INFERENCE OF SOLAR SUBSURFACE FLOWS BY TIME-DISTANCE HELIOSEISMOLOGY

A DISSERTATION
SUBMITTED TO THE DEPARTMENT OF PHYSICS
AND THE COMMITTEE ON GRADUATE STUDIES
OF STANFORD UNIVERSITY
IN PARTIAL FULFILLMENT OF THE REQUIREMENTS
FOR THE DEGREE OF
DOCTOR OF PHILOSOPHY

Junwei Zhao
March 2004

I certify that I have read this dissertation and that, in my opinion, it is fully adequate in scope and quality as a dissertation for the degree of Doctor of Philosophy.

Philip H. Scherrer
(Principal Advisor)

I certify that I have read this dissertation and that, in my opinion, it is fully adequate in scope and quality as a dissertation for the degree of Doctor of Philosophy.

Vahé Petrosian

I certify that I have read this dissertation and that, in my opinion, it is fully adequate in scope and quality as a dissertation for the degree of Doctor of Philosophy.

Alexander G. Kosovichev

Approved for the University Committee on Graduate Studies.

Abstract

The inference of plasma flow fields inside the convection zone of the Sun is of great importance. On the small scales, this helps us to understand the structure and dynamics of sunspots and supergranulation, and the connections between subsurface flows of active regions and coronal activity. On the large scales, it helps us to understand solar magnetic cycles and the generation and decay of solar magnetic fields. In this thesis, the flow fields in the upper convection zone are inferred on both large and small scales by employing time-distance helioseismology.

A detailed description of time-distance measurements is presented, together with the derivation of the ray-approximation kernels that are used in data inversion. Two different inversion techniques,the LSQR algorithm and Multi-Channel Deconvolution, are developed and tested to infer the subsurface sound-speed variations and three-dimensional flow fields. The subsurface flow field of a sunspot is investigated in detail, converging flows and downdrafts are found below the sunspot's surface. These flows are believed to play an important role in keeping the sunspot stable. Subsurface vortical flows found under a fast-rotating sunspot may imply that part of the magnetic helicity and energy to power solar flares and CMEs is built up under the solar surface. A statistical study of numerous solar active regions reveals that the sign of subsurface kinetic helicity of active regions has a slight hemispheric preference.

On the large scales, latitudinal zonal flows, meridional flows and vorticity distribution are derived for seven solar rotations selected from years 1996 to 2002 from SOHO/MDI Dynamics data, covering the period from solar minimum to maximum. The zonal flows display mixed faster and slower rotational bands, known as torsional oscillation. The residual meridional flows, after the meridional flow of the minimum

year is subtracted from the flows of each following year, display a converging flow pattern toward the active zones in both hemispheres. The global vorticity distribution is largely linear with latitude, mainly resulting from the solar differential rotation. In addition, a linear relation between the rotation rate of the magnetized plasma and its magnetic field strength is found: the stronger the magnetic field, the faster the plasma rotates.

Acknowledgment

I feel grateful for the generosity, kindness and patience of many people towards me during these years of my study at Stanford University. First of all, I thank my adviser Phil Scherrer, who continues to offer me various advice, understanding and support. I thank Sasha Kosovichev and Tom Duvall, whose help made the studies inside this dissertation possible, whose knowledge, suggestions and insights were incorporated into this dissertation. I also thank Aaron Birch, Rick Bogart, Doug Braun, Sebastien Couvidat, Laurent Gizon, Rasmus Larsen, Charlie Lindsey, Yang Liu, Jesper Schou and those I may forget to mention, whose frequent or occasional discussions with me helped me progress in my study, more or less. I thank Keh-Cheng Chu and Brian Roberts, who are always ready and skillful to help me solve all kinds of computer problems. Additionally, I thank Jeneen Sommers, whose kind help facilitated my life at Wilcox Solar Observatory.

On the other hand, I thank my family, without whose support I could hardly have made through my study. I thank my parents, who always support and understand me, and forgive me being so far away from their sides for so many years. At last but not least, I thank my wife Ting, whose love and patience that I can never ask for more, for supporting me through all these years. The life at Stanford, including both happiness and sadness, both comfort and hardship, both laughter and depression, will be cherished as beautiful lifelong memories for both of us.

Contents

List of Tables

List of Figures

Chapter 1

Introduction

1.1 Motivation

The Sun is a fascinating star, which not only supports life on the Earth, but also exhibits some extraordinary scientific phenomena, such as solar flares, coronal mass ejections (CMEs), sun-quakes (Kosovichev & Zharkova, 1998), etc. It is solar magnetism that makes the Sun so fascinating, and it is solar eruptions caused by solar magnetism that makes the study of the Sun more and more important with the advent of the space age. The Sun exhibits an 11-year cycle of magnetic activities, and we just witnessed the passage of a solar activity peak in 2000 and 2001. Through magnetic reconnection which usually takes place in the corona above sunspots, solar flares are triggered, protons and electrons are immediately accelerated to high energies and escape into space. In addition, CMEs, which are often associated with flares, eject a great amount of plasma into space, sometimes towards the Earth. Powerful solar storms may knock out electricity supplies, interrupt electronic communications, and display wonderful auroral shows in high latitude areas on the Earth. These make the study of the Sun interesting and important.

Sunspots are dark areas on the solar surface where strong magnetic fields concentrate. They are a couple of thousand degrees cooler than quiet solar regions, and it is believed that this is caused by the convective collapse in the presence of strong magnetic fields of an order of 10^3 Gauss. Sunspots are relatively stable solar features, and

they often remain on the solar surface without apparent shape changes for a few days or longer. The mass flows around sunspots have been under study ever since Evershed (1909) by analyzing various spectra (e.g., Schlichenmaier and Schmidt, 1999), and by tracking motions of small features such as umbral dots (e.g., Wang & Zirin, 1992). The dynamics of sunspots' umbra and penumbra on the surface has been quite clear, however, the interior structure and dynamics of sunspots remain largely unknown. Clearly, it is of great importance to study the subsurface dynamics of sunspots, because most of the magnetic flux that forms sunspots remains beneath the surface, and the growth and decay of sunspots depend heavily on the subsurface dynamics.

On the other hand, solar eruptions often occur in the solar chromosphere and corona above sunspots. Both the storage of magnetic energy that powers solar flares and the plasma motions that trigger solar flares may occur in the interior beneath the corresponding active regions. The study of sunspots' subsurface dynamics will certainly help us understand the connections between subsurface flows and solar eruptions above the solar surface.

The quiet solar regions are dominated by supergranules with a typical size scale of 30 Mm and a typical time scale of 20 hours. Supergranulation is characterized by its divergent flows with an order of 500 m/s. Small magnetic features often concentrate at the boundaries of supergranules, where supergranular divergent flows terminate and downward flows are observed(e.g., Wang, 1989). Supergranulation is generally believed to be a kind of solar convection cells on a scale larger than granulation and mesogranulation (existence of mesogranulation is often questioned), while many researchers dispute such an interpretation. Despite the convincing reports of downward flows along magnetic features at the boundaries of supergranules, no upward flows were observed convincingly inside supergranules, and the magnitude of vertical velocity inside supergranules is believed to be lower than 50 m/s. The magnetic field at the boundaries of supergranulation forms magnetic networks. Some researchers proposed that such magnetic field might be generated by the "local dynamo", a source different from that of active regions (Cattaneo, 1999).

The Sun exhibits an 11-year cycle of magnetic activity. During solar minimum years, sunspots are barely observed on the solar surface for a few months, although the

magnetic network is still present. Occasionally, bipolar active regions emerge at high latitudes of approximately 35° in both hemispheres. With the evolution of the solar cycle from the minimum towards maximum, more and more bipolar active regions emerge on the solar surface with the preferred emergence latitudes migrating towards the solar equator by and by. During solar maximum years, dozens of sunspots may be observed on the solar disk in one single day. The magnetic polarities of bipolar active regions are not arbitrary: usually, in one hemisphere, the leading sunspots carry one polarity and the following sunspots carry the opposite polarity; on the other hand, the leading sunspots in one hemisphere carry a magnetic polarity opposite to that of the leading sunspots in the other hemisphere. This is known as "Hale's Law". Additionally, in both hemispheres, leading sunspots in bipolar active regions usually are located closer to the solar equator than the corresponding following sunspots. This is known as "Joy's Law". However, although these two laws are generally true, cases violating both laws are not rare. After the solar maximum passes, another solar cycle begins, and in this following solar cycle, the magnetic polarities in both hemispheres reverse compared to the preceding one.

Where does solar magnetism come from, and why does the Sun exhibit such a magnetic cycle? The generation of solar magnetism and the evolution of the solar cycle are believed to be caused by the solar dynamo, which operates at the "tachocline", located at the base of solar convection zone. It is believed that toroidal magnetic field is generated at the base of the convection zone. When the magnetic field rises up through the convection zone due to magnetic buoyancy, the magnetic field is amplified and poloidal magnetic field is then produced by the so-called α-effect. Finally, magnetic field emerges from the solar photosphere as bipolar active regions. Numerical simulations of the solar dynamo have shown that the generation and amplification of solar magnetism depend largely on the solar differential rotation and meridional flows (e.g., Dikpati & Charbonneau, 1999). Therefore, the solar interior rotational and meridional flows deduced from helioseismology play an important role in better simulation and understanding of the solar dynamo.

The Sun displays differential rotation, faster near the equator and slower near both poles. In the interior, the rotational rate displays a large radial gradient close

to the base of the convection zone (e.g., Howe et al., 2000a), which is believed to be the location of the solar dynamo operation. For meridional flows, poleward flows with an order of 20 m/s were observed at the surface since the 1970s (e.g., Duvall, 1979). Inside the Sun, the poleward meridional flows were found extending nearly to the base of the convection zone (Giles, 1999). Although equatorward meridional flows are expected in order to keep the mass conservation, no evidence of such flows has been found directly from observations.

To summarize all the above, the subsurface flow fields of sunspots and supergranules are crucial to understand the origin and dynamics of these local solar features. The interior large-scale flows, including rotational and meridional flows, are the basis for understanding solar dynamo, the theory to explain the generation of solar magnetism and magnetic periodicity. However, the inference of these solar interior properties relies upon helioseismology, on both global and local scales.

On the other hand, the Sun is the only star we can observe and study in great details. As a typical main-sequence star in the H-R diagram, all the properties that we learn from the Sun, such as element abundances, temperature and pressure distributions, thickness of convection zone and radiation zone, the rotational and meridional flow profiles, the generation and evolution of magnetism, etc., are crucial for understanding other main-sequence stars and checking the stellar models.

Helioseismology is a unique tool to solve the challenges posed by the Sun. The last couple of decades witnessed a rapid progress in the field of helioseismology. By studying solar oscillation signals, helioseismologists have derived the interior structures of the Sun, including sound-speed variations and internal rotation speed as functions of both latitude and radius, as well as their variations with the solar cycle. On the other hand, local helioseismology emerged in the last decade as a new powerful tool to study interior structures and mass flows of local regions, such as supergranules and active regions. In the following, I will begin with an introduction of a brief history of both global and local helioseismology, and present some major results from this field.

1.2 Global Helioseismology

The five-minute solar oscillations were first observed by Leighton, Noyes, & Simon (1962), and later were interpreted as standing acoustic waves in the solar interior (Ulrich, 1970; Leibacher & Stein, 1971). This interpretation was later confirmed by further observations by Deubner (1975), Claverie et al. (1979) and Duvall & Harvey (1983). These observations established the solar oscillations range from low spherical harmonic degree to intermediate and high degrees, and opened a way for detailed inferences of solar interior properties, such as internal rotation rate (Duvall et al., 1984) and sound-speed variations (Christensen-Dalsgaard et al., 1985).

Better frequency resolution requires a longer uninterrupted observation. Observation networks were thus constructed to meet such a requirement. Among them are the Taiwan Oscillation Network (TON; Chou et al., 1995), and the Global Oscillation Network Group (GONG; Harvey et al., 1996), which can also provide data for local helioseismology studies in addition to serving global helioseismology studies. Observations from space can provide uninterrupted observations from one single instrument with no seeing problems, and the instrument Michelson Doppler Imager (MDI) aboard spacecraft *Solar Heliospheric Observatory* (*SOHO*) (Scherrer et al., 1995) meets this purpose. *SOHO* was launched to Lagrange point $L1$ between the Earth and the Sun in December, 1995. Continuous data (except occasional interruptions) have been transmitted down to the Earth since then, and this greatly enriched helioseismological studies.

Observations by global networks and spacecraft have provided a great amount of valuable data, and thus have boosted scientific research significantly. The properties of solar structure, such as interior sound-speed and density distribution, were inferred. Based on solar models, e.g., the solar model S (Christensen-Dalsgaard et al., 1996), inferences of the sound-speed perturbation from observation were made to compare with the model. Basu et al. (1997) derived $\delta c^2/c^2$ from observation, and found that the derived values agreed with the model within 0.5% from around 0.1 $R_\odot$ to near the surface. Similar results were also obtained by, for example, Gough et al. (1996) and Kosovichev et al. (1997). This is exciting because it proved the success of both

modeling efforts and helioseismic inferences.

In addition to the sound-speed distribution, the internal rotation rate can also be inferred from the observations of frequency splitting based on the equation:

$$\omega_{nlm} - \omega_{nl0} = \int_0^R \int_0^\pi K_{nlm}(r,\theta)\Omega(r,\theta) r \mathrm{d}r \mathrm{d}\theta, \tag{1.1}$$

where ω_{nlm} is angular oscillation frequency at the mode of radial order n, angular degree l and azimuthal order m, K_{nlm} is the sensitivity kernel that can be derived from eigenfunctions of the modes, and $\Omega(r,\theta)$ is the internal rotation rate to be inferred as a function of both solar radius and latitude. Equation (1.1) is a two-dimensional linear equation, and several inversion techniques have been developed to solve it, including the methods of optimally localized averages (OLA), regularized least squares (RLS), spectral expansion, etc. (see, e.g., Christensen-Dalsgaard, Schou, & Thompson, 1990). Inversion results showed that the internal rotation rate was basically consistent with the surface rate through the convection zone, and a sharp gradient of rotation rate existed at the bottom of the convection zone of around 0.7 $R_\odot$, denoted as tachocline, which is believed as the location of solar dynamo (Spiegel & Zahn, 1992; Thompson et al., 1996; Kosovichev et al., 1997; Schou et al., 1998).

It has been a few years since the start of MDI and GONG observations, and this makes possible the study of variations of solar interior properties with the evolution of solar cycle. Mixed faster and slower zonal flow bands at the solar surface, known as torsional oscillation, have been known for a couple of decades from analyses of solar Doppler data (Howard & LaBonte, 1980). Analysis of f-mode frequency splitting (Kosovichev & Schou, 1997; Schou, 1999) detected the existence of torsional oscillation extending to a depth of approximately 10 Mm. More recently, it was found that this phenomenon extended to the depth of 0.92 $R_\odot$ (Howe et al., 2000a), and later again, found that it might extend down to the tachocline through the entire convective zone at high latitudes (Vorontsov et al., 2002). The faster bands migrate towards the solar equator as the solar cycle evolves to the activity maximum, with the activity zones residing in the poleward side of the faster bands. Figure 1.1 shows the result obtained by Howe et al. (2000a).

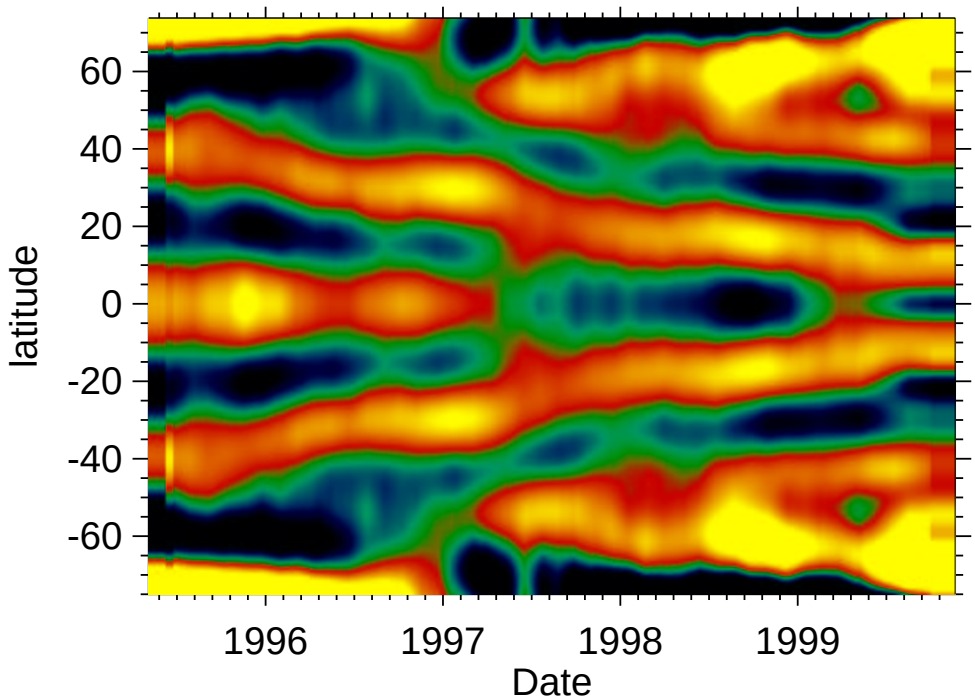

Figure 1.1: The migration of the faster zonal bands towards the solar equator with the evolution of solar cycle. The fastest(*red and yellow*) and slowest (*blue and dark*) rotation rate in the plot are 1.5 and -1.5 nHz. The results were obtained at a depth of $0.99R_{\odot}$. The plot is adopted from Howe et al. (2000a).

Another solar cycle dependent variation found by helioseismology is an oscillation of the internal rotation rate, with a period of 1.3 years near the base of the convection zone (Howe et al., 2000b), which may have some interesting implications in understanding the solar dynamo.

1.3 Local Helioseismology

Global helioseismology has successfully presented us with results on internal sound-speed structures and rotation rates of the Sun, but it still leaves many questions unresolved. For instance, it cannot detect the rotational asymmetry between solar northern and southern hemispheres; it cannot determine the meridional flows,

which are perhaps as important as the differential rotation in understanding the solar dynamo; it cannot disclose the structure and dynamics of local features, such as supergranules and sunspots. In order to answer these questions, three major local helioseismic techniques have been proposed since the late 1980s and early 1990s, and currently they are still under development. These three techniques are ring-diagram helioseismology, acoustic holography, and time-distance helioseismology.

1.3.1 Ring-Diagram Helioseismology

The idea of ring-diagram helioseismic analysis was first proposed by Gough & Toomre (1983) and Hill (1988). It was suggested that in the Fourier domain (ω, k_x, k_y), mode frequencies would be changed by the local velocity field through advection of the wave pattern. Figure 1.2 shows examples of cross sectional cuts at different frequencies obtained by the dense-pack approach (Haber et al., 2002). The power spectra can then be fitted by the following profile

$$P = \frac{A}{(\omega - \omega_0 + k_x U_x + k_y U_y)^2 + \Gamma^2} + \frac{b_0}{k^3} \tag{1.2}$$

where two Doppler shifts ($k_x U_x$ and $k_y U_y$), background power b_0 and central frequency ω_0, width Γ and amplitude A are parameters to be fitted (Haber et al., 2002). The fitting parameters are then passed on to infer the depth dependent flows by solving a one-dimensional regularized least squares inversion problem.

This technique has been carried out by many researchers to infer the rotational speed and meridional flows in the upper solar convection zone (e.g., Schou & Bogart, 1998; González Hernández et al., 1998; Basu, Antia, & Tripathy, 1999; Haber et al., 2000, 2002). The rotational rates inferred from the ring-diagram analyses were compared with those inferred from global frequency splittings, and reasonable agreement was reached (Haber et al., 2000). Poleward meridional flows were also derived in both hemispheres, and a hemispheric asymmetry was found. More recently, Haber et al. (2002) and Basu & Antia (2003) investigated variations of solar rotational and meridional flows with the solar cycle. Haber et al. (2002) reported an extra flow cell, equatorward flows in the northern hemisphere a few megameters below the solar

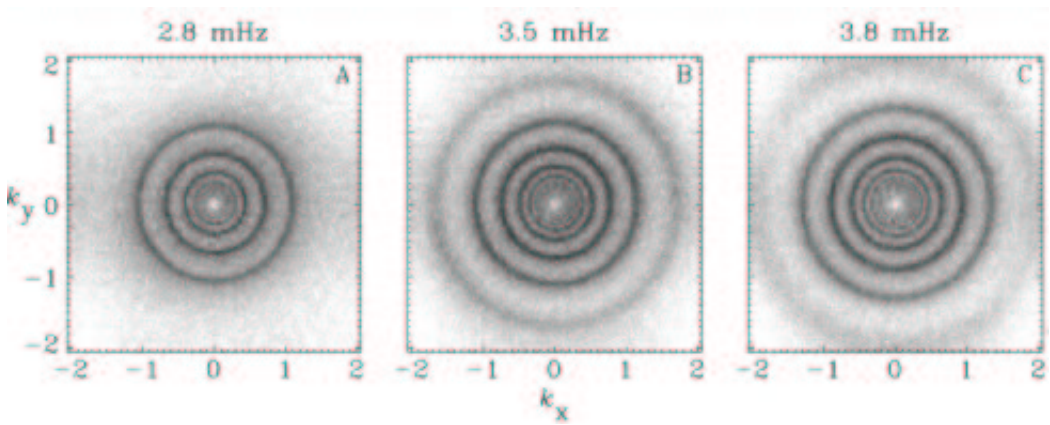

Figure 1.2: Cross sectional cuts of a three-dimensional ring-diagram power spectrum at three different frequencies. The plot is adopted from Haber et al. (2002).

surface, but this was not confirmed by Basu & Antia (2003) and Zhao & Kosovichev (2004). By use of MDI dynamics campaign data, Haber et al. (2002) made synoptic flow maps, coined as "solar subsurface weather", to study local dynamics, in particular, around large active regions.

Ring-diagram analysis was also used to study local variations of acoustic frequencies, but with poor spatial resolution. Hindman et al. (2000) derived the local frequencies from the dense-pack ring-diagram data, and found that large frequency shifts were often associated with active regions. They believed that the physical phenomenon that induces the frequency shifts might be confined within the near-surface layers rather than deep in the Sun. Similar results were also found by Rajaguru, Basu, & Anita (2001).

1.3.2 Acoustic Holography

Analogous to the optical holography, acoustic holography is a tool to image acoustic power of the solar interior, especially beneath solar active regions. This technique was developed by Lindsey & Braun (1997) (for more, see the review by Lindsey & Braun, 2000a) and in parallel, by Chang et al. (1997), who coined this technique as "acoustic imaging" (see the review by Chou, 2000).

Acoustic holography is based on the computation of

$$H_{\pm}(\mathbf{r}, z, \nu) = \int_P \mathrm{d}^2\mathbf{r}' G_{\pm}(\mathbf{r}, \mathbf{r}', z, \nu)\psi(\mathbf{r}', \nu), \tag{1.3}$$

where H_+ and H_- are the monochromatic egression and ingression, and ψ is the local acoustic disturbance at surface location $\mathbf{r}'$ and frequency ν. G_+ and G_- are Green's functions that express how a monochromatic point disturbance at a position $\mathbf{r}'$ on the surface propagates backward and forward in time to the focus at $\mathbf{r}$ and depth z. By computing the egression and ingression powers, "acoustic moats" and "acoustic glories" were found associated with solar active regions (Lindsey & Braun, 2000a).

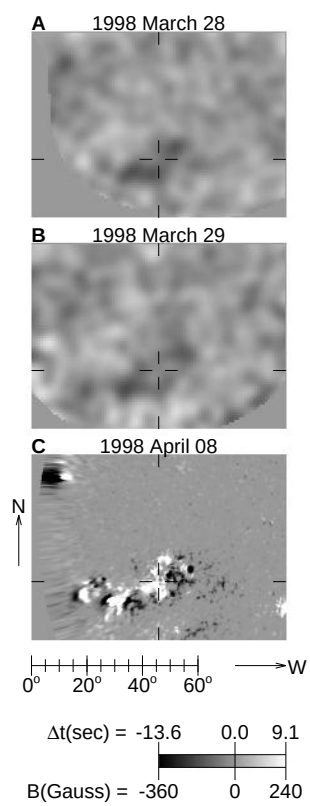

Figure 1.3: The far side acoustic images constructed by use of Dopplergrams of March 28 and 29, 1998, and the magnetogram of April 8, 1998. The acoustic anomalies seen on March 28 and 29 have the same Carrington longitude as the active regions seen in the magnetogram of April 8. This plot is adopted from Lindsey & Braun (2000b).

This technique was eventually used to successfully detect large active regions on the far side of the Sun (Lindsey & Braun, 2000b), as shown in Figure 1.3.

Phase-sensitive acoustic holography was later developed to derive the phase differences by correlating the egression and ingression signals (Braun & Lindsey, 2000).

$$C(\mathbf{r}, z, t) = \int \mathrm{d}t' H_-(z, \mathbf{r}, t') H_+(z, \mathbf{r}, t' + \tau) \tag{1.4}$$

The phase differences may yield information about dynamics, which then can be used to derive subsurface flow fields. The supergranular flow fields and outflows from sunspots were inferred by such an analysis (Braun & Lindsey, 2003). Numerical modeling for better understanding and better interpretation of acoustic holography is still ongoing.

1.3.3 Time-Distance Helioseismology

Time-distance helioseismology was first developed by Duvall et al. (1993, 1996), and then widely used as a tool to study interior properties of the Sun. Giles et al. (1997) confirmed that the solar meridional flows are poleward, and also extended the poleward flow into the deeper convection zone, although the existence of equatorward return flows is still uncertain. Rotational velocity was also derived from time-distance helioseismology (Giles, 1999), and compared to results from global frequency splittings. Reasonable agreement was found.

Time-distance helioseismology was also used to detect local properties. By deriving the travel times of acoustic waves through the underneath of supergranules, Duvall & Gizon (2000) tried to infer $\nabla \times \mathbf{v}_\mathrm{h}$ ($\mathbf{v}_\mathrm{h}$ stands for the two-dimensional horizontal velocity) and $(\nabla \times \mathbf{v}_\mathrm{h})/(\nabla \cdot \mathbf{v}_\mathrm{h})$, which may imply the vorticity and kinetic helicity inside and outside the supergranular regions. More recently, Gizon, Duvall, & Schou (2003) detected the wavelike nature of supergranules that may explain the previously observed faster rotation rate of supergranules.

Inversion of time-distance helioseismology was performed to infer the interior sound-speed variations and flow fields of sunspots (Kosovichev, 1996; Kosovichev,

Duvall, & Scherrer, 2000; Jensen et al., 2001). It was found that the sound speed beneath sunspots is faster compared to the quiet Sun except in the region immediately below the sunspot's surface. Downdrafts and inward flow patterns were found below sunspots, which may provide an explanation for why sunspots can remain stable for a few days.

Forward modeling of time-distance helioseismology was carried out as well. Continuous efforts to model time-distance data by the Born-approximation were made (Birch & Kosovichev, 2000; Birch et al., 2001; Birch, 2002), and a general framework of computing forward problems and an example of distributed-source sensitivity kernels were described by Gizon & Birch (2002).

Since this dissertation mainly focuses on the studies of time-distance helioseismology, more detailed descriptions of measurements, sensitivity kernels, and inversions are presented in the following chapters.

1.4 Results Contained in this Dissertation

Chapter 2 introduces the observational techniques and inversion methods that are used in this dissertation. Some key details of time-distance measurements are given, following which one should be able to repeat such measurements. The derivation of the ray-approximation based sensitivity kernels is also presented in this chapter, and all inversion results throughout this dissertation are based on such kernels. Based on the work of Kosovichev (1996) and Jacobsen et al. (1999), I have developed two different inversion codes: one using LSQR algorithm and one based on Multi-Channel Deconvolution (MCD). The details of these two inversion techniques and the comparison of inversion results are also presented in this chapter.

A well-observed sunspot with high resolution was studied to infer its subsurface flow fields in Chapter 3. A converging and downward directed flow was found from just beneath the solar surface to a depth of approximately 5 Mm, and below this, an outward and upward flow was derived. This result may support the cluster sunspot model proposed by Parker (1979), and also agrees with result of numerical simulations for magnetoconvection (Hurlburt & Rucklidge, 2000).

The same analysis technique was then used to study a fast-rotating sunspot in order to understand the surface dynamics of this special phenomenon. A vortex, in which plasma rotated in the same direction as observed in white light images at the surface, was found near the surface, but an opposite vortex was found in deeper layers at a depth of about 12 Mm. A structural twist of the sunspot was also found by inferring subsurface sound-speed variation structures. These results are presented in Chapter 4.

It has been an interesting topic to study the magnetic helicity (or current helicity) of solar active regions, which may provide a useful tool to understand the solar subsurface dynamics, and to investigate the relationship between solar eruptions and the helicity in the corresponding active region. Our time-distance helioseismology inversions provide us three-dimensional velocities below the solar surface and thus enable us to compute the subsurface kinetic helicity of active regions. We have studied 88 active regions, and found that the kinetic helicity tends to carry a negative sign in the southern hemisphere, and a positive sign in the northern hemisphere. This statistical study is presented in Chapter 5.

Some attempts were made to derive the flow structures of supergranules. But due to the strong cross-talk effects between the divergent (convergent) flows and downward (upward) flows at the center (boundary) of supergranules, it is difficult to derive reliable vertical velocities by inverting time-distance measurements. Nevertheless, horizontal return flows were found for some large supergranules at the depth of approximately as 12 Mm, which might suggest that supergranules have a convective structure. The depth of supergranules was derived based on the correlation of horizontal flow divergences at the surface with different depths, and it was approximated 14 Mm. These results are presented in Chapter 6.

MDI had a $\sim$2 months dynamics campaign each year following its launch in December of 1995. These observations provide valuable data to study the "solar subsurface weather", and also to study the variation of various solar properties with the solar cycle, since these data cover the years from 1996 to 2002, from the solar minimum to past the solar maximum. One Carrington rotation was selected from each year for study, and synoptic flow maps were then constructed from the surface to a

depth of 12 Mm for all these selected Carrington rotations. Interior rotational speed, meridional flow speed and vorticity distribution were deduced from such synoptic flow maps. Migrating zonal flows, migrating converging residual meridional flows, and some properties of vorticity distributions were found from these computations. Large-scale flows were then obtained by averaging these high resolution results, which could be used to compare with results obtained by ring-diagram analyses. This work is presented in Chapter 7.

Once we have synoptic flow maps, we can overlap the magnetic synoptic map with the synoptic flow map to study the relationship between the magnetic field strength and rotational speed of magnetic features on the solar surface. After masking the major active regions, we found that the residual rotational speed of weak magnetic features (mainly pores and network structures) is nearly linearly proportional to its magnetic field strength. This linear relationship varies with the phase of solar cycle, and the linear ratio is largest during solar maximum years. In addition, it was found that the plasma of the following polarity has a faster speed than the plasma of leading polarity but with the same magnetic field strength. These results are included in Chapter 8.

A summary is given in the last chapter, Chapter 9, with some perspective on the future studies in time-distance helioseismology.

Chapter 2

Time-Distance Measurement and Inversion Methods

2.1 Time-Distance Measurement Procedure

Time-distance helioseismology was first introduced by Duvall et al. (1993, 1996), and then greatly improved and widely used in the later studies (see section §1.3.3 for introductions on the major results obtained in the past years. In this chapter, I present the detailed procedure of doing time-distance measurement and inversion problems. The following description is more like a technical note, without including many derivations and theories that can be found in Giles (1999). One should be able to reproduce time-distance measurement by following the descriptions in this chapter, together with some parts of codes and parameters presented in Appendix A.

2.1.1 MDI Data

The Michelson Doppler Imager (MDI) is an instrument dedicated to helioseismology studies aboard the spacecraft *Solar and Heliospheric Observatory (SOHO)*, which was launched in December, 1995. *SOHO* was placed in orbit of Lagrange point L_1 between the Earth and Sun, thus, MDI provided helioseismologists an unprecedented

data quality, free of day and night shifts and free of seeing. Since 1996, MDI has provided continuous (with occasional interruption) coverage of medium-l Dopplergrams, full-disk campaign data for a couple of months each year and many high-resolution Dopplergrams, along with magnetic field observations, which are essentially useful to monitor solar activity and are broadly used by the solar community around the world.

The high-resolution MDI Dopplergrams have a spatial resolution of $1\farcs25$, or $0\farcs625$ per pixel, which is corresponding to 0.034 heliographic degree per pixel at the center of the solar disk. High resolution data only cover a fraction of solar disk. The full-disk Dopplergrams cover the whole solar disk with 1024×1024 pixels, with a spatial resolution of $2\farcs0$/pixel, or 0.12 heliographic degrees per pixel. In every year following the launch of *SOHO*, MDI had a campaign period lasting a couple of months or longer, transmitting down continuous full-disk Dopplergrams that are extremely valuable for helioseismic studies. But, due to the limitation of telemetry, this cannot be done all year long. Therefore, MDI has a Structure observation mode, in which the full-disk data are reduced to 192×192 pixels by the onboard computer and then transmitted down every minute. Details on data parameters, data acquisition and transmission are described by Scherrer et al. (1995).

The observation cadence for all the different observational modes is one minute. The one minute cadence gives a Nyquist frequency of 8.33 mHz when doing Fourier transforms, which is fairly good for helioseismology research.

2.1.2 Remapping and Tracking

The Sun is a sphere, and all points on the Sun's surface can be located by their spherical coordinates. It is more convenient to transform the solar region of interests to a Cartesian coordinate system for local helioseismology studies. There are various remapping algorithms for different purposes, and the one used throughout this dissertation is Postel's projection, which is designed to preserve the great circle distance of any points inside the region to the center of the remapped region. It has been shown

that if the remapped region is not very large, Postel's projection is good at minimizing the deformation of the power-spectrum and is optimal for local helioseismological studies (Bogart et al., 1995).

Usually, a few to tens of hours of continuous Dopplergrams with one-minute cadence are used for helioseismic studies. In order to keep tracking oscillations of specific locations, the differential rotation rate of the Sun should be removed from the observations. One of the two commonly used tracking rates is the latitude dependent Snodgrass rate (Snodgrass, 1984):

$$\Omega/2\pi\,(\mathrm{nHz}) = 451 - 55\sin^2\lambda - 80\sin^4\lambda \tag{2.1}$$

where λ is latitude; the other tracking rate is a solid Carrington rotation rate: 456 nHz, which is corresponding to the rotation rate of magnetic features at the latitude of 17°. However, if using the tracking command `fastrack`, it should be noted that for a specific tracked region, even if one chooses Snodgrass rate to be removed, the actual rotation rate removed is uniformly the Snodgrass rate at the center of the tracked region rather than a latitude dependent rate. This factor should be taken into consideration when tracking before time-distance analysis, and a tracking over very long time should be avoided to prevent the distortion of high latitude regions after tracking. A datacube is thus ready for use with the first dimension as longitude, second dimension as latitude and the third one as time sequence.

The magnitude of Doppler velocities introduced by solar rotation and by supergranular flows is often much larger than the stochastic oscillations on the solar surface. So, usually, the background image which is obtained by averaging all images of the studied time period is subtracted from every Dopplergram.

2.1.3 Filtering

As in all problems of signal processing, filtering is an essential part of the time-distance measurement.

Surface gravity waves, also known as the fundamental mode (f-mode, the lowest ridge in the k-ω diagram shown in Figure 2.1a), have different origins and different

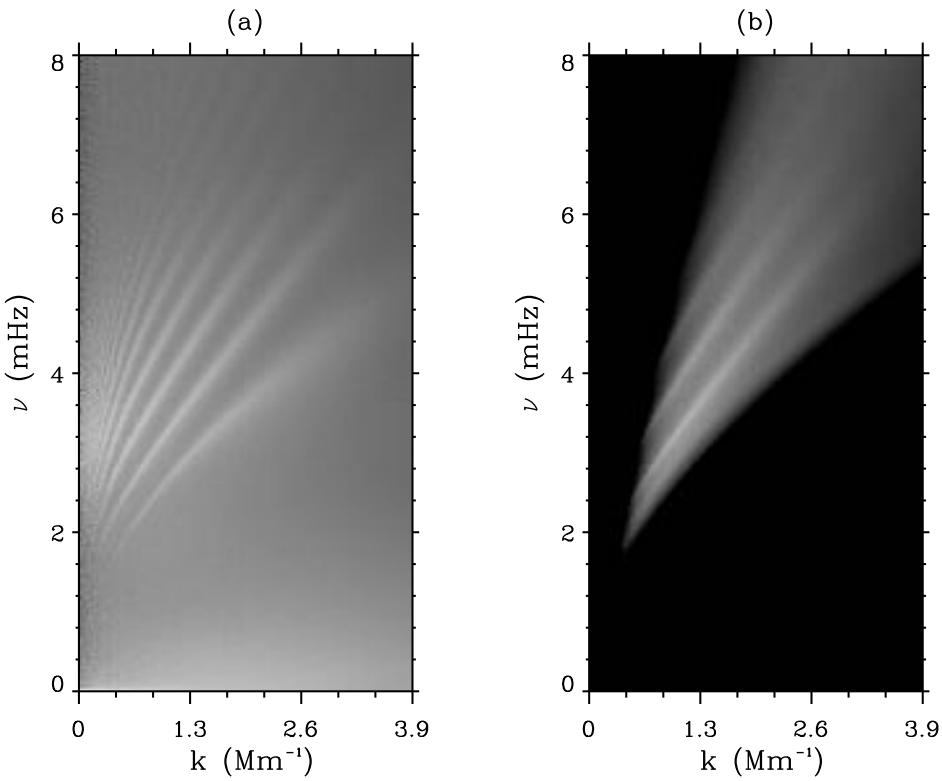

Figure 2.1: (a) The power-spectrum diagram obtained from 512-minute MDI high resolution Dopplergrams; (b) An example of the power-spectrum diagram after f-mode and phase-velocity filtering. This example is corresponding to a case of annulus range: $1\overset{\circ}{.}190 - 1\overset{\circ}{.}598$, with the phase-velocity filter centered at a speed of ~ 25 km/s. Both diagrams are displayed after taking a logarithm of the acoustic power.

properties with the pressure modes (p-modes) that are studied throughout this dissertation. Therefore, the f-mode should be filtered out from the k-ω diagram firstly. The locations of the f-mode and p_1 ridges in the k-ω diagram can be approximated with polynomial forms of (Giles, 1999):

$$\begin{aligned} l_0 &\approx R_\odot k_0 = 100\nu^2 \\ l_1 &\approx R_\odot k_1 = \sum_{k=0}^{4} c_k \nu^k \qquad c = \{17.4, -841, 95.6, -0.711, -0.41\} \end{aligned} \tag{2.2}$$

where the cyclic frequency $\nu \equiv \omega/2\pi$ is measured in milliHertz. A filter is then

constructed by use of Gaussian roll-off with full transmission halfway between the f- and p_1- ridges, and no transmission at and below the f-ridge. The f-mode signals are thus filtered out by applying this filter to the k-ω power spectrum.

The phase-velocity filter has turned out to be a very useful tool to strongly improve the signal-noise ratio when the annulus radius is rather small, and this makes mapping the travel times with certain spatial resolution possible. All the waves with the same ratio of ω/k_h travel with the same speed and travel the same distance between bounces off the solar surface, where k_h is the horizontal wavenumber. Therefore, in the Fourier domain, we can design a phase-velocity filter that has a desired phase speed ω/k_h, which is equal to the travel distance divided by the corresponding travel time that can be computed from the ray-approximation based on the solar model, and filter out all other waves which do not have the same phase speed. Such a filter is designed to have a Gaussian shape, with full pass on the line with desired slope, and the full width at half maximum chosen like given in Appendix A. An example of a two-dimensional k-ω diagram obtained from 512-min high resolution MDI data after f-mode filtering and phase-velocity filtering is shown in Figure 2.1. All the necessary parameters for phase-velocity filtering for different annulus ranges used in my study are presented in Appendix A. In practice, the k-ω power spectrum has three dimensions, and one can easily imagine the shape of the three-dimensional phase-velocity filter.

2.1.4 Computing Acoustic Travel Time

The computation of temporal cross-correlation functions between the signals located at two different points on the solar surface is the essential part of time-distance measurement to infer the travel time of acoustic waves from one point to the other through the curved ray paths beneath the solar surface. After the filtering is carried out in the Fourier domain, the datasets are transformed back to the space-time domain by the inverse Fourier transform. Suppose f is a set of time-sequence signals on the solar surface, T is the observation duration, then the temporal cross-correlation

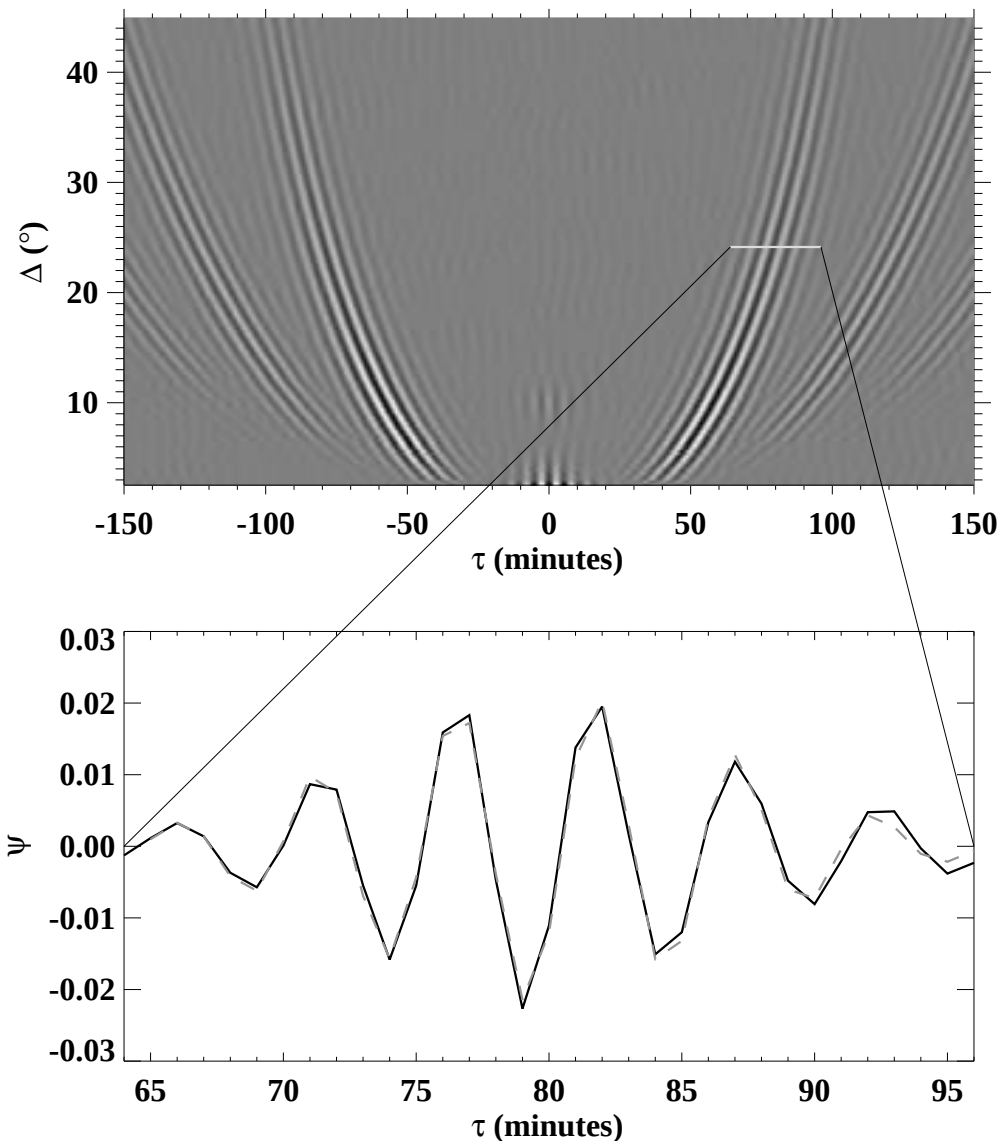

Figure 2.2: Cross-correlation functions for the time-distance measurements. In the upper plot, the gray scale denotes the cross-correlation amplitude as a function of time lag τ and distance Δ. The lower plot shows one cross-correlation function (*solid line*) for $\Delta = 24\overset{\circ}{.}1$, and its fitting function (*dashed line*). This plot is adopted from Giles (1999).

function between two different locations $\mathbf{r_1}$ and $\mathbf{r_2}$

$$\Psi(\mathbf{r}_1, \mathbf{r}_2, \tau) = \frac{1}{T} \int_0^T \mathrm{d}t\, f(\mathbf{r}_1, t)\, f(\mathbf{r}_2, t + \tau) \tag{2.3}$$

can be computed. But in practice, the cross-correlation function between two points is often too noisy to be useful; it is practical to compute the cross-correlation function between the signals of a central point and the average signals of all points inside an annulus with a specific distance range to the central point.

Figure 2.2 shows a time-distance diagram and an example of the cross-correlation function for a specific distance. For the case of center-annulus cross-correlation, the part with positive time lag τ is interpreted as the travel time of outgoing waves from the center to its surrounding annulus, and the part with negative lag is interpreted as the travel time of ingoing waves from the surrounding annulus to the central point.

Kosovichev & Duvall (1996) have shown that the cross-correlation function for the time-distance measurement is approximately a Gabor function having a form of:

$$\Psi(\Delta, \tau) = A \cos[\omega_0(\tau - \tau_p)] \exp\left[-\frac{\delta\omega^2}{4}(\tau - \tau_g)^2 \right] \tag{2.4}$$

where Δ is the distance between the two points, i.e., $\Delta = |\mathbf{r_1} - \mathbf{r_2}|$, A is the cross-correlation amplitude, ω_0 is the central frequency of the wave packet, τ_p and τ_g are the phase and group travel times, and $\delta\omega$ is the frequency bandwidth. Among these parameters, $A, \omega_0, \tau_p, \tau_g$ and $\delta\omega$ are free parameters to be determined by fitting the cross-correlation function computed from real data by applying a non-linear least squares fitting method. The subroutine used for the non-linear least squares fitting is based on the code `mrqmin` in §15.5 of *Numerical Recipes in FORTRAN 77: the Art of Scientific Computing* (Second Edition); or alternatively, the procedure `lmfit.pro` provided by IDL can be used directly. An IDL code to perform the fitting by use of `lmfit.pro` is given in Appendix A. In practice, it turns out that the phase travel time τ_p is often more accurately determined than the group travel time τ_g in the fitting procedure, and will be used to represent wave travel time throughout this dissertation unless specified otherwise.

2.1.5 Constructing Maps of Travel Times

For one specific location, after outgoing and ingoing travel times are computed, one can derive the mean travel time variations and travel time differences for this location:

$$\delta\tau^{\rm oi}_{\rm mean}(\mathbf{r},\Delta) = \frac{\tau^+ + \tau^-}{2} - \langle\tau\rangle, \qquad \delta\tau^{\rm oi}_{\rm diff}(\mathbf{r},\Delta) = \tau^+ - \tau^- \tag{2.5}$$

where τ^+ and τ^- indicate the outgoing and ingoing travel times, respectively, and $\langle\tau\rangle$ represents the theoretical travel time for this specific annulus range. $\delta\tau^{\rm oi}_{\rm mean}$ and $\delta\tau^{\rm oi}_{\rm diff}$ are the measurements which are going to be used directly to do inversions to infer the sound-speed variations and flow fields of the solar interior. If we move the central point to another location, and repeat the above procedure, the $\delta\tau^{\rm oi}_{\rm mean}$ and $\delta\tau^{\rm oi}_{\rm diff}$ can be measured for this point. Thus, we can select every pixel inside the region of interest to calculate the corresponding travel times, and obtain a map of the travel times, as shown in Figure 2.3(a) and (b).

Above, the center-annulus cross-correlation is computed to derive mean travel times and travel time differences. In order to have more measurements as inputs to do inversions, we divide the circular annulus into four quadrants, corresponding to East, West, North and South directions. The cross-correlation functions between average signals inside these quadrants and the signal of the central point are computed, respectively, and then the East-center and center-West functions are combined to derive the West-East travel time differences $\delta\tau^{\rm we}_{\rm diff}$. Similarly, the North-South travel time differences $\delta\tau^{\rm ns}_{\rm diff}$ are derived. It is often thought that $\delta\tau^{\rm we}_{\rm diff}$ is more sensitive to the West-East velocity and $\delta\tau^{\rm ns}_{\rm diff}$ more sensitive to the North-South velocity. The maps for $\delta\tau^{\rm we}_{\rm diff}$ and $\delta\tau^{\rm ns}_{\rm diff}$ can also be made in the same way as $\delta\tau^{\rm oi}_{\rm diff}$, examples are shown in Figure 2.3(c) and (d). Usually, the maps for mean travel times $\delta\tau^{\rm oi}_{\rm mean}$ are used to do inversions for interior sound-speed variation; the maps for $\delta\tau^{\rm oi}_{\rm diff}, \delta\tau^{\rm we}_{\rm diff}$ and $\delta\tau^{\rm ns}_{\rm diff}$ are combined as inputs to do inversions for subsurface flow fields.

We then change the annulus radius to repeat all the above procedures to make another set of measurements. Since the ray path of small annuli reaches shallow solar interiors and the ray path of long annuli reach the deep interiors, the appropriate

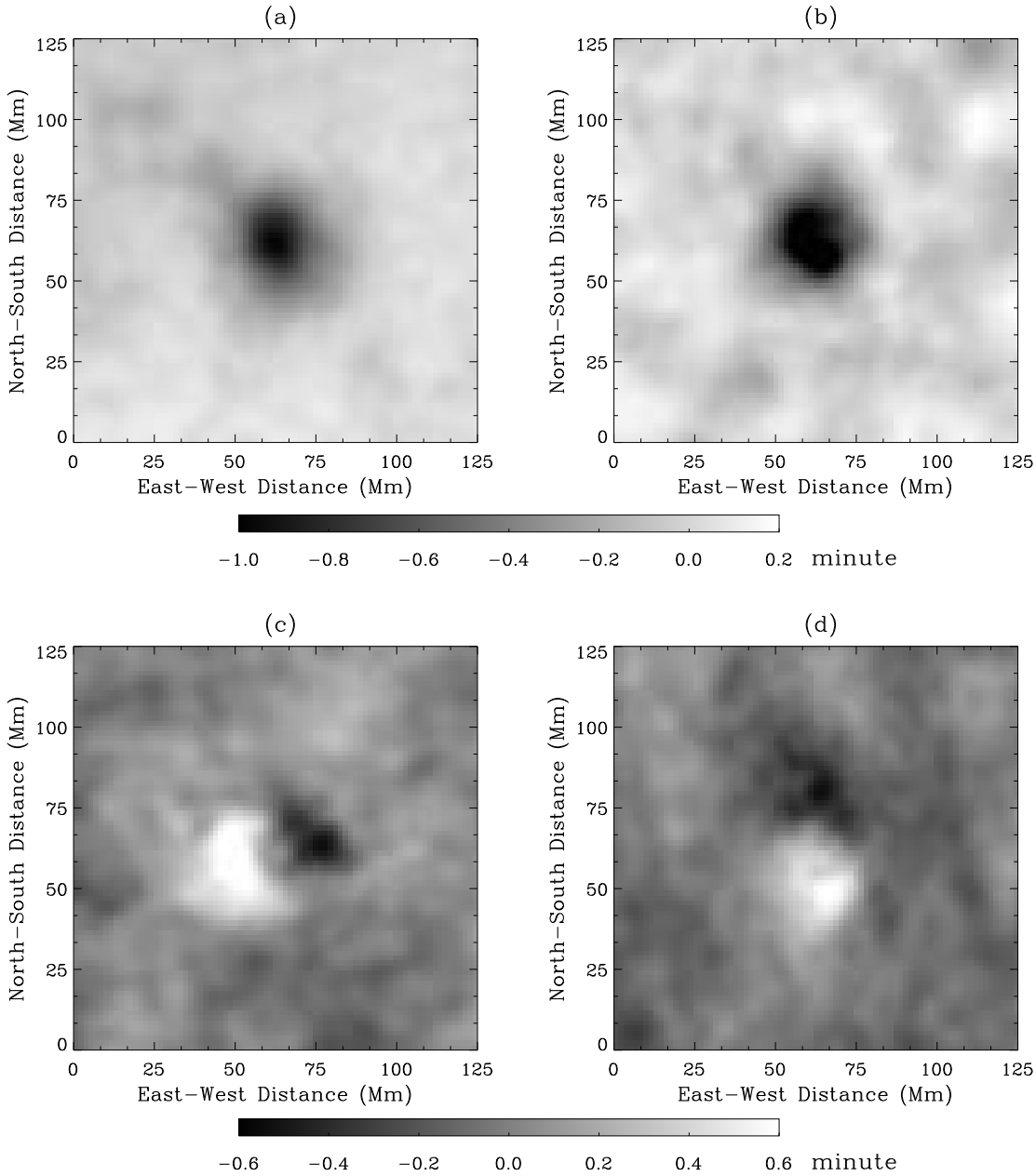

Figure 2.3: The maps of travel times for a solar region including a sunspot: (a) Mean travel times $\delta\tau^{\rm oi}_{\rm mean}$; (b) Outgoing and ingoing travel time differences $\delta\tau^{\rm oi}_{\rm diff}$; (c) East- and West-going travel time differences $\delta\tau^{\rm we}_{\rm diff}$; (d) North- and South-going travel time differences $\delta\tau^{\rm ns}_{\rm diff}$. The annulus ranges used to obtain these maps are $1\overset{\circ}{.}19 - 1\overset{\circ}{.}598$.

combinations of annulus choices can cover the depths from the solar surface to approximately 20 – 30 Mm in depth. Inversions are then applied on such measurements to derive the sound-speed structure and flow fields at different depths.

2.2 Ray-Approximation Inversion Kernels

In order to do time-distance inversions, we need to have inversion kernels that could be derived from a solar model. In this section, I describe how to derive the inversion kernels based on the ray-approximation, and the compare ray-approximation kernels and wave-approximation kernels.

2.2.1 Ray Paths

The acoustic waves traveling downward from the solar surface are continuously refracted due to the increasing acoustic propagation speed with the depth. Eventually, the waves will turn around and return toward the surface, where they get reflected back from the layer with acoustic cutoff frequency $\omega_{\rm ac}$. The acoustic modes with wavelengths small compared to the solar radius $R_\odot$ are amenable to ray treatment (Gough, 1984). Throughout this dissertation, the ray-approximation is employed to make inversion kernels though the derivation of wave-approximation kernels is currently under development (Birch et al., 2001; Gizon & Birch, 2002). The following content and equations on the ray-approximation largely follow the contents in D'Silva & Duvall (1995).

In polar coordinates, the ray equation for the acoustic mode (ν, l) is

$$\frac{\mathrm{d}r}{r\mathrm{d}\theta} = \frac{v_{\rm gr}}{v_{\rm gh}}\,, \tag{2.6}$$

where $v_{\rm gr}$ and $v_{\rm gh}$ are the radial and horizontal components of the group velocity, and

they are expressed as

$$
\begin{aligned}
v_{\mathrm{gr}} &= \frac{\partial \omega}{\partial k_r} = \frac{k_r \omega^3 c^2}{\omega^4 - k_h^2 c^2 \omega_{\mathrm{BV}}^2}, \\
v_{\mathrm{gh}} &= \frac{\partial \omega}{\partial k_h} = k_h \omega c^2 \Big(\frac{\omega^2 - \omega_{\mathrm{BV}}^2}{\omega^4 - k_h^2 c^2 \omega_{\mathrm{BV}}^2} \Big),
\end{aligned}
\tag{2.7}
$$

where the radial and horizontal wavenumbers k_r and k_h are given by the local dispersion relations

$$
\begin{aligned}
k_r^2 &= \frac{1}{c^2}(\omega^2 - \omega_{\mathrm{ac}}^2) - k_h^2 \Big(1 - \frac{\omega_{\mathrm{BV}}^2}{\omega^2} \Big), \\
k_h^2 &= \frac{L^2}{r^2} = \frac{l(l+1)}{r^2}.
\end{aligned}
\tag{2.8}
$$

In the above equations, ω_{BV} is the Brunt-Väisälä frequency, given by

$$
\omega_{\mathrm{BV}}^2 = g \Big(\frac{1}{\Gamma_1} \frac{\mathrm{d} \ln p}{\mathrm{d} r} - \frac{\mathrm{d} \ln \rho}{\mathrm{d} r} \Big),
\tag{2.9}
$$

where $\Gamma_1 = (\partial \ln p / \partial \ln \rho)_s$ is the adiabatic index and g is the gravity at radius r. The acoustic cutoff frequency ω_{ac} is given by

$$
\omega_{\mathrm{ac}}^2 = \frac{c^2}{4 H_\rho^2} \Big(1 - 2 \frac{\mathrm{d} H_\rho}{\mathrm{d} r} \Big),
\tag{2.10}
$$

where H_ρ is the density scale height

$$
H_\rho = - \Big(\frac{\mathrm{d} \ln \rho}{\mathrm{d} r} \Big)^{-1}.
\tag{2.11}
$$

Once we have all the above equations for the ray approximation, by use of the solar model S (Christensen-Dalsgaard et al., 1996) in practice, we can compute the ray paths for certain acoustic waves with certain acoustic frequency ω and spherical harmonic degree l. The one-skip distance is obtained by integrating the ray equation (2.6) for an initial position (r_1, θ_1). The integration is carried on till the mode turns around at the turning point (r_2, θ_2), where the Lamb frequency $\sqrt{l(l+1)}c/r$ approaches ω and k_r goes to zero. The one-skip distance, or the travel distance of

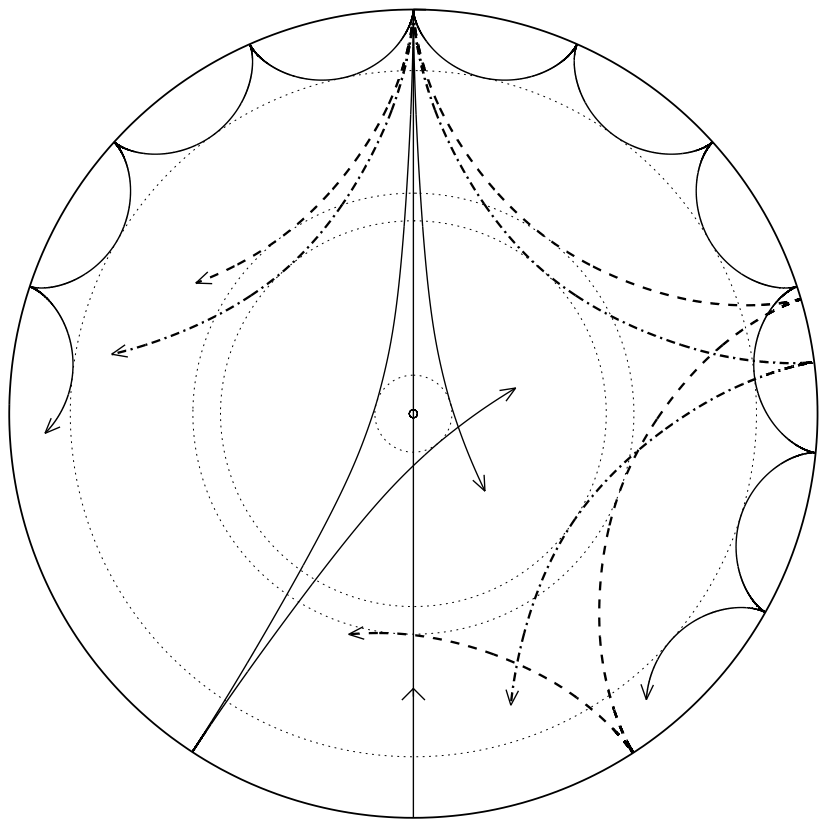

Figure 2.4: A diagram of several ray-paths, showing the different modes of rays reach different depths of solar interior. This plot is adopted from Christensen-Dalsgaard (2002).

the ray, is defined as the angular distance between photospheric reflection points:

$$\Delta = 2|(\theta_2 - \theta_1)|. \tag{2.12}$$

After the ray-path is determined, and the phase velocity at specific locations is known, the corresponding phase travel time can be computed from

$$\tau_p = \int_\Gamma \frac{k\mathrm{d}s}{\omega} = \int_\Gamma \frac{\mathrm{d}s}{v_p} \tag{2.13}$$

where Γ is the ray path. Although this is a simple equation, it is the basis for solving time-distance inversion problems.

2.2.2 Travel Time Perturbation

The following content largely follows the descriptions in Kosovichev et al. (1997). In the ray-approximation, the travel times are only sensitive to the perturbations along the ray paths. The variations of travel times obey Fermat's Principle (e.g., Gough, 1993)

$$\delta\tau = \frac{1}{\omega}\int_{\Gamma} \delta\mathbf{k}\,\mathrm{d}s \tag{2.14}$$

where $\delta\mathbf{k}$ is the perturbation of the wave vector due to the structural inhomogeneities and flows along the unperturbed ray path Γ.

In the solar convection zone, the Brunt-Väisälä frequency ω_{BV} is small compared to the acoustic cutoff frequency and the typical solar oscillation frequencies, and will be neglected in the following derivations. Thus, after considering the effects caused by the presence of magnetic field, the dispersion relation can be simplified as

$$(\omega - \mathbf{k}\cdot\mathbf{v})^2 = \omega_{\mathrm{ac}}^2 + \mathbf{k}^2 c_f^2, \tag{2.15}$$

where $\mathbf{v}$ is the three-dimensional velocity and c_f is the fast magnetoacoustic speed

$$c_f^2 = \frac{1}{2}\left(c^2 + c_A^2 + \sqrt{(c^2+c_A^2)^2 - 4c^2(\mathbf{k}\cdot\mathbf{c}_A)^2/k^2}\right) \tag{2.16}$$

where $\mathbf{c}_A = \mathbf{B}/\sqrt{4\pi\rho}$ is the Alfvén velocity, $\mathbf{B}$ is the magnetic field strength and ρ is the plasma density. To first-order in $\mathbf{v}$, δc, $\delta\omega_{\mathrm{ac}}$, and $\mathbf{c}_A$, equation (2.14) becomes

$$\delta\tau^{\pm} = -\int_{\Gamma}\left[\frac{\pm\mathbf{n}\cdot\mathbf{v}}{c^2} + \frac{\delta c}{c}\frac{k}{\omega} + \frac{\delta\omega_{\mathrm{ac}}}{\omega_{\mathrm{ac}}}\frac{\omega_{\mathrm{ac}}^2}{c^2\omega^2}\frac{\omega}{k} + \frac{1}{2}\left(\frac{c_A^2}{c^2} - \frac{(\mathbf{k}\cdot\mathbf{c}_A)^2}{k^2c^2}\right) + \epsilon\right]\mathrm{d}s \tag{2.17}$$

where $\mathbf{n}$ is a unit vector tangent to the ray, and $\delta\tau^{\pm}$ denotes the perturbed travel times along the ray path ($+\mathbf{n}$) and opposite to the ray path ($-\mathbf{n}$). In equation (2.17), ϵ represents some other contributions that are difficult to quantify, such as phase differences caused by wave reflection and observing errors in Dopplergrams. The effects of flows and structural perturbations can be separated by taking the difference

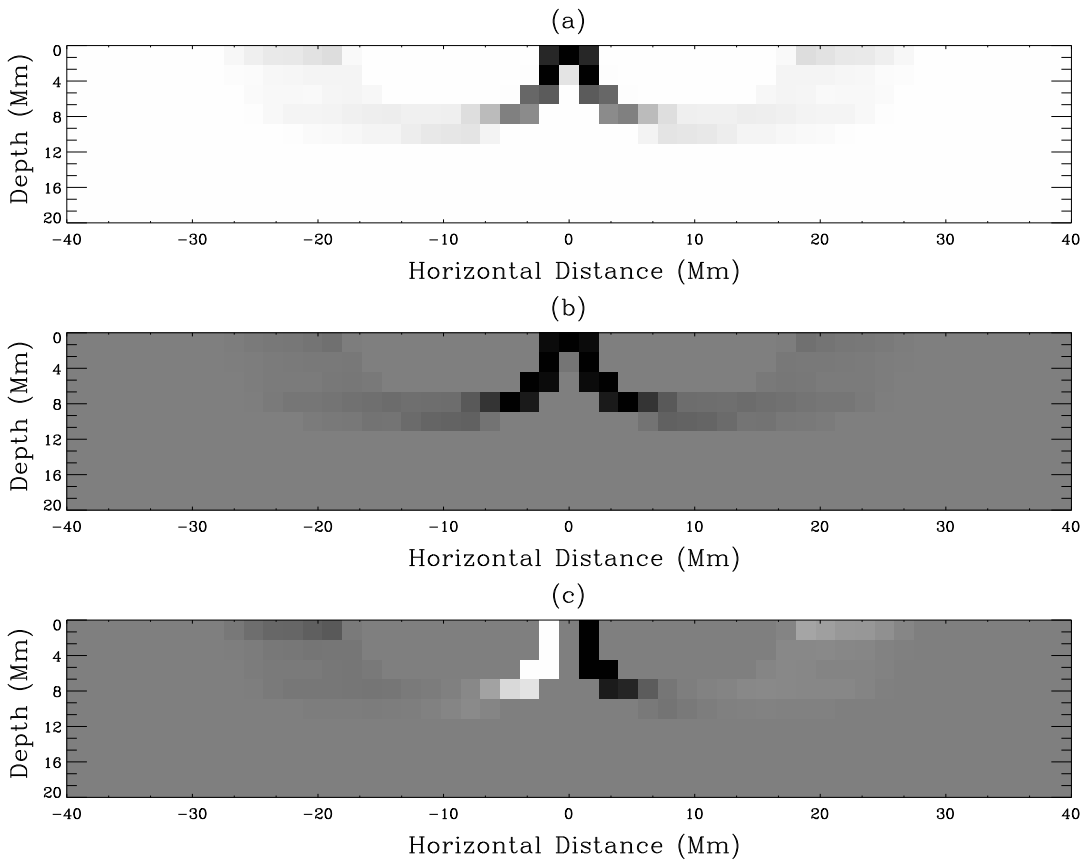

Figure 2.5: Vertical cuts of ray-approximation inversion kernels. (a) Sound-speed kernel for measurement $\delta\tau^{\rm oi}_{\rm mean}$; (b) Vertical velocity kernel for measurement $\delta\tau^{\rm oi}_{\rm diff}$; (c) Horizontal velocity kernel for measurement $\delta\tau^{\rm oi}_{\rm diff}$. These kernels are corresponding to the annulus ranges 1°.598 to 2°.414.

and the mean of the reciprocal travel times:

$$\delta\tau_{\rm diff} = -2\int_\Gamma \frac{\mathbf{n}\cdot\mathbf{v}}{c^2}{\rm d}s, \tag{2.18}$$

$$\delta\tau_{\rm mean} = -\int_\Gamma \left[\frac{\delta c}{c}\frac{k}{\omega} + \frac{\delta\omega_{\rm ac}}{\omega_{\rm ac}}\frac{\omega_{\rm ac}^2}{c^2\omega^2}\frac{\omega}{k} + \frac{1}{2}\left(\frac{c_A^2}{c^2} - \frac{(\mathbf{k}\cdot\mathbf{c}_A)^2}{k^2c^2}\right) + \epsilon\right]{\rm d}s. \tag{2.19}$$

Equation (2.18), though simple, provides the link between the measured travel time differences and the solar interior velocity, and thus gives us a useful tool to

determine the solar subsurface flow fields. Ideally, equation (2.19) can be used to derive the sound-speed perturbation structures, and the anisotropy of the term with $\mathbf{c}_A$ may be used to derive the Alfvén velocity, hence the magnetic field strength. Despite the efforts by Ryutova & Scherrer (1998), no significant progress has been made to disentangle the effects caused by the presence of the magnetic field from the sound-speed perturbation. One useful idea, which I tried, is to make more measurements of travel times in different directions, that is, in addition to the measurements of $\tau_{\rm oi}, \tau_{\rm we}$ and $\tau_{\rm ns}$, we can make the travel time measurements of quadrants northeast-southwest and northwest-southeast. Therefore, more information on anisotropy is obtained, and those measurements help change the inversion problem from being under-determined to be well determined. However, we now have effects from sound-speed variation, flow fields and Alfvén speed perturbation, the combination of which makes the inversion problem very complicated and difficult to solve. Clearly, more efforts could be made in order to make such an inversion possible, and make the derivation of subsurface magnetic field strength possible, which should be very interesting.

2.2.3 Ray-Approximation and Wave-Approximation Kernels

Based on the equations presented in the above two sub-sections and by use of the solar model S (Christensen-Dalsgaard et al., 1996), we compute the ray-approximation inversion kernels for both sound-speed perturbations and three-dimensional flow velocities.

The computation of the ray-approximation kernels closely resemble the procedure of time-distance measurements. Say, for the case of center-annulus measurement, we compute the ray paths and phase travel times from the central point to all the points inside the surrounding annulus, then the paths and travel times are averaged onto grids with the same spatial resolution as the measurements. Corresponding to the measurements of $\delta\tau^{\rm oi}_{\rm diff}$ and $\delta\tau^{\rm oi}_{\rm mean}$, the sensitivity kernels for the sound-speed perturbation, horizontal velocities (v_x and v_y) and vertical velocity (v_z) are computed respectively, as shown in Figure 2.5. The inversion kernels for the v_x, v_y and v_z are also obtained in the same way for measurements of $\delta\tau^{\rm we}_{\rm diff}$ and $\delta\tau^{\rm ns}_{\rm diff}$, the plots of which

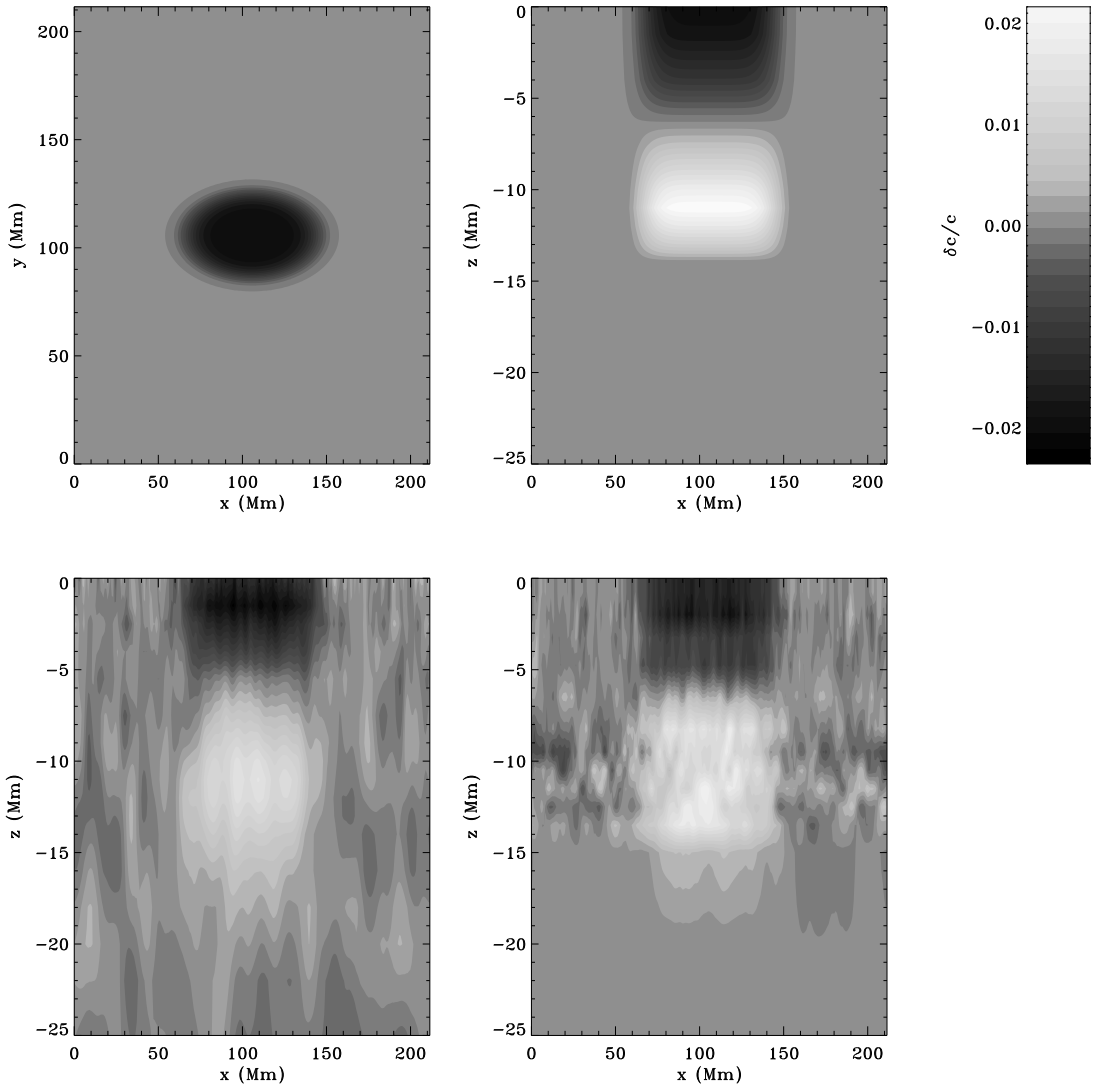

Figure 2.6: An artificial sunspot model and the inversion results. The gray scale represents the sound-speed variations. *Upper*: the surface layer (*left*) and a vertical cut (*right*) of an artificial sunspot model that is to mimic the results presented by (Kosovichev, Duvall, & Scherrer, 2000). The forward problem is performed based on this model to derive the mean travel times, which are then used to do inversions. *Lower*: the inversion result from Fresnel-zone approximation (*left*) and ray-approximation (*right*) kernels. This plot is adopted from Couvidat et al. (2004).

are not shown. Therefore, for each measurement of $\delta\tau_{\rm diff}^{\rm oi}, \delta\tau_{\rm diff}^{\rm we}$, and $\delta\tau_{\rm diff}^{\rm ns}$ with each different annulus range, we have a set of inversion kernels corresponding to v_x, v_y and v_z.

It is natural that the ray-approximation may not be the best approximation of the acoustic waves inside the Sun, and the Fresnel-zone approximation (Jensen, Jacobsen, & Christensen-Dalsgaard, 2000) and Born-approximation (Birch & Kosovichev, 2000) are currently under development. Birch et al. (2001) pointed out that for perturbations with radii larger than the first Fresnel-zone, the Born and ray approximations are nearly equivalent; for smaller scale perturbations, the ray approximation may overestimate the travel times significantly. But considering the fact that large amounts of data are involved in measurement and inversion, together with the choice of different regularization types and regularization parameters, it is not immediately clear how the inversion results differ based on different inversion kernels.

Recently, Couvidat et al. (2004) made some intensive comparisons between inversion results based on sensitivity kernels obtained in the ray-approximation and the Fresnel-zone approximation. Different kinds of artificial sound-speed variation structures to simulate sunspot models were made, and the forward problem was performed to derive mean travel times. Then inversions were carried out by utilizing both ray-approximation and Fresnel-zone approximation inversion kernels. The comparison of inversion results shows that, for the sound-speed perturbation, both kernels reveal similar interior structures with similar accuracy in the solar layers shallower than a depth of approximately 15 Mm. Below 15 Mm, however, the ray-approximation can hardly reveal the deeper structures where the Fresnel-zone approximation still works. Figure 2.6 shows one example. It was concluded that the use of Fresnel-zone kernels should not invalidate the results obtained from ray-approximation, provided that the inverted structures lie entirely within the scope of ray-path kernels used. Although the wave approximation inversion kernels for velocities have not been available for comparison, it may be true that similar conclusion can be drawn as for the sound-speed perturbations.

2.3 Inversion Techniques

2.3.1 LSQR Algorithm

Equations (2.18) and (2.19) have shown us the connection between the measured travel times and solar interior properties: sound-speed variations and flow fields. We rewrite these two equations here, dropping the insignificant (presumably) terms in the mean travel times equation:

$$\delta\tau_{\rm diff} = -2\int_\Gamma \frac{\mathbf{v}(\mathbf{r})\cdot\mathbf{n}}{c_0^2(\mathbf{r})}{\rm d}s \tag{2.20}$$

$$\delta\tau_{\rm mean} = -\int_\Gamma \frac{\delta c(\mathbf{r})}{c_0^2(\mathbf{r})}{\rm d}s \tag{2.21}$$

We can divide the three-dimensional region into rectangular blocks, and study the properties inside the blocks as a discrete model. Assume that the sound-speed perturbation, $\delta c/c$, and the ratio of flow velocity to the sound-speed, $\mathbf{v}/c$, are constant in each block and remain unchanged during the observation period, then we can linearize the above equations to obtain:

$$\delta\tau_{\rm mean}^{\lambda\mu\nu} = \sum_{ijk} A_{ijk}^{\lambda\mu\nu}\frac{\delta c_{ijk}}{c_{ijk}}, \tag{2.22}$$

$$\delta\tau_{\rm diff}^{\lambda\mu\nu} = \sum_{ijk,\alpha} B_{ijk,\alpha}^{\lambda\mu\nu}\frac{v_{ijk,\alpha}}{c_{ijk}}, \tag{2.23}$$

where $A_{ijk}^{\lambda\mu\nu}$ and $B_{ijk,\alpha}^{\lambda\mu\nu}$ are the inversion kernels obtained by the ray-approximation based on the descriptions in the last section. Here, λ and μ label the points inside the observed area, and ν labels different annulus ranges, and in most cases of this dissertation is $1 \leq \nu \leq 11$; i, j and k are the indices of the blocks in three dimensions; and α denotes the three components of the flow velocity.

If transforming matrix $B_{ijk,\alpha}^{\lambda\mu\nu}$ into a square matrix, one side of this matrix is, typically, as large as $128\times128\times11\times11\times3$, so equations (2.22) and (2.23) are typical large sparse linear equations which can be solved in the sense of least squares. LSQR is an algorithm proposed by Paige & Saunders (1982) to solve the linear problems

$Ax = y$ or least squares problems $\min||Ax - y||_2$. This algorithm was later widely used in geophysical inverse problems, and helioseismological inverse problems (e.g., Kosovichev, 1996).

The LSQR algorithm is based on the bidiagonalization procedure of Golub & Kahan (1965), and it is analytically equivalent to the standard method of conjugate gradients. It was demonstrated to be more reliable than other algorithms when the coefficients matrix A is ill-conditioned, which is actually the case of our inverse problems. The great advantage of the LSQR algorithm is that it is an iterative method and avoids the computation of the inverse of a large sparse matrix (which is often unstable and involves a great amount of computation). In practice, it is only required for the users to provide the computation of Ax and $A^T y$ for each step of the iteration. This algorithm also has a build-in zero-th order regularization, or damping coefficient, which is to minimize $||x||_2$ and $||Ax - y||_2$ at the same time. We have not found a way to incorporate the first-order or second-order Tikhonov regularization into this algorithm easily and efficiently, except to do that externally by providing an additional dimension of coefficient matrix A.

Because of the extremely large size of the matrices involved, the computation burden of the inversion is also very heavy. Fortunately, it was found that the direct matrix multiplications of Ax and $A^T y$, the core part of the computation and where the most computation time is spent, can be converted into convolution problems, which expedite the computations by a factor of about 20 times in my computations. Later, BLAS library and FFTW package for fast Fourier transforms were employed in the inversion code, which reduced the computation time from the original a couple of days down to a couple of minutes.

There are a few other issues which should be addressed about LSQR algorithm, such as the ability to detect deeper structures, vortical flows, cross-talk, and the spatial resolution. I plan to incorporate such discussions into following chapters when dealing with the particular inversion problems.

2.3.2 Multi-Channel Deconvolution (MCD)

As pointed out in last section, the very large matrix multiplication Ax can be transformed into a convolution. Therefore, it it possible to solve the least square problem in the Fourier domain, which may expedite the computation speed and also provide us an alternative way to do inversions. A multi-channel deconvolution (MCD) technique was developed and have been used in solving local helioseismic problems (Jacobsen et al., 1999; Jensen, Jacobsen, & Christensen-Dalsgaard, 1998).

In the following, I derive the equations for the case of sound-speed perturbations, the equations for three-dimensional velocities can be derived similarly, but with one more dimension. As shown in the last section, we have obtained the discrete equation (2.22) for the sound-speed perturbation:

$$\delta\tau^{\lambda\mu\nu}_{\text{mean}} = \sum_{ijk} A^{\lambda\mu\nu}_{ijk}\,\delta s_{ijk} \tag{2.24}$$

where I use δs_{ijk} to replace $\delta c_{ijk}/c_{ijk}$. By considering the measurement procedure of time-distance, this equation is actually equivalent to a convolution, which is then simplified as a direct multiplication in the Fourier domain:

$$\delta\tilde{\tau}^{\nu}(\kappa_\lambda,\kappa_\mu) = \sum_k \tilde{A}^{\nu}_k(\kappa_\lambda,\kappa_\mu)\delta\tilde{s}_k(\kappa_\lambda,\kappa_\mu) \tag{2.25}$$

where $\delta\tilde{\tau}$, $\tilde{A}$ and $\delta\tilde{s}$ are the Fourier transforms of $\delta\tau$, A and δs, respectively; $\kappa_\lambda, \kappa_\mu$ are the wavenumbers in the Fourier domain corresponding to λ, μ in the space domain. For each specific $(\kappa_\lambda, \kappa_\mu)$, the equation in the Fourier domain is a direct matrix multiplication:

$$d = Gm \tag{2.26}$$

where

$$G = \left\{\tilde{A}^{\nu}_k(\kappa_\lambda,\kappa_\mu)\right\}, \quad d = \left\{\delta\tilde{\tau}^{\nu}(\kappa_\lambda,\kappa_\mu)\right\}, \quad m = \left\{\delta\tilde{s}_k(\kappa_\lambda,\kappa_\mu)\right\}$$

Thus, we have a large number of small linear equations in the Fourier domain. If all these small linear equations can be solved to obtain m for all $(\kappa_\lambda, \kappa_\mu)$, then the two-dimensional m can be inverse Fourier transformed back to the space domain to

obtain all the values of δs_{ijk} that we are seeking.

Equation (2.26) is a small linear complex equation that can be solved in numerous ways. Here, we adopt the method given by Menke (1984), and solve the equations by:

$$m = \left(G^H G + \varepsilon^2 V\right)^{-1} G^H d \tag{2.27}$$

where G^H is the conjugate transpose of G, ε can be viewed as a damping parameter, and V is a diagonal matrix chosen as

$$V = \begin{pmatrix} 1 & 0 & 0 & \dots & 0 \\ 0 & \frac{c_2}{c_1} & 0 & \dots & 0 \\ 0 & 0 & \frac{c_3}{c_1} & \dots & 0 \\ \vdots & \vdots & \vdots & \ddots & \vdots \\ 0 & 0 & 0 & \dots & \frac{c_N}{c_1} \end{pmatrix}$$

where c_N is the sound-speed at the N-th layer from the solar model used.

Just like the damping coefficient λ used in the LSQR algorithm, the choice of ε in MCD is somewhat arbitrary. Often, many artificial tests are performed to choose a reasonable value of ε in practice. Since each small linear equation is solved in the Fourier domain, the first-order or second-order regularization can only be applied in the vertical direction. But on the other hand, because it is in the Fourier domain, the reasoning and effects of applying first- or second-order regularization is vague.

2.3.3 Comparison of LSQR and MCD

Previously, it was argued that MCD had great advantage in computing time over iterative solvers such as LSQR (Jensen, Jacobsen, & Christensen-Dalsgaard, 1998). However, after I utilized the convolution to compute the matrix multiplication, and incorporated the BLAS library and FFTW package into the LSQR technique, the computing time advantage of MCD was gone. Currently, both codes can finish the computation of a typical inverse problem (say, 128×128 in horizontal and 11 in vertical direction) within a couple of minutes on a Pentium IV machine with a speed of 2.0 GHz and a memory of 1.0 GB. The computation time increases with the same

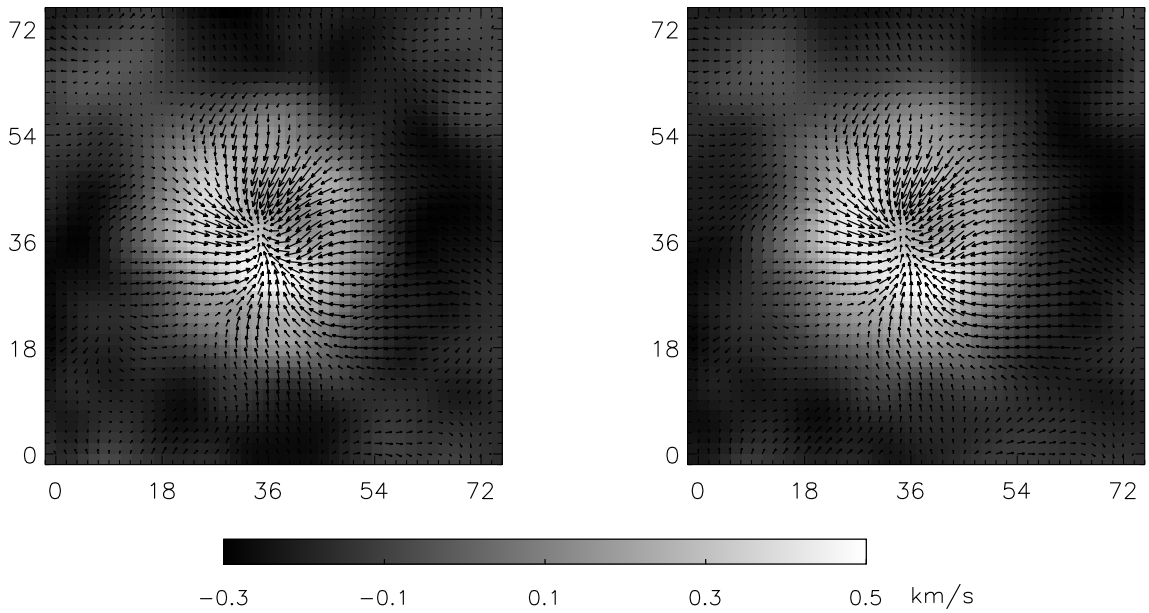

Figure 2.7: Comparison of LSQR algorithm and MCD inversions on the subsurface flow fields of a sunspot. The maps are obtained at the depth of 0 – 3 Mm. In each image, lighter represent downward flows and darker represent upward flows. Arrows in the graph represent horizontal flows, with longest arrow as 1 km/s approximately. Horizontal scales are in units of Mm.

ratio as the increase of the size of the three-dimensions of the inverted region, provided that the memory requirement does not exceed the computer's memory limit.

Then, the next issue is to compare the accuracy of results obtained by these two different inversion techniques. We applied both LSQR and MCD techniques on the same time-distance measurements of a sunspot to derive the subsurface flow fields that will be shown in Chapter 3. Figure 2.7 shows a comparison of the three-dimensional flow fields obtained at the depth of 0 – 3 Mm. Clearly, both horizontal velocities and the vertical velocities agree very well with each other. The correlation coefficients between the three dimensional velocities obtained by these two different techniques are all above 95% at different depths shallower than 12 Mm.

The differences between these two inversion techniques may come from the choice of damping coefficients: λ for LSQR and ε for MCD. LSQR solves the equation iteratively in the space domain, and MCD solves the problem in Fourier domain, whereas

the choice of damping coefficient can hardly agree with each other. Our comparison shown above may and may not reflect the best match of these two regularization parameters.

Chapter 3

Subsurface Flow Fields of Sunspots[1]

3.1 Previous Observations

How plasma flows around a sunspot is an interesting topic that has been studied for decades. Measurements of the subsurface flow can help us to understand how sunspots form, grow, evolve, and decay. The Evershed effect is a well-known phenomenon, which is observed as a prominent outflow from the inner sunspot penumbra to its surrounding photosphere (Evershed, 1909). With the development of new technology to achieve better spatial and temporal resolution, more details of the Evershed effect have been disclosed. Recent results show that Evershed outflows concentrate mainly in narrow and elongated radial penumbral channels (Rimmele, 1995; Stanchfield et al., 1997). This may suggest that the Evershed effect is only a superficial phenomenon at the solar surface. More recent studies of vertical flows have found hot upflows in the inner penumbra, which feed the horizontal Evershed flow, and cool downflows surrounding the outer penumbra where the horizontal Evershed flow terminates (Schlichenmaier and Schmidt, 1999).

The studies mentioned above were conducted by direct spectral observations,

[1]Most part of this chapter was published in the Astrophysical Journal (Zhao, Kosovichev, & Duvall, 2001)

which cannot determine the material flow fields beneath the surface. Time-distance helioseismology provides a very useful technique to probe the interior structure and mass flows beneath the solar surface. Using the time-distance technique based on the travel time measurements of solar surface gravity waves (f mode), Gizon, Duvall, & Larsen (2000) detected a radial outflow, which has an average velocity of about 1 km s^{-1} in the top 2 Mm below the photosphere, extending from sunspot center to up to 30 Mm outside the sunspot umbra. Since the inferred outflow is significantly smaller than the surface outflow speed measured by Doppler velocity, they suggested the Evershed flow is very shallow, which is consistent with conclusions from direct spectral observations. Because of the surface nature of the f mode, these results can only reflect horizontal material motions in shallow layers just beneath the surface (Duvall & Gizon, 2000).

The origin of sunspots is not understood. Parker (1979) suggested a cluster model for sunspots. In order to hold together the loose cluster of magnetic flux tubes, a downdraft beneath the sunspot in the convection zone is needed. But so far, this model lacks direct observational evidence. Though Duvall et al. (1996) have obtained evidence for downflows under the sunspot by use of the time-distance technique, some authors (e.g., Woodard 1997; Lindsey et al. 1996) put this conclusion in suspicion.

In this chapter, we apply the time-distance technique based on measuring travel times of acoustic waves (p modes) to one set of continuous Dopplergram observations by SOHO/MDI. These travel times are inverted to probe the plasma flows under and around the sunspot region. The clear flow picture deep below and around the sunspot presented in this chapter provides strong support to the cluster sunspot model and emergence of magnetic Ω loops.

3.2 Data Acquisition

The set of data analyzed are high resolution Dopplergrams with one-minute cadence, obtained by MDI. The observations began at 15:37UT of June 18, 1998, and lasted for approximately 13 hours. A sunspot was at the center of the field of view and remained stable during the observation period. The resolution of observation is $0\overset{\circ}{.}034$/pixel, and

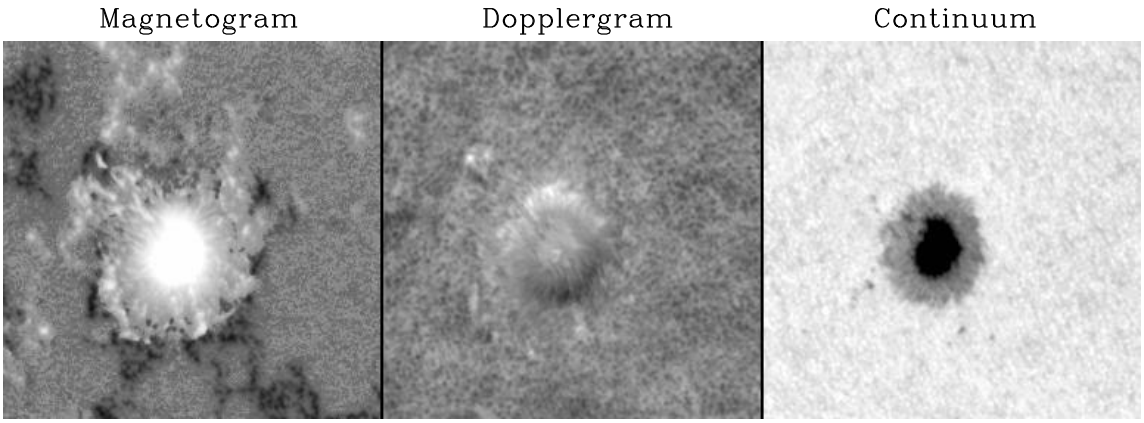

Figure 3.1: A magnetogram, Dopplergram and continuum graph of the studied sunspot in AR8243. The observation was obtained on June 18, 1998.

after a 2×2 rebin, we get an image of 256×256 pixels with resolution of 0.″068/pixel for each one-minute cadence. (Here, 1° represents 1 heliographic degree, which is approximately 12.15 Mm at disk center) A plot of a magnetogram, Dopplergram and intensity graph of the active region are presented in Figure 3.1.

After the dataset was tracked, remapped and filtered, time-distance measurements were then performed as described in §2.1 and Appendix A. To account for variations of the differential rotation with depth, the corresponding mean values of the differences from a quiet Sun region were subtracted from our travel-time differences.

3.3 Tests Using Artificial Data

Kosovichev (1996) applied an inversion technique used in geophysical seismic tomography to develop a new way to detect the mass flows and other inhomogeneities (e.g. sound speed variations) beneath the visible surface of the Sun. Detailed description of the method can be found in that paper. Equations relating flowing speed and travel time differences were solved by a regularized damped least-square technique (Paige & Saunders, 1982).

In order to check the spatial resolution of our calculation code, we designed some artificial data to simulate the flows in the solar interior. The travel time differences

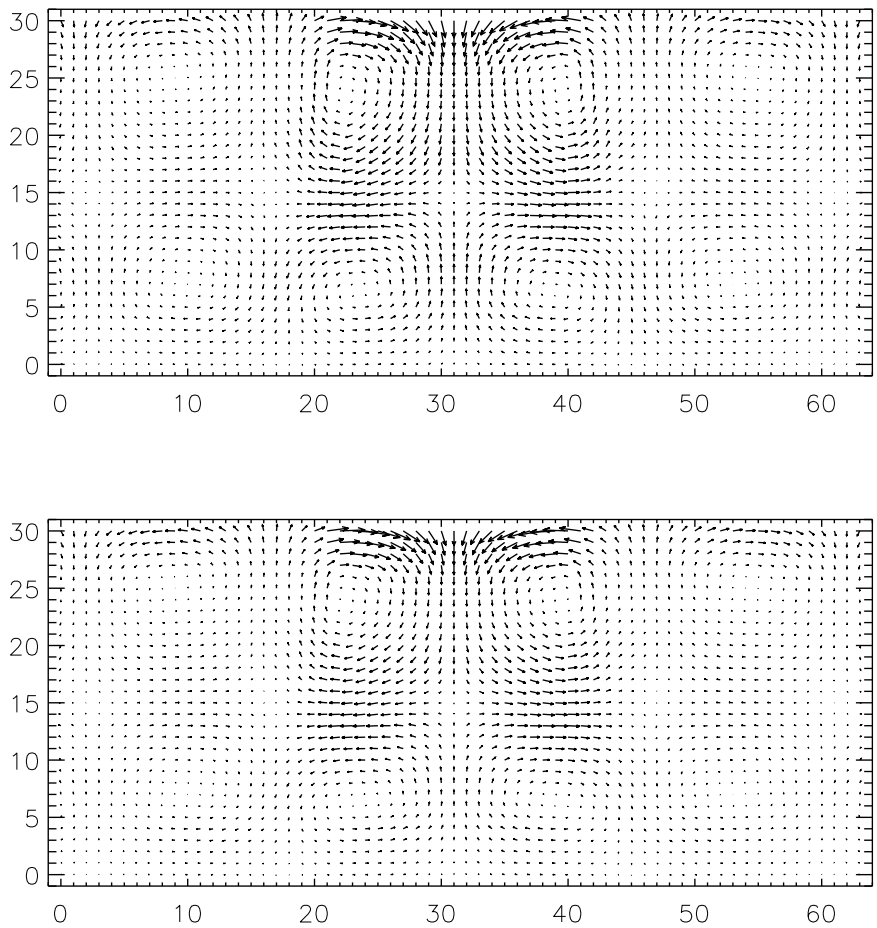

Figure 3.2: The experiment on our inversion code: *upper*, artificial data that simulates the flows of sunspots; *lower*, inversion results.

are calculated using a forward approach, then the inversion was done to get the flow speeds. We found that, generally, the flows in the upper layers can always be recovered well, but flows in the lowest layers may be smaller than the input values (see also Kosovichev and Duvall 1997). We also found that in some specific cases, because of a cross-talk between horizontal flows and vertical components of flow velocities, it may be impossible to recover the original data. This problem will be addressed again in more details in Chapter 6. However, for localized strong flows such as in sunspots, the cross-talk effects do not occur. Figure 3.2 shows a result from a set of our artificial data which has relatively strong motions in the central region. It can be found that

the flow patterns are recovered well, but the velocity magnitude in the lower layers is somewhat smaller than the input. Therefore, the inferred mass flow speeds in the upper layers of the sunspot region should be quite credible. In the lower layers these speeds are probably underestimated.

To double check our inversion results, we compute the travel time differences resulting from the velocities inferred from the inversion, which are compared with the travel time differences computed from time-distance analysis. These travel time differences were used to compute the flow velocities by inversion again to compare with the previous results. Good agreement was achieved from our calculations in both procedures. This means that the observational data are sufficient for recovering both the horizontal and vertical components of the velocities in the sunspot region.

3.4 Inversion Results

3.4.1 Subsurface Sound-speed Structure

Following the inversion technique in §2.3, and the artificial tests in last section, the inversions were performed on the real observational data of the sunspot.

The sound-speed variations below the sunspot's surface was obtained, as shown in Figure 3.3. It was found that about 3 Mm immediately below the sunspot's surface, the sound-speed variation is negative, perhaps due to the low temperature of plasma. Below 3 Mm, the sound-speed variations are largely positive and extend to approximately a depth of 20 Mm. It is yet not clear why the sound-speed is larger in these regions. The larger speed may result from a higher temperature of the plasma, or may result from the magetoacoustic speed that should be but was not disentangled from the sound-speed variations in the inversion procedure, as already discussed in §2.2.

The recent inversion efforts by use of Fresnel-zone approximation (Jensen et al., 2001; Couvidat et al., 2004) confirmed the sound-speed structures inverted here, with the similar structures and similar magnitude of variations. Different inversion codes with different choice of the regularization parameters are suspected to account for the

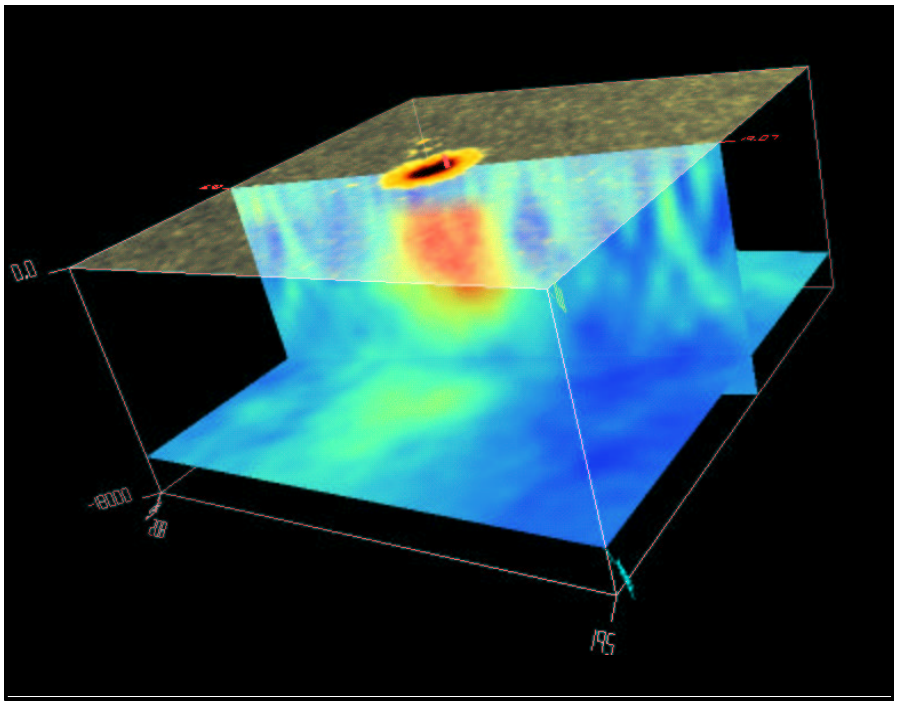

Figure 3.3: Sound-speed variations below the sunspot. The cold color (blue) represents negative sound-speed variations, and the warm color (yellow and red) represents positive variations (courtesy: SOHO/MDI).

slight differences.

3.4.2 Subsurface Flow Fields

We average the calculated travel time differences in 2×2 pixel rebin, thus obtain maps of 128×128 pixels for each $\delta\tau_{\rm oi}, \delta\tau_{\rm we}$ and $\delta\tau_{\rm ns}$ for the eleven different annulus ranges described in Appendix A. We adopt a ten-layer discrete model in depth of the sunspot region, and use the same number of pixels in each layer as in the time-distance measurements. The depth ranges for 10 layers are: 0–3, 3–4.5, 4.5–6, 6–9, 9–12, 12–14, 14–16, 16–18, 18–20.5 and 20.5–23 Mm. The results are presented in Figure 3.4 and Figure 3.5.

Figure 3.4 shows the mass flows in the first and the fourth layers, with arrows

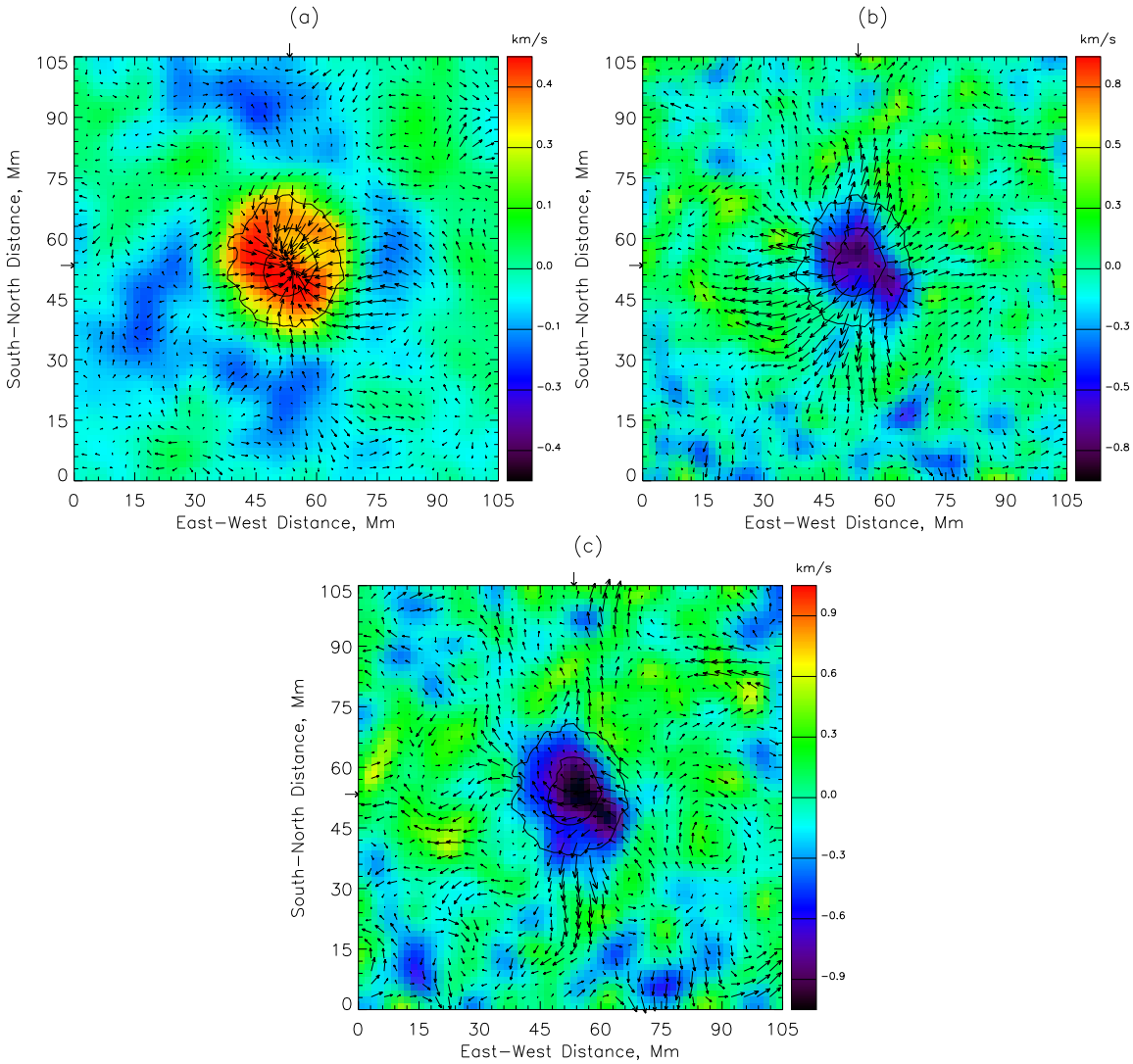

Figure 3.4: Flow fields at a depth of (a) 0 – 3 Mm, (b) 6 – 9 Mm and (c) 9 – 12 Mm. Arrows show magnitude and direction of horizontal flows, and the background shows vertical flows with positive as downward flows. The contours at the center correspond to the umbral and penumbral boundaries. The longest arrow represents 1.0 km/s for (a) and 1.6 km/s for (b) and (c). Arrows outside the frame indicate where the cut is made to obtain graphs of figure 3.5.

showing the direction and strength of the horizontal flows, and the background image showing the vertical velocities. From Figure 3.4a which shows results for the

first layer corresponding to an average of depth of 0–3 Mm, we can clearly identify a ring of strong downflows around the sunspot, with relatively weaker downflows inside the ring. Converging flows at the sunspot center can also be seen in this graph. Figure 3.4b shows the flows in the fourth layer, corresponding to a depth of 6–9 Mm. The sunspot region contains a ring of upflows with relatively smaller downward velocity at the center. Outside this region, the results are a little noisier, but downward velocities seem dominant in the region immediately outside the sunspot. Strong outflows from the sunspot center can be seen, extending more than 30 Mm from the sunspot center. Figure 3.4c shows the flows in the fifth layer, average of depth of 9–12 Mm, where powerful upflows occupy the whole sunspot region. It is of more interests to notice the horizontal mass flows in this layer. Some materials from the West flow right across the sunspot region, and continue moving mainly to the South-East quarter of the graph.

Figure 3.5 shows two vertical cut graphs, one in the East-West direction, the other in the North-South direction, through the center of the sunspot. Although the ten layers were calculated from observation, we only use the upper eight layers to provide more reliability to the results according to our test inversions. The velocities from inversion are actually the average velocities in the block. We assume these as the velocities at the center of the block, and also assume the velocities change uniformly from the block to its neighboring blocks, and calculate the speeds in between two layers by use of linear interpolation. Converging and downward flows can be seen in both graphs right below the sunspot region from 1.5 Mm to about 5 Mm. Below that, the horizontal outflows seem to dominate in this region, though relatively weaker upflows also appear. Below a depth of $\sim$10 Mm, the flows seem not to be concentrated in the region vertically below the sunspot. This can be seen more clearly in the East-West cut. It is intriguing that an upflow towards the East dominates in the region from 10 Mm to 18 Mm. In the South-North cut graph, this pattern is not so clear but still can be seen, with the upflow towards the South stronger than towards the North.

In order to check whether the velocity distribution can keep the structure stable or quasi-steady, $\nabla \cdot (\rho \mathbf{v})/\rho$ was computed, where ρ is the density from a standard

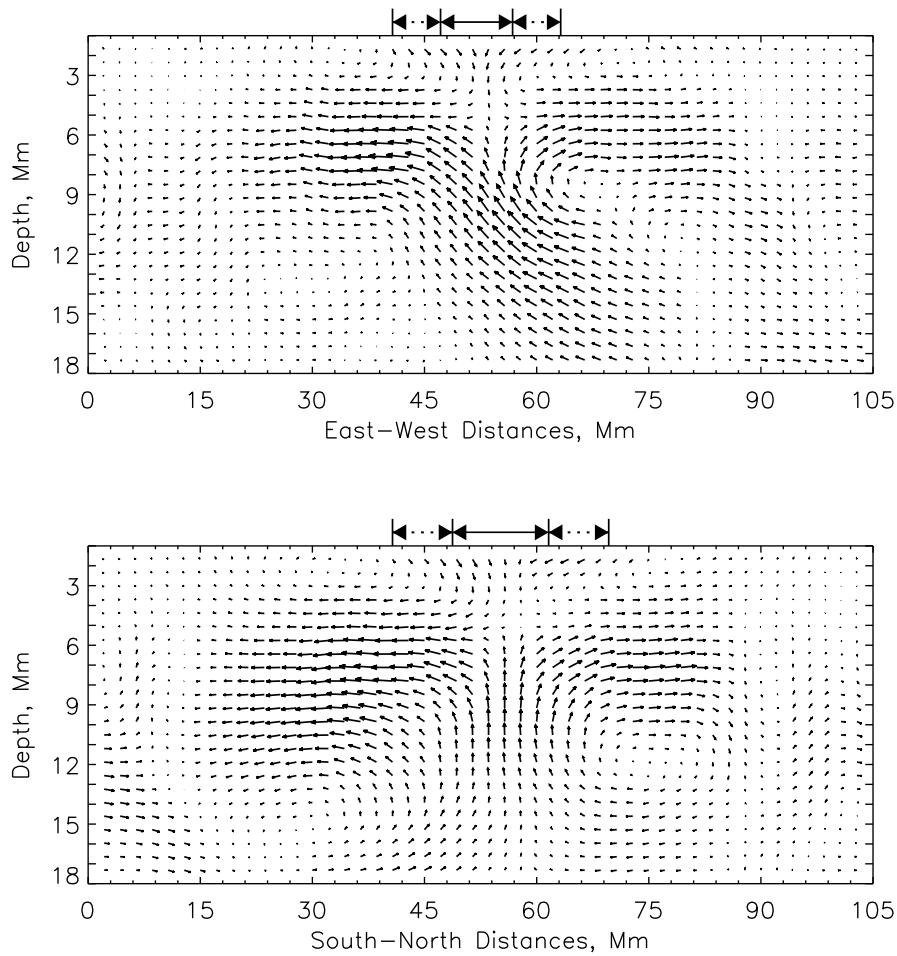

Figure 3.5: Vertical cuts through the sunspot center, with a cut direction of East-West (*upper*, east on left side) and South-North (*lower*, south on left side). The range covered by the line arrow indicates the area of the umbra, and the range covered by the dotted arrow indicates the area of penumbra. The longest arrow indicates a velocity of 1.4 km/s.

solar model. The largest value is of order 10^{-4} s^{-1}, slightly larger than the inverse of the duration of observation. However, the density distribution inside the sunspot and around it, where the magnetic field should be significantly large and the temperature obviously low, is probably significantly different from the standard model, and remains to be determined. Therefore, it is quite possible that the velocity distribution shown in the graph is consistent with the sunspot structure.

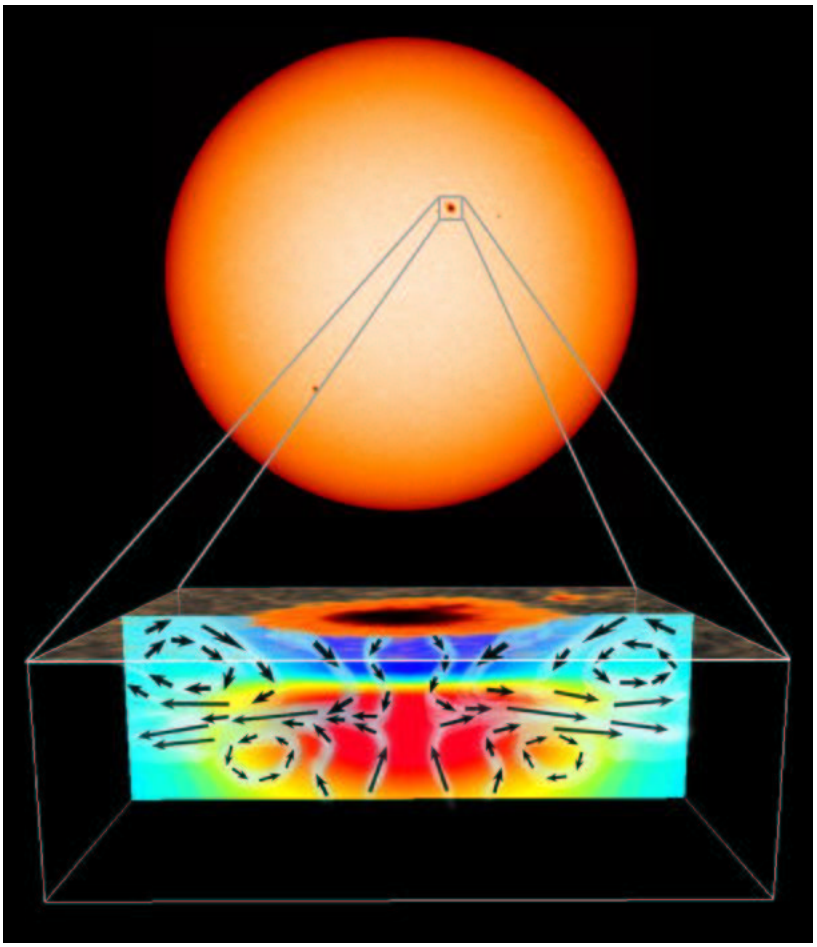

Figure 3.6: A cartoon showing both the sound-speed variations and the subsurface flow patterns of a sunspot (Courtesy: *SOHO*/MDI).

3.5 Discussion

We have presented our best estimates of the flows associated with a sunspot, and believe that these provide an accurate qualitative description of the flow pattern. Several factors could affect the accuracy of our results. It is unavoidable to have averaging effects between neighboring pixels and neighboring layers in our calculations. So, the flow speeds shown in Figures 3.4 and 3.5 can not represent the exact magnitudes, directions or locations, but some average values with their neighboring pixels and layers. Also, we have to bear in mind that the flows shown in Figures 3.4

and 3.5 are averages of 13 hours of observation. That means our inferences can only reflect flow patterns that are stable for a long time run rather than instantaneous speed at any observation time.

In our calculation, we assume that the travel time differences from time-distance analysis are totally due to mass flows, and we employ the geometrical ray approximation. Woodard (1997) and Birch & Kosovichev (2000) argued that some other factors, such as non-uniform distributions of acoustic sources and finite wavelength effects, may also affect travel times, which may greatly complicate our analysis, in particular, quantitative inferences.

In both graphs of Figure 3.5, powerful converging and downward flows are found from 1.5 Mm to ∼5 Mm beneath the surface. Meyer et al. (1974) predicted the existence of the converging flow (∼1 km/s at a depth of several Mm) as a collar

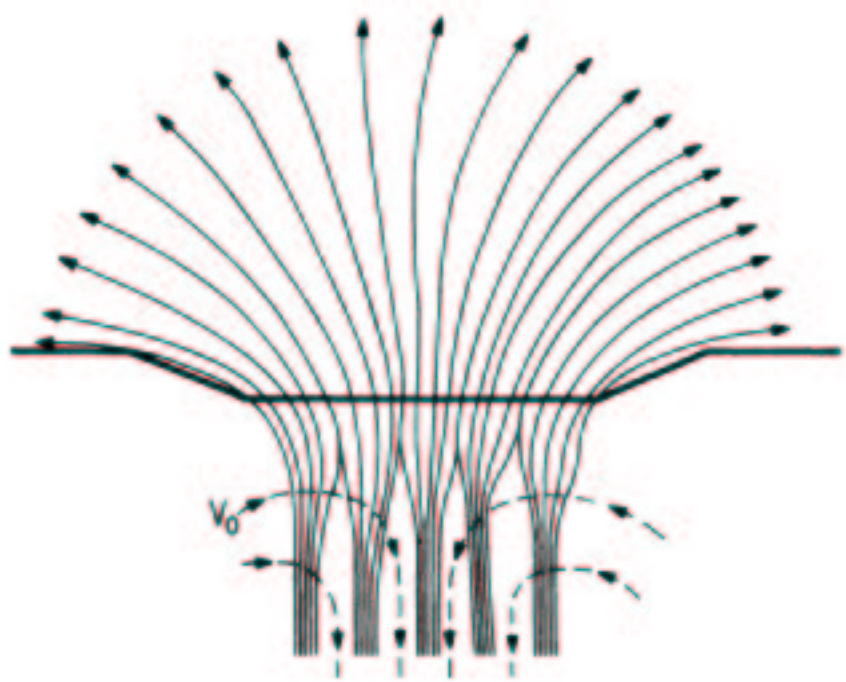

Figure 3.7: The cluster model of sunspots proposed by Parker (1979). This plot is adopted from that paper.

around the sunspot to provide the confinement and stability of sunspots. The material downdrafts below the sunspot were also required to keep the cluster of magnetic fluxes confined under the sunspot in the cluster sunspot model (Parker, 1979), as shown in Figure 3.7. Our observation seems to have provided strong evidence for both predictions. More recent numerical simulations (Hurlburt & Rucklidge, 2000) show in more detail the converging and downward flows below the sunspot surface, and the upflow near the moat, which are in good agreement with our observation not only in the converging and downward flows, but also in upflows near the moat (a little weaker in our results than the simulation). The converging and downward flow beneath the sunspot cannot be immediately consistent with the other observed facts of upward and diverging flows at the surface, as described in §3.1. Further studies of the shallow region from the surface to a depth of 2 Mm should be done more carefully by combining the f mode observations (Gizon, Duvall, & Larsen, 2000).

Besides the cluster model, the monolithic model is another widely proposed sunspot model. It suggests that the sunspot is one large magnetic flux tube below the photosphere rather than dividing into some small flux tubes. If this is true, one should expect no material can flow across the monolithic magnetic tube. But our results in Figure 3.4c shows otherwise. This may be a further evidence to support the cluster model, which does not prohibit mass flow across the lower part of a sunspot.

It is clear that magnetic inhibition of convection is most effective within 1.5 Mm of the photosphere (Thomas and Weiss, 1992). The temperature difference, ΔT, between the sunspot umbra and the mean undisturbed atmosphere at the level of the Wilson depression is about 900K, but ΔT decreases rapidly with depth. The estimated value of ΔT falls to 500K at depth of 2 Mm, and then to 25K at depth of 6 Mm (Meyer et al., 1974). The sunspot would be a shallow phenomenon if it were defined by its thermal properties alone. Our calculation of flows shows that converging and downward flows disappear below the depth of $\sim$5 Mm, which is an approximate depth where ΔT vanishes. So, it may be interpreted that, the converging and downward flows beneath the sunspot are phenomena related to the sunspot's thermal properties. These flows disappear as the temperature difference of the sunspot with its surroundings vanishes.

It is widely believed that a sunspot is formed when the magnetic Ω loop rises from

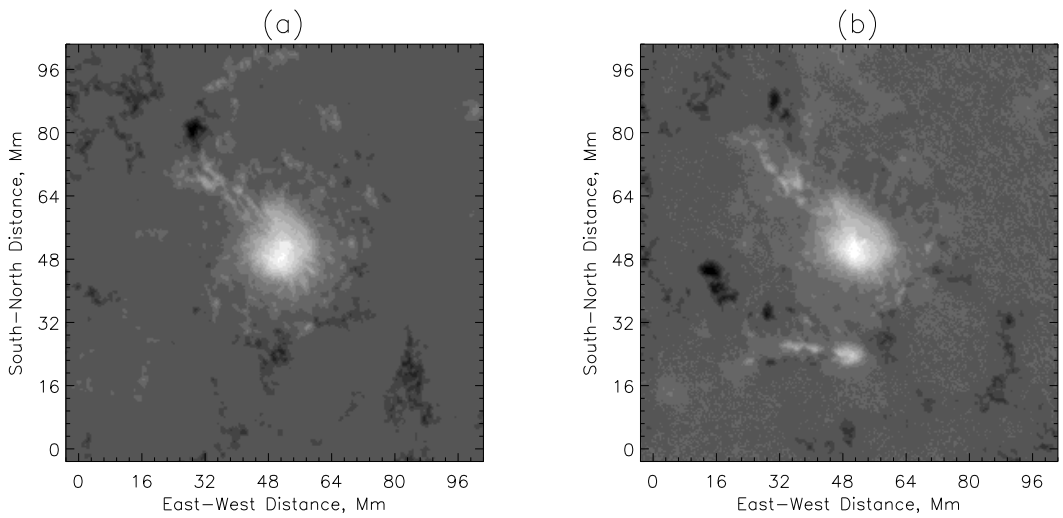

Figure 3.8: Magnetograms taken by MDI at (a) 04:30UT and (b) 22:00UT on June 19, 1998.

the deeper convection zone and emerges at the solar surface. The sunspot is located where the Ω loop emerges and where strong magnetic flux bundles concentrate. The flux bundles will stop rising after the sunspot reaches its maximum, but plenty of other magnetic flux keeps rising from the convection zone at the local site (Parker, 1994). There must be plenty of magnetic flux tubes which are underlying the sunspot but do not emerge on the surface despite of magnetic buoyancy. Figure 3.4c shows a strong mass flow across the sunspot, if some magnetic flux tubes underlying the spot are blown away to the South-East of the sunspot, and brought up by some upflows (some strong upflows can be found at the lower left corner of Figure 3.4c), magnetic emergence at the surface will be expected after ∼4 hours (from a depth of 9–12 Mm, the rising speed is around 0.7 km/s). We checked MDI full-disk magnetograms, and found about 5 hours after our analysis period, at 09:40UT of June 19, a magnetic emergence was first seen at the exact site of the upflows seen in Figure 3.4c. The pores with opposite polarities developed into their maxima after 12 hours. Figure 3.8 shows the magnetogram before the magnetic emergence and after it reaches the maximum. The sound-speed perturbation analysis of the same sunspot by Kosovichev, Duvall, & Scherrer (2000) revealed that the sunspot is connected with the pore of same

polarity in the deep interior, which may confirm our assumption that these two newly emerged pores were formed by rising Ω loops which might have broken away from the main magnetic flux bundles. We have also noticed another fact that the proper motion of this sunspot during the observation is towards the South-East. It may be caused by the South-East directed motion of the lower portion of the sunspot seen in Figure 3.4c due to an unknown reason. Obviously, more high-resolution helioseismic observations are required to confirm these results. Such observations could offer a unique opportunity for solving one of the great puzzles of astrophysics − the origin of sunspots.

Chapter 4

Dynamics of A Rotating Sunspot[1]

4.1 Introduction

Sunspots that exhibit some degrees of rotational motion around its own vertical axis are not rare in solar observations (Knoška, 1975). Many authors (e.g., Tokman & Bellan , 2002) suggested that some solar eruptive events, such as solar flares and coronal mass ejections, are correlated with rotational and sheared motions of sunspots. Recently, Brown et al. (2003) studied several rotating sunspots observed by *TRACE*, and calculated the total magnetic helicity and energy generated by the sunspot rotation. They found that the sunspot rotation can twist coronal loops and trigger solar flares. On the other hand, many authors investigated the origin of the magnetic twists observed in vector magnetograms and coronal loop structures, and some explanations have been proposed including the solar differential rotation, surface motions and turbulent motions in solar convection zone (see review by Canfield & Pevtsov, 2000). More recently, based on analysis of 22 bipolar solar active regions, López Fuentes et al. (2003) proposed that the magnetic deformation may result from large-scale vortical flows in the solar convection zone and the photosphere or in subphotospheric layers. Therefore, it is of great importance and interest to investigate the subsurface structures and dynamics of rotating sunspots. These studies may shed light on

[1]Most part of this chapter was published in the Astrophysical Journal (Zhao & Kosovichev, 2003b)

physical conditions in the solar convection zone, the interaction between convective motions and magnetic structures of sunspots, the formation of magnetic twists, the energy storage for solar eruptions and many other interesting topics of solar physics.

In this chapter, we apply the method of time-distance helioseismology to a fast rotating sunspot observed by *SOHO*/MDI in August 2000, and present maps of subsurface flows and sound-speed variations. We demonstrate that the structural twist of magnetic flux exists below the photosphere, as argued by Leka, Canfield, & McClymont (1996); and we present the subsurface vortical flows which may further twist the magnetic flux and store more magnetic energy and magnetic helicity required by solar eruptions. In this chapter, we also show some error analysis and do the mask experiment to test the reliability of our inversion results.

4.2 Observations

4.2.1 MDI Observations

The full-disk Dopplergrams with one-minute cadence used for our analyses were obtained from *SOHO*/MDI (Scherrer et al., 1995). The spatial resolution is 2 arcsecond, corresponding to 0.12 heliographic degree per CCD pixel.

Active region NOAA 9114 passed through the solar disk from August 4 to August 12, 2000. The movie made from the MDI magnetograms with a temporal interval of 96 minutes from August 6 to August 10 showed in this active region a fast rotating leading large sunspot, and a small satellite sunspot moving closer to the leading sunspot and merging with it on August 8. After the merge the sunspot continued its rotation until August 10. The sunspot's rotation is clearly seen because the larger sunspot is not completely round, but has a protruding feature "A", as marked in Figure 4.1. It shows counter-clockwise rotation around the main sunspot. Although rotation of sunspots is not rare in solar observations, this case of such a rapid and large degree rotation (approximately 200° within 3 days) is rather unusual.

Figure 4.1 shows a magnetogram obtained by *SOHO*/MDI at 16:11UT on August 7. The path of the small sunspot from 00:00UT, August 6 to 08:00UT of August 10

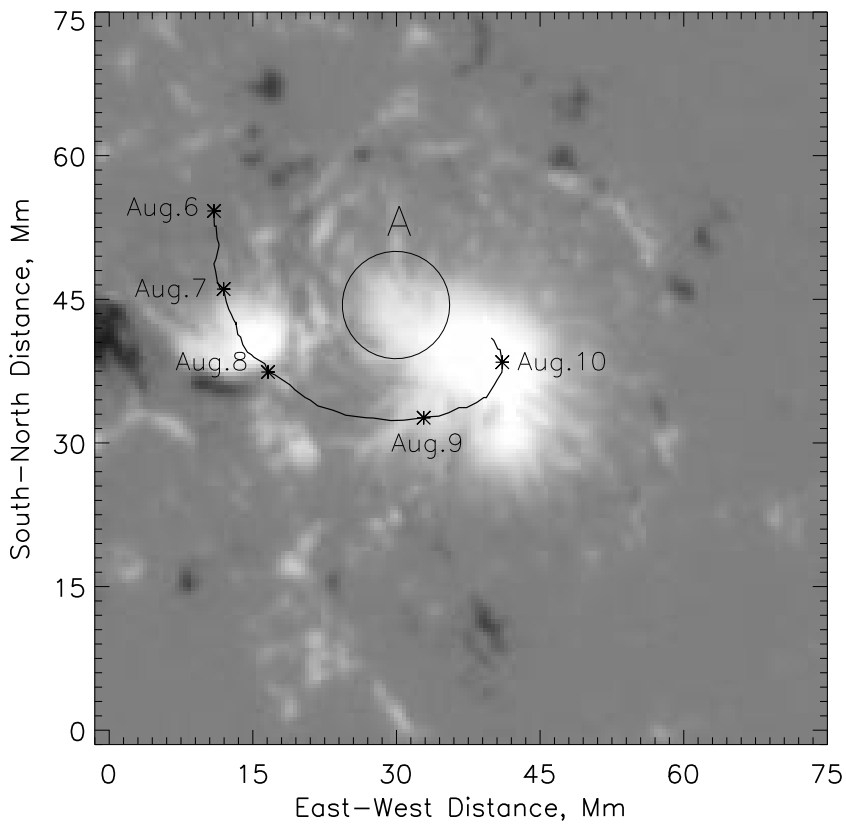

Figure 4.1: Line-of-sight magnetogram obtained by *SOHO*/MDI at 16:11UT of August 7, 2000. The solid line shows the path of the small sunspot from 00:00UT August 6 to 08:00UT August 10. Asterisks mark the 00:00UT of August 6 through August 10 respectively. The protruding part from the larger sunspot in the circle is marked as feature "A". The magnetic field strength ranges from -1100 to 1600 Gauss.

is plotted as a solid line in Figure 4.1, with asterisks marking 00:00UT of every day from August 6 to 10. The small sunspot moved along a curve rather than a straight line before the merge, and after merging with the larger sunspot, it rotated together with this sunspot.

4.2.2 Observations by *TRACE* and Mees Observatory

The *Transition Region and Coronal Explorer (TRACE)* (Schrijver et al., 1999) also gave continuous observation of this interesting event from Aug. 8 to Aug. 10 both in white light and in 171Å. *TRACE* has a spatial resolution of 0.5 arcsec, better than SOHO/MDI full disk observation. Figure 4.2 shows an image of *TRACE* 171Å observation of this active region, with the contours showing the boundaries of the penumbra and umbra of this sunspot. The magnetic loops above the sunspot shows a so-called "fan" structure, which means that the magnetic loops deviate from their potential field.

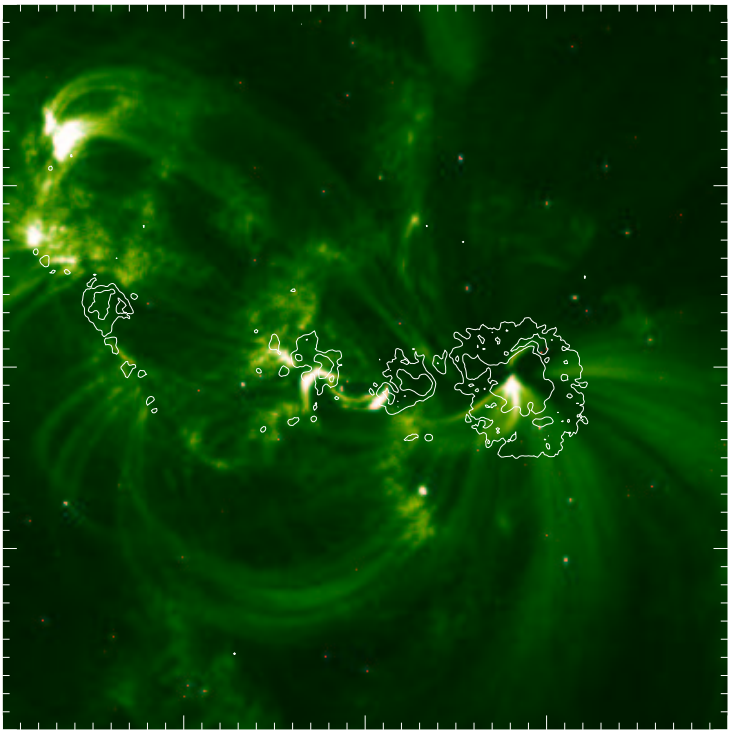

Figure 4.2: *TRACE* observation of this active region. The image is 171Å observation by *TRACE*, and the contour is from white light observation showing the boundary of umbra and penumbra of the sunspot. The scale of this graph is 138 Mm × 138 Mm.

The Imaging Vector Magnetogram (IVM) at Mees Solar Observatory (Mickey et al., 1996) observed the transverse magnetic field of this active region. Figure 4.3 shows

the transverse magnetic field overlapping white light image of the sunspot. Obvious counter-clockwise transverse magnetic field twists deviating away from the potential field can be seen on the right hand side of the sunspot's center. The observations of August 7 and 9 also show some twists in transverse magnetic field, but the twists are not so strong as on August 8.

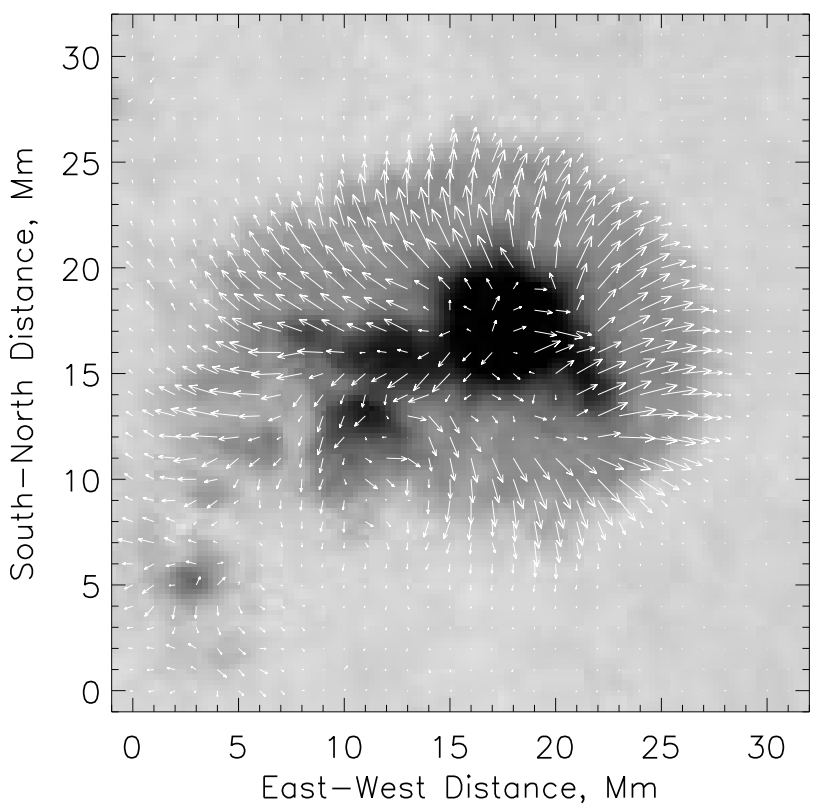

Figure 4.3: Transverse magnetic field, shown by arrows, overlapping the white light image from the Mees Solar Observatory. The longest arrow represents the magnetic strength of 1100 Gauss.

4.2.3 Time-Distance Measurement and Inversion

To perform the time-distance helioseismology measurements with an acceptable signal-to-noise ratio, we select the following two observing periods, both of which last 512 minutes, for our time-distance analyses: 16:20UT August 7 – 00:51UT August 8, 2000 and 04:08UT – 12:39UT August 8, 2000 (for simplicity, we refer to them as August 7 data and August 8 data respectively).

Time-distance measurements and inversions were then performed following the procedures described in Chapter 2. In Chapter 3, we tested the accuracy and convergence of the LSQR algorithm using artificial data, and found that this technique can recover three-dimensional flow structures up to 15 Mm beneath the visible surface. Moreover, in §2.3, we demonstrated the inversion results obtained by LSQR algorithm agree well with the inversion results from Multi-Channel Deconvolution. The results that are to be presented in the following were inverted using LSQR algorithm and MCD technique was employed to ascertain the results.

Here, we present some additional inversion tests for noise-free artificial data to estimate the ability of the LSQR-based inversion technique to measure vortical flows and detect opposite flows within relatively short depth ranges. The upper panels of Figure 4.4 show the original artificial data, with downward and converging counter-clockwise vortical flows at the depth of 0 – 3 Mm, and upward and diverging clockwise flows at the depth of 9 – 12 Mm. The lower panels show the inversion results from the artificial data following the procedure in Chapter 3. We can find that the inversion results reproduce very well the flow patterns of the artificial data, with the correlation coefficient as high as 98.9% for the depth of 0 – 3 Mm, and 94.7% for 9 – 12 Mm.

4.3 Results

4.3.1 Results of Sound Speed Variation

Previous observations have shown that the average sound-speed variation $\delta c/c$ relative to the quiet Sun is mostly positive below the depth of $\sim$4 Mm in active regions (Kosovichev, Duvall, & Scherrer, 2000; Sun et al., 2002). We may assume that the

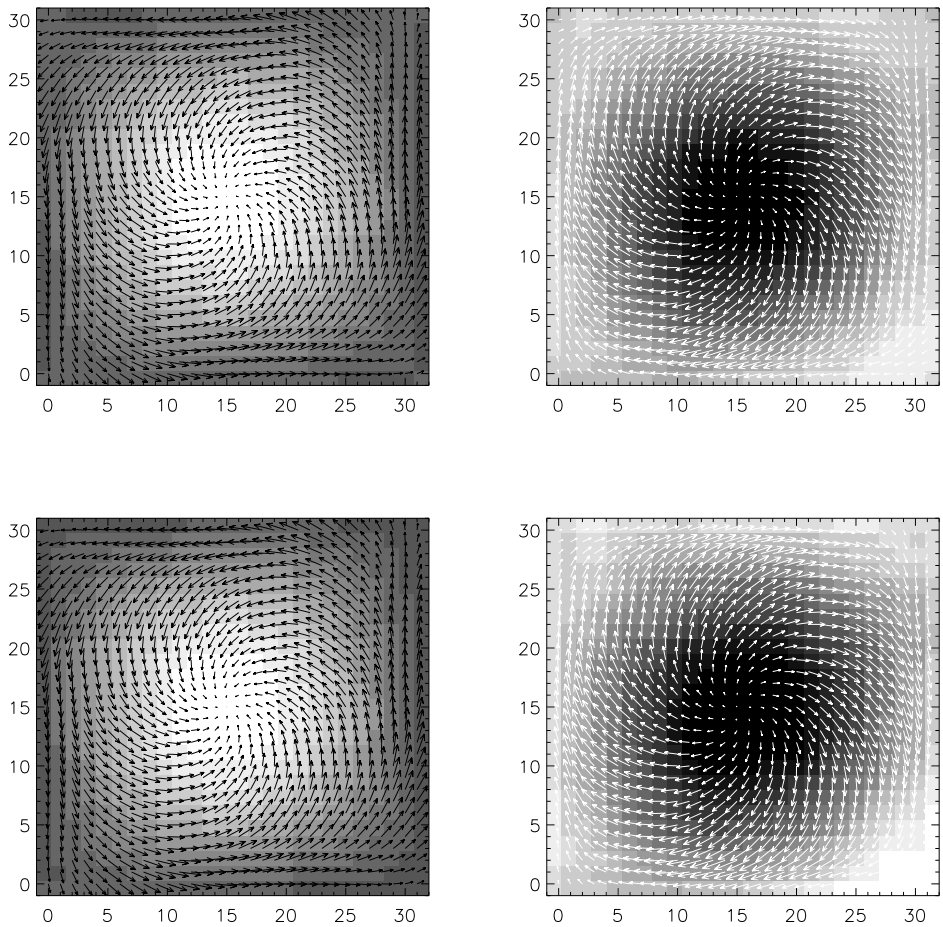

Figure 4.4: Test results from noise-free artificial data. Background images in each graph represent the vertical velocities, with bright as upward flows and gray as downward. Arrows indicate the horizontal flows. The upper two graphs are the artificial data for the depth of 0 – 3 Mm (*left*) and 9 – 12 Mm (*right*) respectively, and the lower two graphs are the inversion results. Scales are arbitrary in these graphs.

horizontal shape of the subsurface sound-speed variation corresponds to the shape of the subsurface magnetic field structure, however, the precise relation between them has not yet been established.

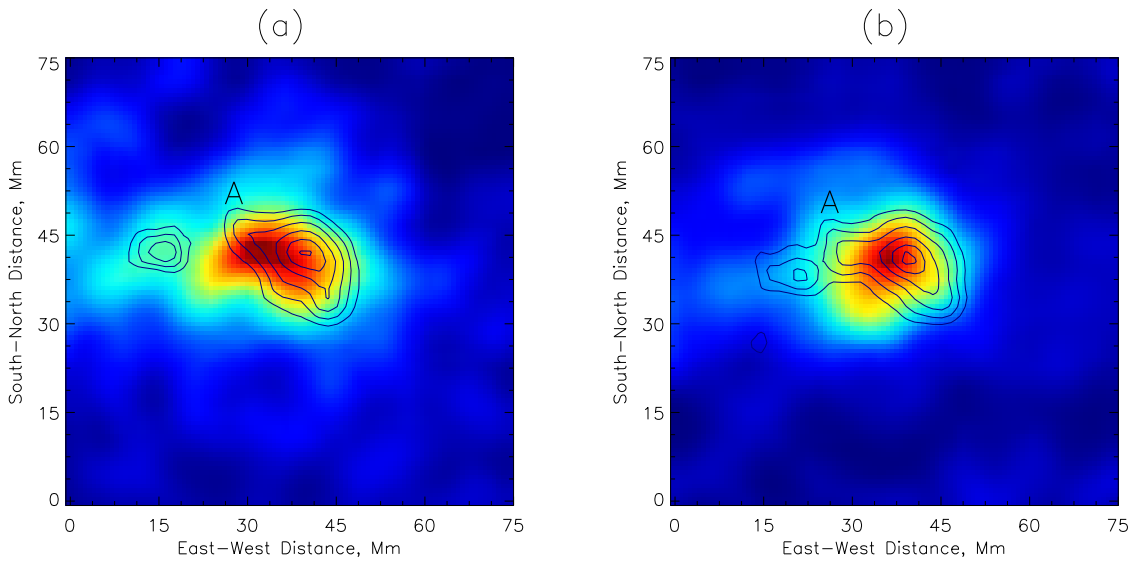

Figure 4.5: Sound-speed variation maps at the depth of 6 Mm (background color images) and the photospheric line-of-sight magnetic field (contour lines) for two observing intervals: a) 16:20UT August 7 – 00:51UT August 8, 2000; b) 04:08UT August 8 – 12:39UT August 8, 2000. The red color corresponds to positive sound-speed variation $\delta c/c$, and the blue one corresponds to negative $\delta c/c$ which ranges from -0.02 to 0.08. The contour levels are 600, 800, 1000, 1200, 1400, 1600 Gauss.

In Figure 4.5a, the background image shows the sound-speed variation structure at the depth of 6 Mm, obtained from the August 7 data. The contour lines in this graph show the line-of-sight magnetic field averaged from all 1-minute cadence magnetograms during the 512-min observation period. Even though the exact correspondence between the photospheric structures and the subsurface sound-speed structures cannot be easily seen, it appears that the subsurface structure is rotated by $\sim$34° counter-clockwise with respect to the photospheric sunspot structure. The root of the small sunspot which eventually merged with the larger sunspot is not identified as a separate structure in our data. This may imply that the root of the small satellite sunspot was probably connected to the magnetic flux clusters of the main sunspot deeper than the depth of a few megameters (see also, Kosovichev, Duvall, & Scherrer, 2000).

Figure 4.5b shows the sound-speed variation map and the averaged line-of-sight

magnetic field from the August 8 data. In this case, the shape of the sound-speed variation is not in the same good accordance with the shape of the surface magnetic field as in Figure 4.5a. However, the protruding part of the sound-speed structure seems to correspond well to feature "A" on the surface, thus forming an angle of $\sim 45°$ between these features. These observations seem to suggest the existence of the subsurface structural twist of the sunspot in both datasets.

4.3.2 Flow Fields Beneath the Surface

Three-dimensional velocity maps have also been obtained from the August 7 and 8 data. The left panels of Figure 4.6 present the velocity fields at two depth intervals of 0 – 3 and 9 – 12 Mm obtained from the August 7 data, while the right panels show the velocity fields at the same depth intervals for the August 8 data.

In the upper layer (0 – 3 Mm in depth), we find strong converging flows with downdrafts in the sunspot area, as found by Zhao, Kosovichev, & Duvall (2001). Except for the lower left corner (or the southeast part) of the main sunspot, an apparent counter-clockwise vortical flow can be found around the sunspot for both dates August 7 and 8, with stronger vorticity on August 8. This vortex has the same counter-clockwise direction as the sunspot surface rotation. Similar vortical flow patterns are found at the depth of 3 – 5 Mm, which implies that the rotational motions seen at the surface extends to 5 Mm in depth.

In the deeper layer (9 – 12 Mm in depth), we observe that divergent flows with upward flows replace the converging downflows in the sunspot area. A strong clockwise vortex can be seen in the August 8 graph (Figure 4.6d) in and around the sunspot region. The August 7 data (Figure 4.6b) also show this vortex but of a smaller vorticity. It appears that the direction of the vortex seen at this depth is opposite to the surface rotation of the sunspots.

In order to show more clearly the vortical flows in and around the sunspot region, we present in Figure 4.7 the tangential components of the velocities relative to the center of the sunspot at two different depths from August 8 data.

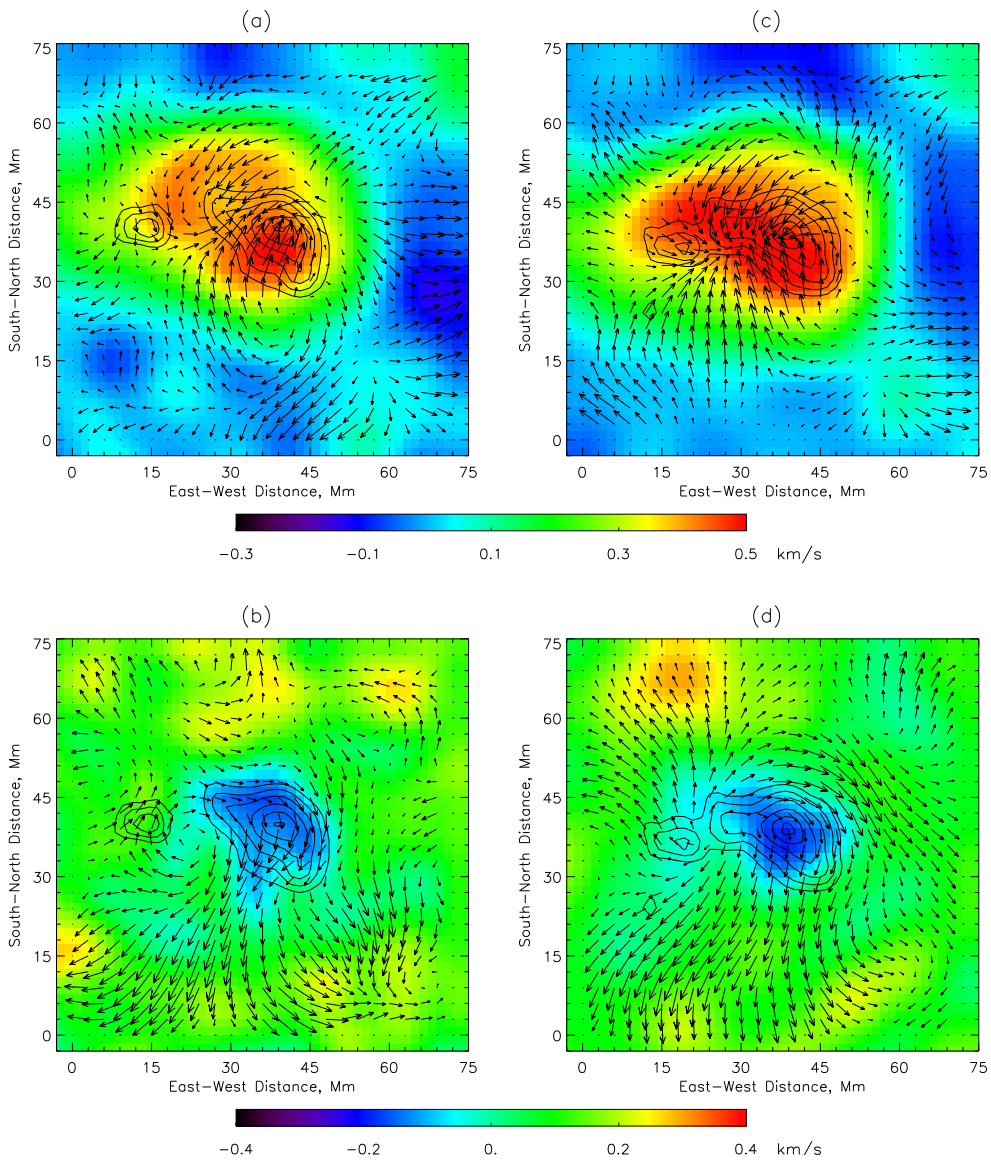

Figure 4.6: Flow fields obtained at two different depths. In the left panels, the background image shows the vertical velocities, and arrows represent the horizontal velocity field obtained from the August 7 data at the depth intervals: a) 0 – 3 Mm, and b) 9 – 12Mm. The right panels show the results for the August 8 data with same depth intervals: c) 0 – 3 Mm, and d) 9 – 12Mm. The longest arrow is 0.5 km/s for both the upper and lower graphs. The contour lines represent the line-of-sight magnetic field, the same as in Figure 4.5.

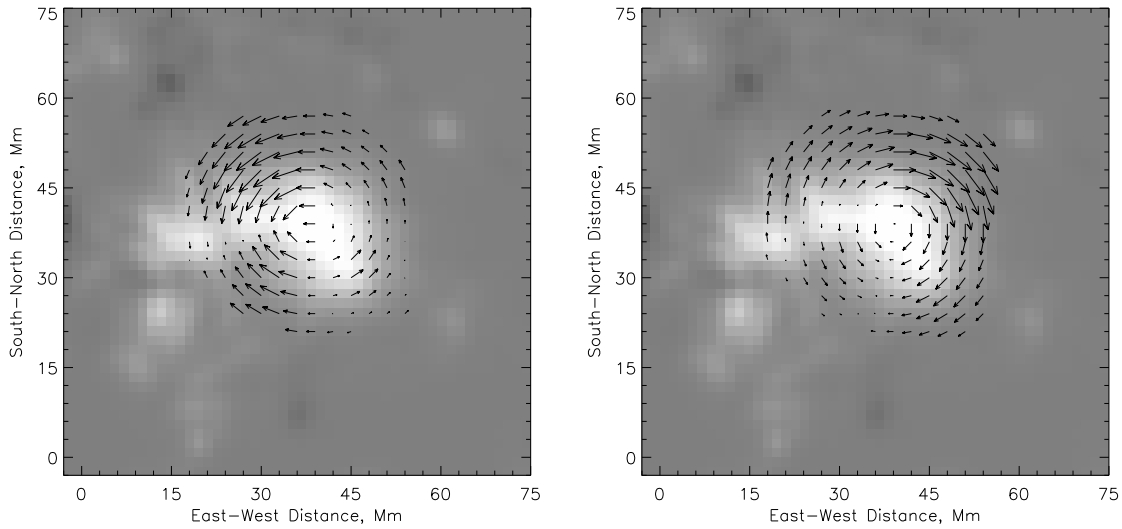

Figure 4.7: The tangential components of flow velocity relative to the center of the sunspot at two different depths 0 – 3 Mm (*left*) and 9 – 12 Mm (*right*) obtained from the August 8 data. The background images show the magnetic field same as the contour in Figure 4.5. Longest arrow in both graphs represents a speed of 0.45 km/s.

4.3.3 Kinetic Helicity

The three dimensional velocity field obtained from our time-distance helioseismic inversions enables us to estimate the kinetic helicity of the subsurface flows, which is an important characteristic quantity for solar MHD .

Following Mestel (1999), we define the kinetic helicity as

$$\alpha^v \equiv \mathbf{v} \cdot (\nabla \times \mathbf{v})/|\mathbf{v}|^2 \tag{4.1}$$

In particular, we use a component of α^v corresponding to the vertical components of velocity and vorticity:

$$\alpha_z^v = v_z(\partial v_y/\partial x - \partial v_x/\partial y)/(v_x^2 + v_y^2 + v_z^2) \tag{4.2}$$

This corresponds to the current helicity obtained from magnetograms by some previous authors, e.g., Pevtsov, Canfield, & Metcalf (1995). After computing value α_z

at each pixel, we average these values over the whole active region where $B_z > 100$ Gauss, although the selection of 100 Gauss threshold is arbitrary. The mean kinetic helicity from the August 7 velocity data (Figure 4.6a, b) is -1.01×10^{-8} m^{-1} for the depth of 0 – 3 Mm, and -2.21×10^{-8} m^{-1} for the depth of 9 – 12 Mm, and the mean kinetic helicities for August 8 data (Figure 4.6c, d) are -2.11×10^{-8} m^{-1} and -6.26×10^{-8} m^{-1}, respectively.

Based on the observations of vector magnetograms in solar active regions, Pevtsov, Canfield, & Metcalf (1995) calculated the mean current helicity of many active regions with the definition of current helicity as $\alpha = J_z/B_z$, where J_z is the line-of-sight current density and B_z is the line-of-sight magnetic field. The average kinetic helicity calculated from our inversion results of this active region has the same order of magnitude as the typical current helicity of active regions calculated by them. It is suggested by many authors (e.g., Longcope, Fisher, & Pevtsov, 1998) that the magnetic helicity observed in the photosphere may be produced by helical motions beneath the photosphere. However, we can hardly draw any conclusion about the relationship between the subsurface kinetic helicity and magnetic helicity from just one sample that we currently have. Apparently, a statistical study combining the kinetic helicity and magnetic helicity is needed for better understanding this relationship in solar active regions.

4.4 Error Analysis

4.4.1 Monte Carlo Simulation

The inverse problem of the time-distance helioseismology is reduced to the linear system $\mathbf{Ax} = \mathbf{b}$, which is solved in sense of least squares. The covariance matrix for error estimations of the inversion results is given by $C_m = \sigma_d^2(\mathbf{A}^T\mathbf{A})^{-1}$ (see Menke, 1984), where σ_d^2 is the covariance matrix from the observation data. However, it is not realistic to perform such a calculation because $(\mathbf{A}^T\mathbf{A})^{-1}$ is too large to calculate directly, and the LSQR algorithm does not give the matrix inverse explicitly, nor does the other algorithm MCD. Therefore, we estimate the error propagation by the use

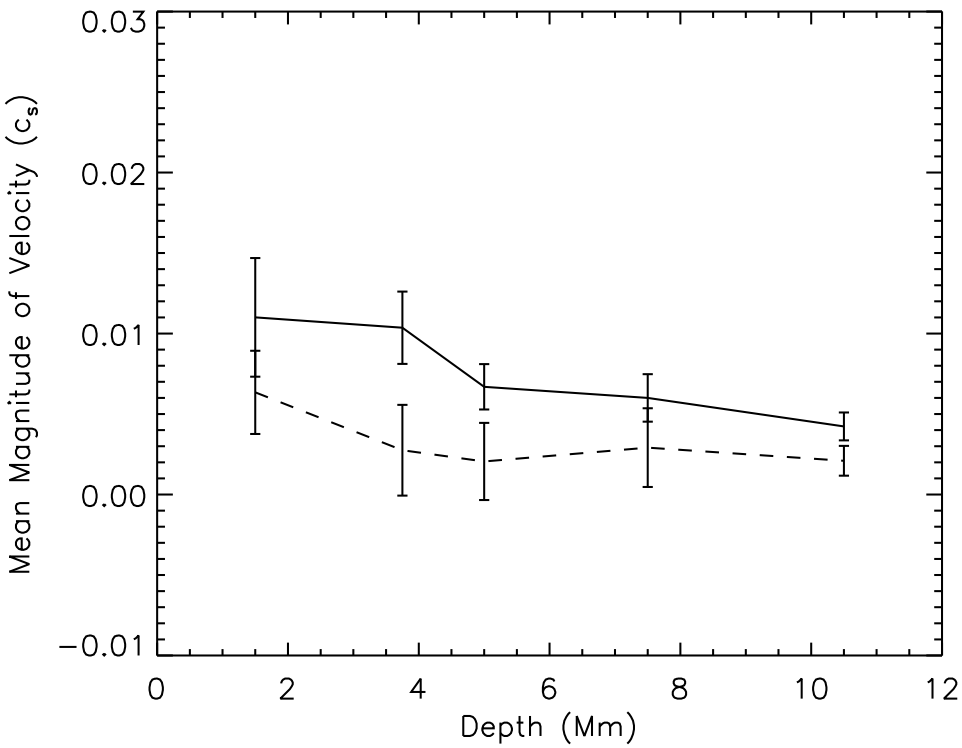

Figure 4.8: Mean magnitude of the horizontal (solid line) and vertical (dashed line) components of flow velocity at different depths with the error bars estimated by a Monte Carlo simulation. The velocities are shown in the unit of local sound-speed.

of Monte Carlo simulation.

Time-distance helioseismology calculates the wave propagation time by fitting cross-covariance of the solar oscillation signals in two locations; hence, a fitting error of the propagation time can be estimated at each pixel for different travel distances by following the description by Press et al. (1992). Typically, the fitting errors are less than 2% of the wave propagation time. However, only the travel time differences are used for the inversion, which are relatively small and therefore, have significant error levels. For larger distances, we use larger annulus intervals in which more data points are included, and in this case fitting errors are usually smaller than those from smaller distances. This is done in order to increase the reliability of the inferences

for deeper layers. Then, for each specific distance, we approximate the fitting error distribution by a Gaussian function. Although the exact distribution function for the travel time fitting errors is not exactly known, to the observed distributions the Gaussian function is a good approximation.

After the distribution function of fitting errors is obtained for each distance, we perform Monte Carlo simulation by producing 40 sets of random errors consistent with the error distribution function and adding these to the travel time estimates for August 8 data. The time-distance inversion for three dimensional velocity is performed for each of these 40 datasets, respectively. After the inversion is done, the mean value and standard deviation are computed for each pixel of the velocity maps. In Figure 4.8, the average of mean values of the horizontal and vertical components of velocity are presented, and the error bars indicate the average of standard errors at different depths. We find that the results for the horizontal component of velocity are robust, while the vertical component of velocity is more uncertain (we even have difficulty in determining the correct signs at the depth from 3 to 6 Mm). However, in the depth intervals $0 - 3$ and $9 - 12$ Mm, which are used in our analysis of the vortical flows (shown in Figure 4.6), the errors are relatively small.

4.4.2 Umbra Mask Test

The other issue that we need to consider is the *SOHO*/MDI observation saturation problem in dark areas of sunspots umbrae (Liu & Norton, 2001), which appears in MDI magnetograms and Dopplergrams observations when the spectral line intensity drops below a certain level. Additional effect that may affect our measurements is a strong absorption of the solar acoustic power by sunspot umbrae (Braun, Duvall, & LaBonte, 1988).

In order to test how the saturation and the acoustic absorption in sunspot umbra might affect the vortical flow fields derived from our analysis, we discard all the travel times obtained inside the sunspot umbra, and then perform the inversion calculations, although only a small part of the umbra is affected by the saturation. The results are shown in Figure 4.9. We find from the masked data that at the depth of $0 - 3$

Mm, the downward flow speeds are only slightly smaller than those in the original calculation, and the horizontal speeds also slightly change, but most importantly, the flow structure is not affected. We still see the same downward and converging flow patterns, thus confirming the earlier conclusion obtained in Chapter 3. Outside the sunspot umbra, the vortical flows seen in Figure 4.6 remain almost the same. At the depth of 9 – 12 Mm, the flow fields are not affected at all by the umbral mask. Therefore, we conclude that the potential uncertainties in the observations of the umbra area do not significantly affect our results.

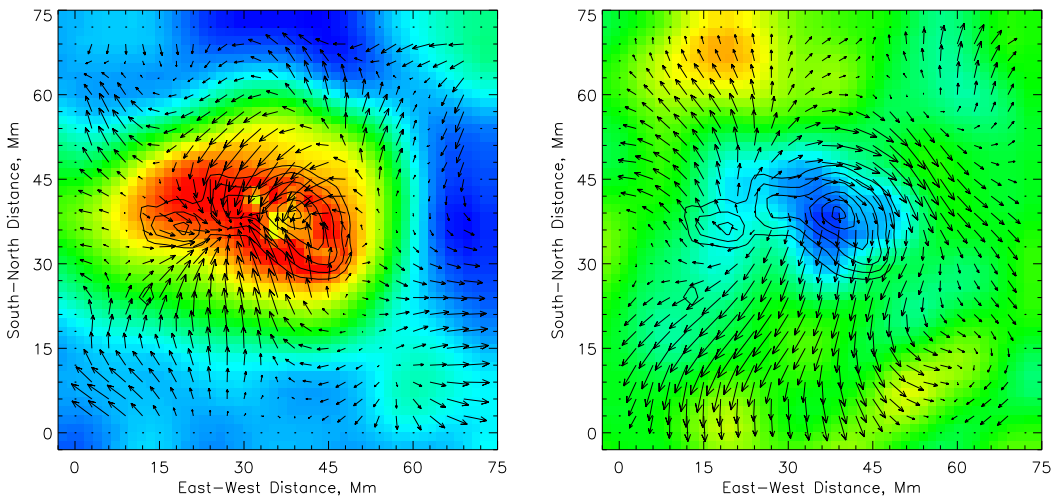

Figure 4.9: Flow fields derived for August 8 data after masking the sunspot umbra (see text). Color index and arrows are same as in Figure 4.6.

4.5 Discussion

Using the time-distance technique and inversion methods based on the ray approximation, we have mapped the sound-speed structures and flow fields beneath a rotating sunspot. We have estimated the error propagation in both the time-distance measurements and the inversion procedure by the use of Monte Carlo simulations, and found that while the vertical velocity inferences may have significant errors, estimates of the horizontal component are sufficiently robust for determination of the structure

of the vortical flows. The test of masking the sunspot umbra where the measurements may be uncertain because of the observational signal saturation and wave absorption showed only slight changes in both components of the velocity in the sunspot area close to the surface and nearly no change in the deeper layers. Perhaps, the main uncertainty of our measurements comes from the ray approximation in the inversion procedure, which is known to underestimate the magnitude of perturbations, particularly at small scales (Birch et al., 2001). However, the larger scale structure of sunspots should be reproduced correctly (Jensen et al., 2001). Hence, results shown in this chapter are correct qualitatively, if not quantitatively.

Many previous observations have revealed that the magnetic field in some active regions is twisted. Evidence for the twists exhibits in various solar phenomena, such as the morphology of Hα structures (Hale, 1927), filaments (Martin, Billamoria, & Tracadas, 1994) and coronal loops (Rust & Kumar, 1996). The results presented in Figure 3 show us that the surface magnetic field of a rapidly rotating sunspot has an angle with respect to the subsurface sound-speed structure at the depth of 6 Mm. This provides observational evidence that the magnetic flux twists also exist beneath the visible surface of the active region, in addition to the previously reported twists in the solar photosphere and corona. Furthermore, it was argued that the magnetic field twists may have already formed before the emergence of magnetic flux on the surface (Leka, Canfield, & McClymont, 1996, and many other investigators). Our observation presents direct evidence that magnetic field twist may exist beneath the surface.

Assuming that the magnetic flux tubes have already been twisted below the solar surface, Magara & Longcope (2003) simulated numerically the emergence process of magnetic flux and reproduced the sigmoidal shape of coronal loops as observed in X-rays. In addition, vortical flows in and around the magnetic flux footpoints were also found in their simulations, which in turn could twist more the already twisted magnetic flux. Our observation of sunspot rotation in the photosphere and 5 Mm below the photosphere seems to be consistent with their numerical simulation for both the subsurface magnetic twists and the photospheric and subphotospheric vortical motions. Perhaps, our inference of the subsurface vortical flow fields in this

study may also support the argument by López Fuentes et al. (2003) that vortical flows may exist in subphotosphere and play an important role in the formation of magnetic twists.

It is widely believed that vortical sheared flows around magnetic flux footpoints could eventually lead to solar eruptions. Recently, some authors began to calculate the energy and magnetic helicity generated by the surface flows. Some argued that the surface horizontal rotational flows could provide sufficient magnetic helicity and energy to produce solar flares (Moon et al., 2002), while others argued that magnetic helicity from subsurface must be included to be sufficient for solar eruptions (Nindos & Zhang, 2002). Our observation shows that strong subsurface vortical flows should be taken into account as a potential source of magnetic helicity and energy buildup, which can be much stronger in the deeper layers than at the surface because mass density and plasma β are much higher there.

In this study, we have found counter-clockwise vortical flows at the depth range of $0 - 3$ Mm around the sunspot (which also rotated counter-clockwisely at the surface), and the evidence of reverse clockwise flows at the depth of $9 - 12$ Mm. What could cause these opposite vortical flows is an open question. At present there is no theoretical model explaining the vortex motions. It may be useful to consider some analogies, for instance, it is known that for hurricanes on the Earth there are strong converging flows near the ocean surface, and divergent flows at high altitude in the atmosphere. Hence, the hurricanes have counter-clockwise flows at the bottom and clockwise flows at the top due to the Coriolis force on the Earth's northern hemisphere (e.g., Gordon, 1998). If one can think of a sunspot model as a reverse hurricane as proposed by Schatten & Mayr (1985), then the opposite vortical flows may be caused by Coriolis force. If this were the case, then magnetic flux can be twisted by these flows, hence build up a great amount of energy. However, if the reverse hurricane sunspot model is true, the question is why the vortical flows are not observed in most sunspots.

By using the time-distance inferences, we have also calculated the subsurface kinetic helicity in two different depth intervals, and obtained the kinetic helicity values of the same order of magnitude as the current helicity of typical active regions. It is

reasonable to believe that kinetic helicity and magnetic helicity are related to each other in the sub-photosphere and upper convection zones, and the subsurface kinetic helicity may have some contributions to the formation of surface magnetic helicity and its hemispherical preference distribution. Certainly, how the subsurface kinetic helicity are correlated with the surface magnetic helicity needs a further statistical study. The time-distance inversion technique and results presented in this chapter enable us to carry out such study.

Further time-distance helioseismological studies of the subsurface dynamics of sunspots and active regions, particularly before powerful solar flares, may be of great importance for the investigation of the subsurface energy buildup, kinetic helicity development and their relationship with the solar eruptive events, and may lead to the possibility of solar eruptions forecast.

Chapter 5

Statistics of Subsurface Kinetic Helicity in Active Regions

5.1 Introduction

Observations have revealed that a hemispheric preference of magnetic chirality (handedness) exists throughout the solar atmosphere. Pevtsov, Canfield, & Metcalf (1995) used photospheric vector magnetograms of active regions from Mees Solar Observatory to compute the linear force-free field α-coefficient, and they found among 69 active regions studied α was negative (positive) in 69% (75%) of northern (southern) hemisphere active regions. Later analysis of more active regions showed similar results (Longcope, Fisher, & Pevtsov, 1998). Bao & Zhang (1998) used vector magnetograms from Huairou Solar Observing Station to compute current helicity density h_c of 422 active regions, and found that 84% (79%) of active regions in northern (southern) hemisphere had negative (positive) h_c. It was found more recently that α-coefficient and h_c for active regions in Solar Cycle 23 retain a similar hemispheric preference as in Solar Cycle 22 (Pevtsov, Canfield, & Latushko, 2001).

Besides statistical work on vector magnetograms, statistics were also done on the shapes of sigmoidal coronal loops. Canfield & Pevtsov (1999) studied X-ray images from the *Yohkoh* soft X-ray telescope, and found that 59% (68%) of sigmoidal coronal loops displayed an inverse-S (S) shape in the northern (southern) hemisphere.

Hα analysis of solar filaments in the chromosphere gave similar results (Pevtsov, Balasubramaniam, & Rogers, 2003).

Several mechanisms have been proposed to explain the observed hemispheric preference, such as differential rotation (e.g., DeVore, 2000), dynamo models (Gilman & Charbonneau, 1999), and the non-vanishing kinetic helicity $\langle \mathbf{v} \cdot (\nabla \times \mathbf{v}) \rangle$ (here and after, $\langle\rangle$ means to compute the average, and $\mathbf{v}$ is velocity) in the turbulent convection zone (Longcope, Fisher, & Pevtsov, 1998). Although most work agrees that the formation of the magnetic chirality results from the kinetic helicity, no statistical work has been able to be performed so far to study the kinetic helicity in the solar photosphere and subphotospheric regions.

In the last two chapters, I have shown that time-distance measurement and its inversion can reveal the three-dimensional subsurface flow maps in active regions to a depth of approximately 12 Mm, which enables the computation of subsurface kinetic helicity. Therefore, a statistical study of subsurface kinetic helicity in solar active regions is feasible to investigate the relationship between subphotospheric kinetic helicity and photospheric magnetic helicity. Furthermore, it is also of great help in understanding the physical conditions in the convection zone and testing solar dynamo models.

In this chapter, I apply our time-distance technique on 88 sets of active region data taken between 1997 to 2002 by the MDI mission to infer their subsurface flow fields and compute the average subsurface kinetic helicity. The statistical results on the latitudinal distribution of kinetic helicity, relationship of kinetic helicity and magnetic strength are presented in this chapter.

5.2 Observations and Data Reduction

SOHO/MDI had around 2 months of dynamic campaign data each year from 1996 to the present, and provided nearly uninterrupted one minute cadence Dopplergrams, which are valuable to perform helioseismology studies. From these dynamic periods from 1997 to 2002 and a few other continuous coverage periods, we have chosen 77 active regions, and performed 88 sets of time-distance computations, with 9 active

regions computed in two different time periods, and 1 active region computed in three periods.

For all the 88 sets of data, we derived three-dimensional subsurface velocity fields, from which we then computed kinetic helicity $\alpha_v = \mathbf{v} \cdot (\nabla \times \mathbf{v})$. However, we adopted only the vertical component $\alpha_v^z = v_z(\partial v_y/\partial x - \partial v_x/\partial y)$ for computation, so that we can avoid the derivatives in vertical (z) direction where we have only a few layers. In addition, we can keep accordance with previous studies of current helicity, in which only the vertical component of current helicity was derived. Before computing the kinetic helicity, we removed the differential rotation from each set of data in order to exclude the vorticity caused by rotation. After computing the α_v^z values at each pixel in the selected active regions, we averaged all α_v^z where the magnitude of line-of-sight magnetic field is larger than 100 Gauss to obtain a mean value of kinetic helicity of this active region, although the selection of 100 Gauss is arbitrary. All the detailed information of the active regions and results of the averaged kinetic helicity are presented in Table 5.1 for the northern hemisphere and Table 5.2 for the southern hemisphere. In the tables, $\langle \alpha_{v1} \rangle$ and $\langle \alpha_{v2} \rangle$ represent the mean kinetic helicity at $0 - 3$ Mm and $9 - 12$ Mm, respectively. $\langle |\mathbf{B}| \rangle$ represents the mean magnetic field strength for each active region, and $\langle |\alpha_{v1}| \rangle, \langle |\alpha_{v2}| \rangle$ represent the mean magnitude of kinetic helicity at different depths.

Some previous authors (e.g., Pevtsov, Canfield, & Metcalf, 1995) estimated the errors of mean α-coefficient or current helicity by computing the same active regions a few times at different observation time. However, considering the observational requirements for time-distance studies (512 minutes uninterrupted observation with one minute cadence) and the heavy computational burden, it is not easy for us to estimate the errors of the kinetic helicity mean values by means of repeated computations of one active region at different observation times. Instead, we divide the active regions randomly into two equal halves, and compute the mean kinetic helicity separately for these two half regions, hence to estimate the errors of the mean kinetic helicity in one active region.

AR number	Date (mm.dd.yyyy)	Latitude (degree)	$\langle\alpha_{v1}\rangle$ (10^{-3}ms^{-2})	$\langle\alpha_{v2}\rangle$ (10^{-3}ms^{-2})	$\lvert\langle\mathbf{B}\rangle\rvert$ (Gs)	$\langle\lvert\alpha_{v1}\rvert\rangle$ (10^{-3}ms^{-2})	$\langle\lvert\alpha_{v2}\rvert\rangle$ (10^{-3}ms^{-2})
8036	04.26.1997	18.68	0.0064	0.30	167	1.18	3.84
8038	05.11.1997	20.48	0.24	0.24	419	3.51	7.63
8040	05.20.1997	5.17	0.039	-0.13	292	1.81	7.19
8040	05.22.1997	5.07	0.23	-0.28	292	2.36	5.68
8045	-	1.50	0.0098	5.65	237	0.56	7.80
8052	06.16.1997	18.00	0.16	-0.72	237	1.47	5.27
8071	08.11.1997	25.45	0.0032	1.90	193	1.30	4.35
8117	12.12.1997	30.36	-0.60	-2.57	314	3.09	6.23
8535	05.12.1999	21.67	0.086	0.52	275	2.10	8.43
8541	-	21.01	0.0093	1.95	250	2.58	14.92
8545	05.20.1999	36.58	0.59	-2.63	277	2.92	9.81
8552	05.28.1999	18.48	-0.0071	-1.03	300	2.06	7.30
8555	-	19.55	0.33	1.71	260	2.36	14.12
8582	06.16.1999	26.47	0.0073	0.69	282	3.61	6.68
8990	05.12.2000	13.83	0.16	-2.16	354	3.62	13.36
8994	-	17.05	-0.35	0.19	412	6.06	10.17
9002	05.20.2000	18.88	0.30	0.0046	405	4.75	10.81
9002	05.22.2000	18.88	0.59	1.37	357	3.44	8.51
9004	05.20.2000	10.90	0.36	0.23	479	7.26	11.86
9004	05.22.2000	10.90	0.18	1.86	351	4.56	11.56
9026	06.07.2000	21.02	-0.064	-1.19	296	2.72	6.33
9030	-	19.24	0.35	-7.59	475	5.66	10.97
9033	06.12.2000	22.40	-0.20	0.12	298	2.51	10.05
9039	-	6.69	-0.24	-1.22	334	1.92	7.69
9041	-	16.45	0.53	-0.14	301	2.27	7.66
9055	06.27.2000	20.12	0.20	-3.89	417	4.38	7.44
9057	-	14.05	-0.32	-3.36	538	6.88	14.4
9070	07.07.2000	18.71	-0.04	-0.75	315	2.46	6.58
9114	08.07.2000	9.41	-0.39	-2.53	363	5.61	8.79
9114	08.08.2000	9.41	-0.94	-6.76	372	4.84	11.78
9115	-	17.14	0.85	1.61	377	5.00	6.98
9236	11.23.2000	19.82	0.70	2.93	420	5.01	19.28
9236	11.24.2000	19.82	0.23	-1.62	404	5.61	17.86
9387	03.25.2001	8.71	0.32	2.43	280	2.22	8.42
9393	03.29.2001	17.43	-0.38	-0.89	432	5.59	12.21
9406	04.01.2001	25.78	0.029	-1.53	277	3.54	10.33
9407	-	11.03	0.13	3.31	308	2.36	8.74
9418	04.09.2001	20.83	-0.23	-0.99	270	2.91	9.43
9433	04.24.2001	16.71	0.063	-0.57	317	3.96	8.08
9450	05.12.2001	5.81	0.49	2.63	334	2.21	5.83
9450	05.14.2001	5.81	0.18	1.99	256	1.68	5.64
9454	-	13.00	-0.36	2.63	298	3.58	8.87
9463	05.23.2001	7.60	0.024	0.14	371	4.09	8.77
9691	11.14.2001	8.33	-0.76	10.33	437	4.80	27.55
9694	-	13.81	-1.05	1.09	328	4.17	14.58

Table 5.1: Summary of data for the analyzed active regions in the northern hemisphere.

AR number	Date (mm.dd.yyyy)	Latitude (degree)	$\langle\alpha_{v1}\rangle$ (10^{-3}ms^{-2})	$\langle\alpha_{v2}\rangle$ (10^{-3}ms^{-2})	$\lvert\langle\mathbf{B}\rangle\rvert$ (Gs)	$\langle\lvert\alpha_{v1}\rvert\rangle$ (10^{-3}ms^{-2})	$\langle\lvert\alpha_{v2}\rvert\rangle$ (10^{-3}ms^{-2})
8035	04.26.1997	34.50	0.0013	-1.02	132	0.42	3.36
8048	06.03.1997	28.29	0.21	-1.07	303	3.78	8.51
8070	08.11.1997	19.52	-0.18	-0.85	183	1.14	4.83
8118	12.12.1997	39.69	-1.02	-0.44	257	2.60	10.11
8120	-	22.31	-0.31	-1.03	197	0.74	6.00
8131	01.13.1998	22.48	-0.63	0.81	331	3.18	5.68
8143	01.29.1998	35.71	-0.034	-0.079	287	3.23	7.06
8156	02.16.1998	24.78	-0.19	1.34	410	4.00	11.08
8158	-	22.87	0.091	-2.73	242	1.39	16.50
8534	05.12.1999	24.19	0.10	-0.75	246	1.21	5.87
8540	-	17.29	-0.54	-0.65	316	2.57	4.63
8542	05.20.1999	21.07	-0.66	-0.47	331	2.61	7.96
8544	-	18.69	-0.45	-2.22	260	2.16	6.13
8583	06.16.1999	19.50	-0.26	-1.33	275	2.90	10.00
8906	03.13.2000	20.71	0.17	-1.56	310	2.30	6.53
8906	03.14.2000	20.71	-0.20	-0.17	317	3.15	7.11
8907	03.12.2000	16.83	-0.38	-2.61	410	5.39	22.08
8907	03.13.2000	16.83	-0.46	2.65	449	5.25	17.92
8907	03.14.2000	16.83	0.53	-8.89	449	8.92	36.96
8993	05.12.2000	23.10	-0.38	0.17	331	3.73	5.52
8996	05.20.2000	20.78	-0.081	0.75	318	4.39	8.50
8998	-	12.22	-0.16	-0.63	351	4.03	14.20
9056	06.27.2000	13.09	0.25	0.92	464	4.96	7.68
9067	07.07.2000	19.62	-0.31	-1.07	466	6.60	7.72
9068	-	17.48	0.22	0.22	298	2.56	13.77
9389	03.25.2001	12.78	-0.24	0.21	258	2.12	6.87
9395	03.29.2001	9.05	-0.079	1.32	306	3.33	10.99
9396	03.25.2001	5.81	-0.29	0.16	256	1.37	7.15
9397	03.29.2001	9.03	0.051	-3.05	308	3.20	14.39
9404	04.01.2001	5.62	0.16	-0.83	306	2.65	6.45
9408	-	9.19	0.95	0.14	487	6.51	7.97
9417	04.07.2001	8.62	0.85	1.01	368	4.04	10.89
9415	-	21.47	0.13	1.34	384	4.57	22.65
9415	04.09.2001	21.47	-0.14	4.35	392	3.47	14.85
9435	04.24.2001	20.05	-0.77	-0.77	341	3.79	6.69
9451	05.12.2001	20.67	0.063	1.48	289	1.74	9.41
9452	-	17.00	-0.065	2.05	352	2.91	5.32
9455	-	17.71	0.10	0.0081	313	2.74	5.74
9690	11.14.2001	17.17	0.43	-0.17	336	4.44	7.31
9787	01.24.2002	8.17	-0.72	-4.48	375	5.51	12.38
9787	-	8.17	0.42	0.11	370	5.80	9.72
9802	02.01.2002	13.26	0.89	2.09	409	5.84	9.19
9856	03.10.2002	3.93	-1.57	-1.34	462	6.30	10.11

Table 5.2: Summary of data for the analyzed active regions in the southern hemisphere.

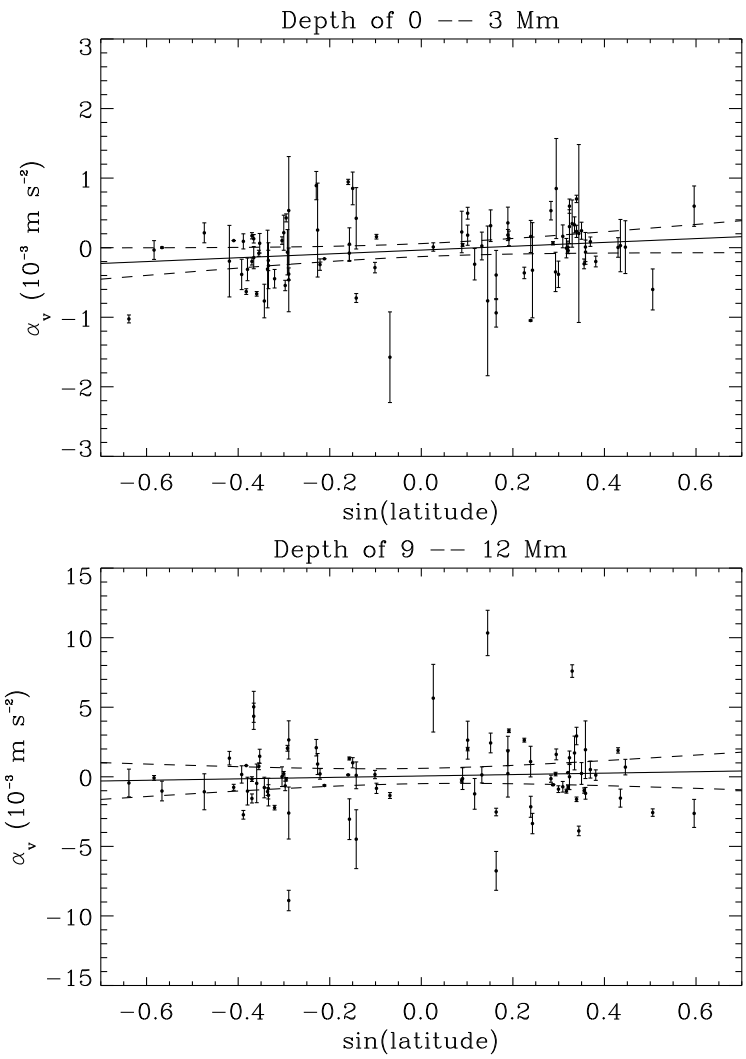

Figure 5.1: Latitudinal distribution of average kinetic helicity (α_v) from the selected active regions at two different depth intervals. The solid line in each panel is a linear fit to the scatter plot; the dashed lines indicate the 2σ error level of the fit (or 95% confidence level).

5.3 Statistical Results

5.3.1 Mean Kinetic Helicity vs Latitude

Figure 5.1 presents the latitudinal distribution of mean kinetic helicity for 88 sets of data at two different depth intervals 0 – 3 Mm and 9 – 12 Mm. It is found that

at the depth of 0 – 3 Mm, among 45 active regions in the northern hemisphere, 30 (66.7%) have positive mean kinetic helicity, and among 43 active regions in the southern hemisphere, 25 (58.1%) have negative signs of mean kinetic helicity. A linear fitting of the latitudinal distribution was performed by use of the least squares. The dashed curve in the graph shows 2σ errors (i.e., 95% confidence level) of the mean kinetic helicity distribution, from which we can find that the mean kinetic helicity of the active regions is preferentially negative in the southern hemisphere and positive in the northern hemisphere. The percentage of dominant signs in each hemisphere is similar to the percentage in the coronal loop study by Canfield & Pevtsov (1999).

At the depth of 9 – 12 Mm, it is found that 25 (55.6%) active regions in the northern hemisphere have $\alpha_v^z > 0$, and 24 (55.8%) active regions in the southern hemisphere have $\alpha_v^z < 0$. The statistical percentages from both hemispheres only show a very weak hemispheric preference of the signs of kinetic helicity, while the linear fit and the 95% confidence band do not show clear evidence of this tendency.

5.3.2 Kinetic Helicity vs Magnetic Strength

It is generally believed that the solar magnetic field is produced by the solar dynamo at the base of the convection zone, and the poloidal field is produced by the toroidal field through α-effect, where α is proportional to the kinetic helicity $\langle \mathbf{v} \cdot (\nabla \times \mathbf{v}) \rangle$ through the solar convection zone (e.g., Gilman & Charbonneau, 1999). Therefore, since we have estimated the kinetic helicity in the active regions, it is of great interest to find whether there is any relationship between the magnetic field strength and the kinetic helicity.

Here, we average the magnitude of the kinetic helicity as $\langle |\alpha_v| \rangle$ over the areas where the magnetic strength is larger than 100 Gauss. The mean magnetic field strength $\langle |\mathbf{B}| \rangle$ for each active region is obtained by averaging the line-of-sight magnetic field strength in the same areas where the mean magnitude of kinetic helicity is obtained. Note that these two quantities are both from the average of the magnitudes regardless of the signs of the quantities.

Figure 5.2 shows scatter plots of the mean magnitude of the kinetic helicity versus

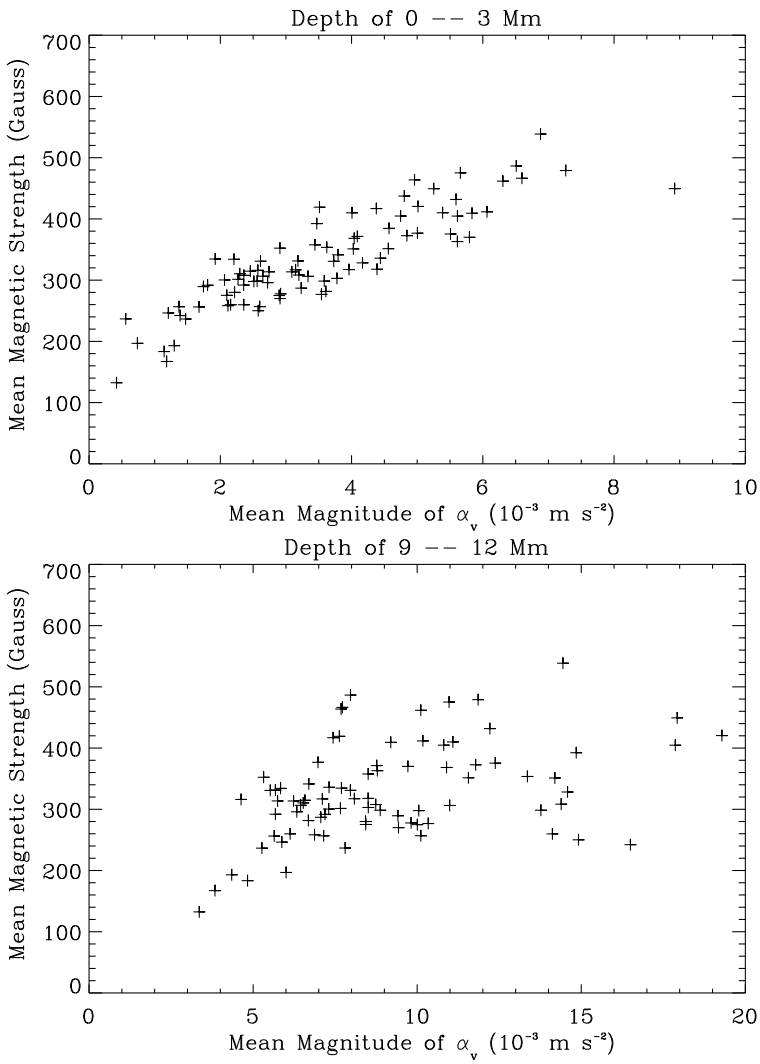

Figure 5.2: Scatter plot of the mean magnetic strength as a function of mean magnitude of kinetic helicity (α_v) from each selected active region.

the mean magnetic strength in all the 88 selected solar active region datasets. At the depth of 0 – 3 Mm, it shows that the mean magnetic strength seems linearly proportional to the mean magnitude of kinetic helicity, although the exact analytical relation is not clear. At the depth of 9 – 12 Mm, no obvious relation can be found between these two quantities, but it is basically true that the mean magnetic strength increases with the increase of the mean magnitude of kinetic helicity.

5.4 Discussion

Applying time-distance measurements and inversions on continuous Dopplergram observations has enabled us to detect the dynamics beneath the visible surface of active regions. The statistics of 88 active region datasets of Solar Cycle 23 show that at the depth of 0 – 3 Mm and 9 – 12 Mm, the distribution of mean kinetic helicity in active regions has a very slight hemispheric preponderance: negative in the southern hemisphere and positive in the northern hemisphere. Although the selection of 100 Gauss in the active regions as a computation criterion is arbitrary, the computations with 50 and 200 Gauss as criteria give us similar latitudinal distributions.

In Chapter 4, we have shown that the inversion technique applied to time-distance measurement could satisfactorily invert the vortical flows up to 12 Mm beneath the surface. But presumably the signals from time-distance measurements are becoming weaker with the increase of the depth, and how sensitive the time-distance measurements are to deep vortical flows is currently not known. So it is possible that some vortical flows may not be fully inverted and are underestimated. In addition, since we have little knowledge of the magnetic structures at the depth of 9 – 12 Mm, the selection of the computed region according to the photospheric magnetic field may be inaccurate. Particularly, at a few megameters beneath the surface, the velocity fields often extend to an area that is much larger than the surface structure (see figures in Chapter 3). Therefore, due to the above reasons, we may have underestimated the mean kinetic helicity at the depth of 9 – 12 Mm.

Overall, we find in our data that in the upper convection zone very close to the photosphere, kinetic helicity in active regions is slightly dominated by the positive sign in the northern hemisphere, and by the negative sign in the southern hemisphere. Therefore, the kinetic helicity preference has the opposite signs to the current helicity (or force-free coefficient α), which is negative (positive) in northern (southern) hemisphere. By simulating three-dimensional turbulent cyclonic magneto-convection, Brandenburg et al. (1990) found that in the upper layers of their magneto-convection model, the signs of kinetic helicity are opposite to the signs of the current helicity. In the more recent simulations of α-effect due to magnetic buoyancy as well as global

rotation, Brandenburg & Schmitt (1998) confirmed the finding of opposite signs between kinetic helicity and current helicity, and furthermore they showed that the kinetic helicity in the northern hemisphere is positive. Later analytical analysis on the compressible turbulent field (Rüdiger, Pipin, & Belvedère, 2001) confirmed the results from the numerical simulations. Our observations of positive kinetic helicity in the northern hemisphere give the same sign as expected from these theoretical works. On the other hand, we must be aware of the high fluctuation shown in our results. It is also noticed that in numerical simulation of Brandenburg & Schmitt (1998), the kinetic helicity is also highly noisy and a positive sign of kinetic helicity could only be found with some cautious analysis.

It was recognized by many authors (e.g., Seehafer, 1996; Choudhury, 2003) that the signs of magnetic helicity should be opposite in small scales (fluctuating field) and large scales (mean field), yet it is unknown whether the current helicity observed from photospheric vector magnetic field (e.g., Bao & Zhang, 1998) reflect the characteristic scale of small or large. We also do not know which scale our measurements of kinetic helicity represents, therefore, it is perhaps inappropriate to conclude that the kinetic helicity from our measurements has an opposite sign with the current (or magnetic) helicity observed by many previous authors. On the other hand, the conventional sign of kinetic helicity in the bulk of the convection zone in the northern hemisphere is negative (Moffatt, 1978), as observed by time-distance helioseismology study on the global scale (Duvall & Gizon, 2000). But Rüdiger, Pipin, & Belvedère (2001) argued the kinetic helicity should be positive for the compressible magnetized plasma where magnetic helicity plays an important role. The preponderance of the positive kinetic helicity in the northern hemisphere in our statistics may support this argument.

Another interesting result from our statistical study is that the mean magnetic strength in the active regions is roughly proportional to the mean magnitude of the z-component of kinetic helicity. It is generally believed that the solar poloidal magnetic field is produced by the α-effect, and numerical simulations (Brandenburg, Saar, & Turpin, 1998) have showed that $\langle \alpha_v \rangle$ could increase with the increase of $\langle \mathbf{B} \rangle$, although in some cases α-quenching would be present, viz $\langle \alpha_v \rangle$ decreases with the increase of $\langle \mathbf{B} \rangle$. The observation that $\langle \alpha_v \rangle$ is proportional to $\langle \mathbf{B} \rangle$ may show us that the

mean magnetic field in the solar active regions is much smaller than the equipartition magnetic strength, thus too weak to provoke the α-quenching effect. In addition, the average of the magnetic fields may have smeared out the α-quenching effect in some strong magnetic strength areas. Once again, we understand that the α-effect may mainly work in the bulk and bottom of the convection zone rather than near the solar surface, therefore more studies of the dynamics in the whole convection zone are required to better understand the formation of magnetic fields in active regions. Nonetheless, the present study in the active regions in the upper convection zone should provide some valuable observational evidence to understand the α-effect of solar dynamo theory.

Chapter 6

Deep Structure of Supergranular Flows[1]

6.1 Previous Observations

Granulation, observed at the solar photosphere, with a typical size of 1 Mm and lifetime of 10 minutes, is believed to be a solar convective structure. Supergranulation was first observed in 1950s (Hart, 1954), and was later also associated as convective cells (Leighton, Noyes, & Simon, 1962), although this interpretation is still at dispute.

Supergranulation is characterized by its horizontal divergent flows, observed either by direct Doppler velocities when the supergranulation is away from the disk center (e.g., Hart, 1954; Leighton, Noyes, & Simon, 1962), or by tracking the advection of magnetic elements or granules (e.g., Simon, 1967; November & Simon, 1988). Its typical scale is 32 Mm and typical lifetime is 20 hours, and the horizontal outflows have a speed of the order of 500 m/s. The supergranular flow pattern appears cellular, diverging from center outward and terminating at boundaries outlined by strong photospheric magnetic fields that are corresponding to chromospheric magnetic networks. Measurements of downflows at supergranular boundaries are often complicated by the presence of magnetic elements, and this makes the Doppler velocity very difficult to

[1]Part of this chapter was published in *Proceeding of SOHO 12/GONG+ 2002 Workshop* (Zhao & Kosovichev, 2003a)

disentangle from effect of the magnetic field by use of spectrum. Nevertheless, downward flows with speed of tens to hundreds of meters per second were reported (e.g., Frazier, 1970; Wang, 1989), and the downward flows often concentrated in the small regions where magnetic field appeared. If the downward flows at the supergranular boundaries are still detectable, the vertical velocity at the supergranular centers are hardly measurable. No reliable measurements have so far been reported from spectral analyses.

The other interesting and well-known characteristic of supergranules is its super-rotation rate. By tracking the supergranular pattern at the solar surface, it was found that supergranules rotate much faster than the solar plasma, and also faster than the surface magnetic features (Duvall, 1980; Snodgrass & Ulrich, 1990). This remained a puzzle for two decades. Recently, Gizon, Duvall, & Schou (2003) and Schou (2003) found the wave-like features of supergranulation which may help to explain the super-rotation rate. The rotational speed of supergranular patterns may be an addition of the real rotational speed of supergranulation and the wave propagation speed. The real rotation speed of supergranules derived by subtracting the wave propagation speed from the supergranular patterns speed is similar to the speed of magnetic features, and this was then interpreted by the authors as that supergranules may have a common origin with solar surface magnetic features.

In this chapter, we will attempt to obtain the subsurface flow fields by doing inversions on time-distance measurements of supergranules. And we also try to determine the depth of supergranules by correlating the divergent flows with the return flows at some depths.

6.2 "Cross-talk" Effects in Inversion

Strong "cross-talk" effects will affect our inversions for time-distance measurements of supergranular flows. This is because, at the center the supergranules, strong horizontal divergence can accelerate the outgoing waves and decelerate the ingoing waves in the same way as the downward flows do; while at the boundary of supergranules,

strong horizontal convergence can accelerate the ingoing waves and decelerate outgoing waves in the same way as the upward flows do. On the other hand, the vertical flow speed of plasma at the center of supergranules is often one order smaller than the horizontal velocity. So, in some cases, the horizontal divergence may be inverted as downward flows, which we should avoid.

Therefore, many artificial experiments were designed to test the ability of our inversion code to solve the "cross-talk" effects. Figure 6.1 shows a very interesting example which reminds us to be very cautious in doing inversions. The upper panel of Figure 6.1 shows an artificial model of flows having a strong horizontal divergence but very weak vertical flow speed, which may perhaps simulate the flow structures of supergranules. The lower two panels of Figure 6.1 show the inversion results by LSQR algorithm with 5 and 100 iteration steps. Interestingly, but not surprisingly, results with 5 iteration steps gave downward flows at the center of the divergent regions, which is not the case in the original data. However, it seems that the results with 100 iteration steps can recover perfectly the shallow flow fields. This numerical experiment shows us that "cross-talk" can result in incorrect vertical velocity in inversions for a small number of iteration steps.

As a summary after various artificial models experiments, it was found that for different flow structures, "cross-talk" effects can be significant or not. However, after a sufficiently large number of iterations, the vertical flows can still be nearly or totally recovered for noise-free data. But, for the case of real data, since noises are unavoidable, it is usually impractical to have a large number of iterations because noises can be easily magnified and transported to other locations. The optimal number of iterations selected in practice is larger than 5, but less than 20.

6.3 Inversion for Supergranules

6.3.1 Supergranular Flows

A set of 512-minute high-resolution MDI data was used for time-distance analysis to derive the flow fields of supergranules. Measurements and inversions were performed

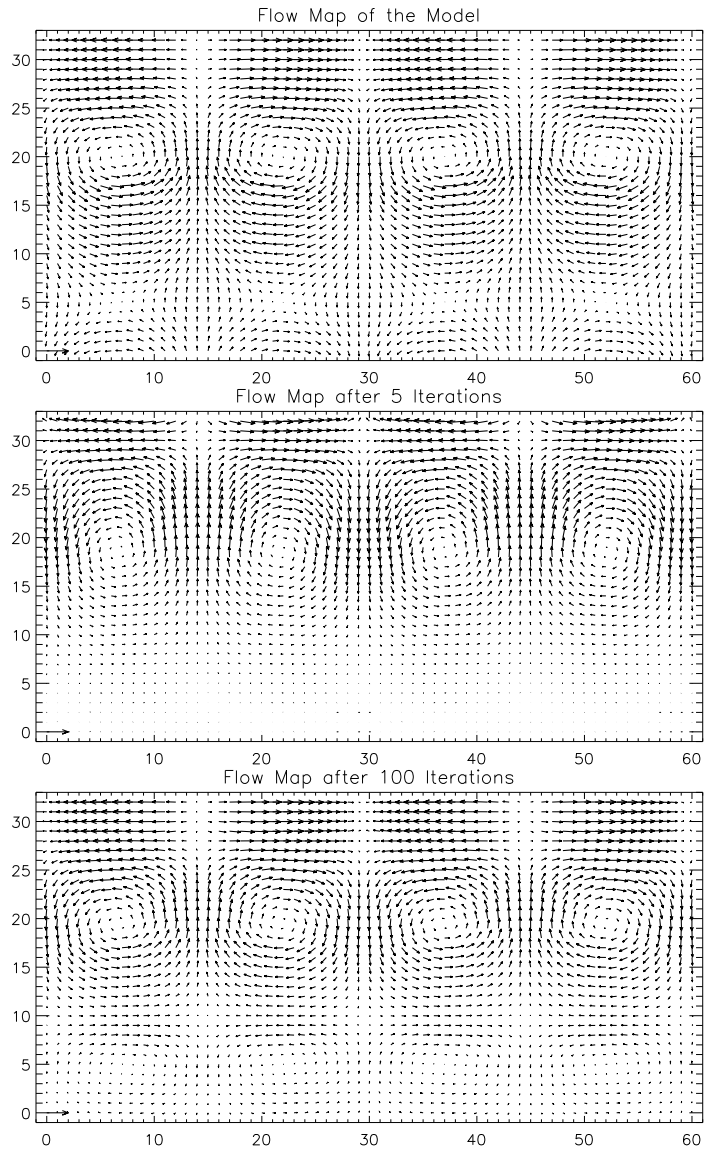

Figure 6.1: An example of inversion tests over artificial models. The upper panel shows an artificial flow field in a vertical cut. The two lower panels show the inversion results of noise-free travel times after 5 and 100 iterations.

as described in Chapter 2. Due to the perhaps confused vertical flow directions as demonstrated in the last section, we only present the horizontal flow fields in the following.

Figure 6.2 shows one large supergranule with very strong divergence picked from

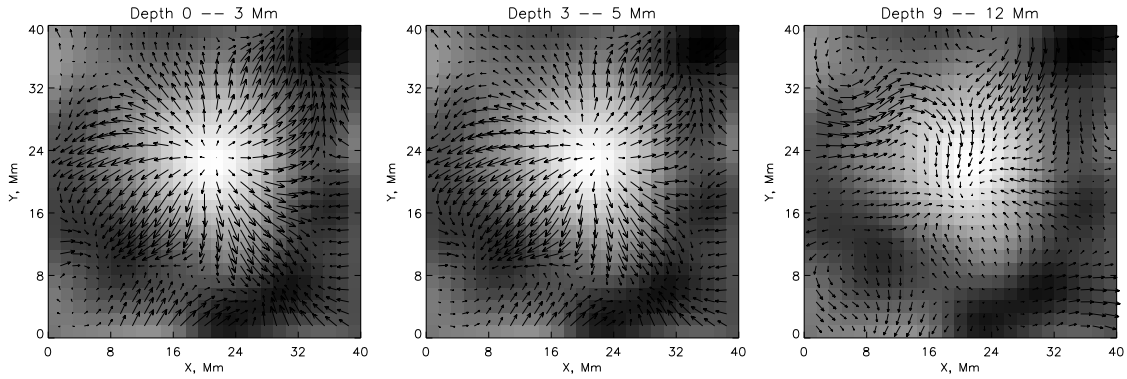

Figure 6.2: Horizontal flows of a supergranule from inversion results of the MDI data. The background image of each graph is the divergence of flows near the solar surface to indicate the location of the supergranule, with white as divergence and dark as convergence. The longest arrow in each panel represents approximately 500 m/s.

the studied region, with the center of the supergranule at approximately latitude 6° in North hemisphere and when it is passing the central meridian. The horizontal flow maps at three different depth intervals are presented. Outflows from the central supergranular region can be seen at the depths from the surface to about 5 Mm. However, at the depth of 9 – 12 Mm, convergent flows are found with smaller speed, though not toward exactly the center of the supergranule observed at the surface.

It should also be pointed out that the return convergent flows are not seen for all the supergranules. Except some large supergranules with strong divergence, most other supergranules do not show returning flows in deeper layers. Random flows, which may be caused by noise propagation or systematic errors, dominate the flow structures below the depth of 6 Mm or so for such supergranules.

6.3.2 Depth of Supergranules

Although the vertical flows have not been reliably derived from our inversions, the convergent flows found at depth of ∼10 Mm may suggest that the supergranules are cellular convective structures. If this is true, we may estimate the depth of supergranules by the following means. In a quiet solar region of approximately 200 Mm × 200 Mm, which includes about 30 supergranules, we calculate the divergence

$\nabla \cdot \mathbf{v}_h = \partial v_x/\partial x + \partial v_y/\partial x$ from the inverted horizontal velocities at different depth intervals. Then we compute the correlation coefficients of the divergence map at each depth with the divergence map of the first layer.

Figure 6.3 shows the results of correlation coefficients as a function of depth. The coefficient drops from 1.0 to 0.0 with the increase of depth, and continues to drop to the negative until -0.5. This may indicate that the divergent flow structures may extend from the surface to around 6 Mm, and then are replaced by the returning convergent flows, which extends to a depth of around 14 Mm. From this plot of correlation coefficients, we may estimate that the depth of supergranules are approximately 14 Mm.

Previously, Duvall (1998) estimated the depth of supergranules to be around 8 Mm by calculating the correlation coefficients between horizontal components of velocities

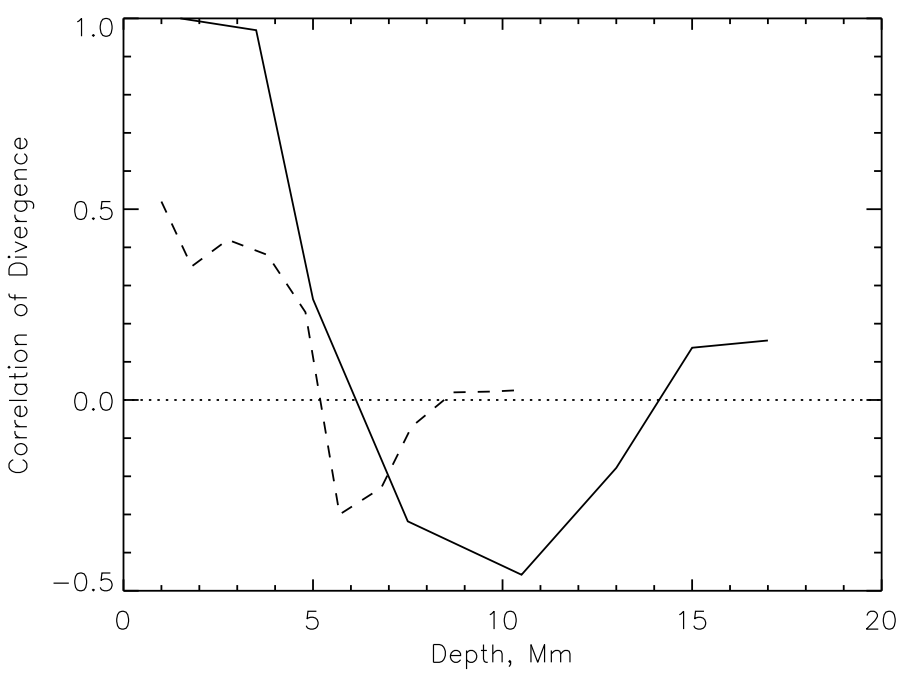

Figure 6.3: Correlation coefficients (*solid curve*) between the divergence maps at each different depth and the divergence map of the top layer (from this study). The dashed curve shows the correlation between horizontal velocities at different depths with the top layer (from Duvall, 1998). The dotted line indicates the 0 line.

at different depths and the velocities at the surface (also shown in Figure 6.3). But that work (Duvall, 1998) did not exclude the f-modes when doing time-distance measurements, which probably cause the shallowness of the depth result. The result presented here has significantly extended the estimated depth of supergranules, which may be closer to what some researchers expected (Hathaway et al., 2000).

6.4 Discussion and Summary

Various artificial data experiments have shown us how the inversion codes can provide us inaccurate and even opposite results. This cautions us the necessity of designing various artificial experiments before doing inversions on real observations, and suggests care when interpreting inversion results.

Due to the nature of the weak vertical supergranular flow speed, we failed to derive reliable vertical flows like previous studies based on analyzing spectral lines. The issue is that the number of inversion iterations is limited by noise propagation and magnification. However, if we have more knowledge of time-distance measurement errors and are able to incorporate the error covariance matrix into the inversion code, we may increase the number of inversion iterations and prevent the fast propagation and magnification of measurement errors. On the other hand, some constraints may also be provided to the inversion code in order to have reliable results with relatively small number of iterations. Such constraints may include the conservation of mass and the minimization of kinetic energy. However, we have not found an effective way to incorporate such constraints into the LSQR inversion code.

In this study, we have found return converging flows of supergranules at a depth of approximately 10 Mm. This may indicate the flow structures of supergranules are cellular, like most researchers expected. Base on this assumption, we estimated the depth of supergranules to be around 14 Mm, which is similar to the depth as some researchers expected. Braun & Lindsey (2003) computed the ratio of velocities at different depths that were derived from acoustic holography technique, and found a similar curve as shown in Figure 6.3, from which they suggested supergranules have a convective structure.

The computations presented in this chapter can be extended to a few Carrington rotations which were taken during the MDI Dynamic Campaign periods. By such computations, solar rotational speed and meridional flows can be inferred; and latitudinal vorticity distribution can also be derived. These results will be presented and discussed in the next chapter.

Chapter 7

Global Dynamics Derived from Synoptic Flow Maps [1]

7.1 Introduction

The Sun's global-scale flows, such as solar differential rotation and meridional circulation, are crucial for understanding solar magnetic cycles and dynamo mechanisms. Large-scale flows, as shown in Gizon, Duvall, & Larsen (2001) and Haber et al. (2002), present information on the dynamics and evolution of active regions. The flow structures of both scales can deepen our understanding of the generation of solar magnetism, and of the birth and evolution of solar active regions.

Solar rotation rates have been widely studied by use of direct Doppler velocity measurements (e.g., Howard & LaBonte, 1980), by tracking photospheric magnetic or supergranular features (e.g., Meunier, 1999), and by both global and local helioseismology (e.g., Thompson et al., 1996; Giles, 1999). The solar cycle variations of solar rotation known as torsional oscillation were first observed by Howard & LaBonte (1980), and then studied by many researchers using different approaches (e.g., Snodgrass, 1985; Howe et al., 2000a; Ulrich, 2001). Torsional oscillation is a phenomenon of mixed faster and slower rotational bands relative to a smooth rotation profile in each hemisphere, with the faster rotational bands residing on the equatorial side of

[1] Most part of this chapter was published in the Astrophysical Journal (Zhao & Kosovichev, 2004)

the solar activity belts. Torsional oscillation is not only found in the photosphere, but has also been detected beneath the solar surface by helioseismology. Analysis of f-mode frequency splitting (Kosovichev & Schou, 1997; Schou, 1999) detected the existence of torsional oscillation extending to a depth of approximately 10 Mm. More recently, it was found that this phenomenon extended to the depth of $0.92R_\odot$ (Howe et al., 2000a), and later found that it might extend down to the tachocline through the entire convective zone (Vorontsov et al., 2002).

The solar meridional circulation is more difficult to observe than the rotational flows, because of its much smaller velocity. Despite difficulties and uncertainties of earlier years, a poleward meridional flow of the order of 20 m/s was eventually found by analysis of Doppler velocity (Duvall, 1979; Hathaway et al., 1996), time-distance helioseismology (Giles et al., 1997) and the ring-diagram analysis (Basu, Antia, & Tripathy, 1999; Haber et al., 2002). More recent studies showed that the meridional flows also vary with the solar cycle. Measurements of acoustic travel times (Chou & Dai, 2001; Beck, Gizon, & Duvall, 2002) implied that, after subtracting a smooth poleward meridional flow profile, the residual meridional flow showed divergent flow patterns around the solar activity belts below a depth of 18 Mm or so. This divergent flow pattern migrates toward the solar equator together with the activity belts. Evidence of meridional flow variations associated with the solar cycle has also been found by the ring-diagram helioseismology (Haber et al., 2002; Basu & Antia, 2003).

The torsional oscillation and meridional flows in the solar interior obtained from helioseismological studies can help us understand turbulence in the solar convection zone. Some numerical simulations (Brun & Toomre, 2002; DeRosa, Gilman, & Toomre, 2002) of the multi-scale turbulent convection inside the solar convection zone, aimed at determining how the differential rotation, torsional oscillations and meridional flows are sustained, and how these global features are related to the turbulence of different spatial scales. It was found that the Reynolds stress might play an important role in sustaining the global-scale flows and transporting the angular momentum in the meridional plane. On the other hand, the differential rotational and meridional flows also provide observational input for numerical models of the

solar dynamo (Dikpati & Charbonneau, 1999). It is generally believed that the solar dynamo operates in the tachocline at the base of the convection zone, where the strongest radial rotational shear is located. The poloidal magnetic field of the Sun may be regenerated from the toroidal field by helical turbulence by means of the so-called α-effect (e.g., Stix, 2002). Thus, studies of rotational and meridional flows and their variations associated with the solar cycle are important in understanding the solar dynamo and turbulence in the convection zone.

Time-distance helioseismology measurements and inversions provide a tool to study three-dimensional flow fields in the upper solar convection zone with relatively high spatial resolution. By applying this technique to *SOHO*/MDI Dynamics campaign data (Scherrer et al., 1995), one can map the solar subsurface flows with significantly higher resolution than is obtained from the ring-diagram analysis (e.g., Haber et al., 2002). By averaging such flow maps, both zonal and meridional flows can be derived to compare with results of global helioseismology, direct Doppler measurements and ring-diagram helioseismology. Moreover, a better spatial resolution of time-distance helioseismology enables us to calculate maps of vorticity, from which a latitudinal distribution of vorticity can be inferred. This is important in understanding the α-effect of the solar dynamo theory. Similar studies to derive flow structures just beneath the photosphere have been carried out by f-mode time-distance helioseismology (Gizon, 2003).

In §7.2, we introduce the data reduction and analysis. In §7.3, we present the results for the torsional oscillation, meridional flows, and vorticity distributions with latitude, and show variations of these properties with the solar cycle. In §7.4, we show the residual synoptic flow maps for two solar rotations and discuss the large-scale flow patterns of active regions. Discussions and conclusions follow in §7.5.

7.2 Data Reduction

In every year following the launch of the *SOHO* mission in 1995, the *SOHO*/MDI (Scherrer et al., 1995) has spent about two months in continuous (with only occasional interruptions) full-disk Dynamics Campaigns, observing Dopplergrams with

1-min cadence and 2 arcsec/pixel spatial resolution, thus providing unique data for helioseismological studies. The total number of these campaigns is 7 so far, covering the period from 1996 to 2002, from solar minimum to solar maximum of Solar Cycle 23. The 2003 run was interrupted by too many telemetry gaps to be used for such studies. One useful way to study the large-scale flow structures is to construct synoptic maps of the inferred flows in a way similar to that in which Carrington synoptic magnetic maps are constructed.

In order to make a synoptic flow map for one Carrington rotation, we select a central meridian region 30 heliographic degrees wide in longitude, from $-54°$ to $54°$ in latitude, with continuous 512-minute observation of acoustic oscillations. After remapping the Doppler images by utilizing Postel's projection, and removing the Carrington rotation rate, time-distance measurements are carried out following the descriptions in Giles (1999). Then, data inversions are performed to obtain the horizontal velocities following the procedure described in Chapter 2. This provides one tile for the synoptic flow map. For the next tile, the central meridian region observed 8 hours after the previous region is selected, remapped and processed in the same way. This procedure is repeated until the end of a solar rotation period. In practice, for each solar rotation, approximately 90 tiles of such central meridian regions of size $30° \times 108°$ are obtained, each from continuous 512-minute intervals. The tiles overlap both spatially and temporally. Based on the Carrington coordinate system, these tiles are merged together to form a synoptic flow map, with each specific longitude being overlapped 6 times. The spatial resolution of the resultant flow map is half that of the original MDI full-disk observation, i.e., 0.24 heliographic degrees per pixel. One Carrington rotation is selected for study each year from 1996 through 2002.

The time-distance helioseismology inversions carried out in this study are based on the ray-path approximation. Although an acoustic wave theory for time-distance helioseismology is under development (Birch & Kosovichev, 2000; Gizon & Birch, 2002), it was argued that ray approximation could give credible inversion results with fewer computations (Birch et al., 2001; Jensen et al., 2001). Because of a cross-talk effect between the horizontal divergence and the vertical flows in time-distance measurement (Kosovichev et al., 1997), the weak vertical flows in the quiet solar regions

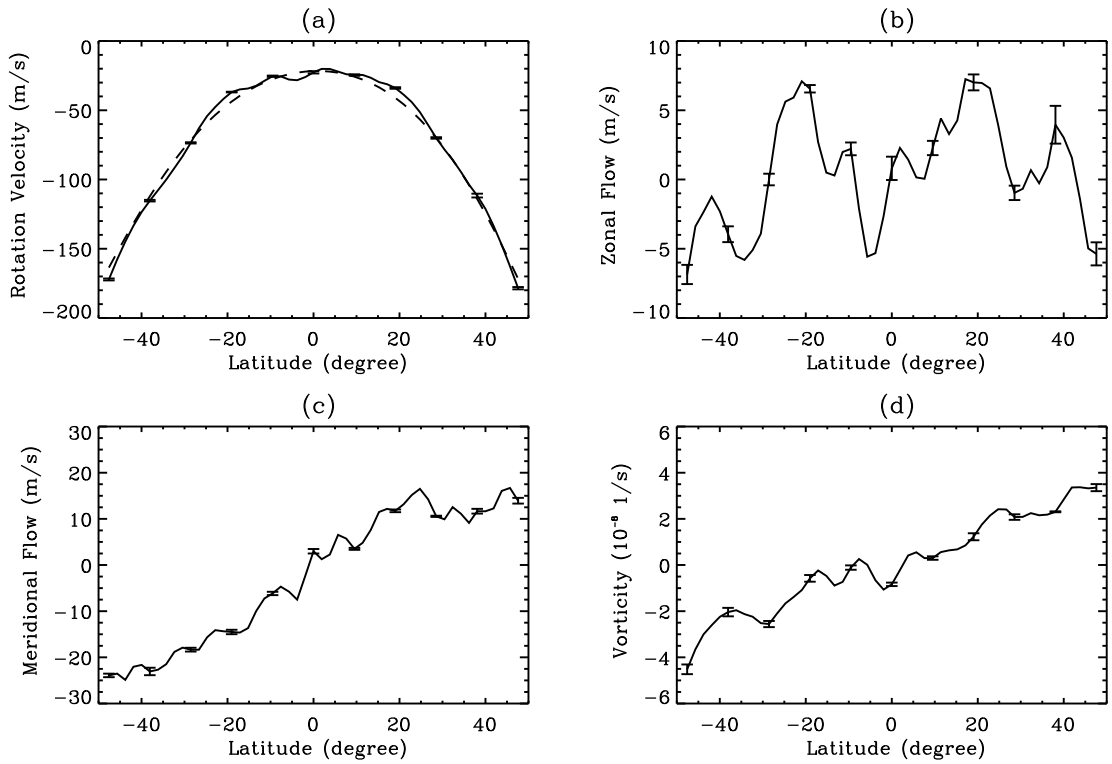

Figure 7.1: (a) Rotation, (b) torsional oscillation (zonal flow), (c) meridional flows and (d) vorticity distribution derived from CR1923 of year 1997 at the depth of $3-4.5$ Mm. In (a), the solid curve is the rotational velocity displayed after the Carrington rotation rate is subtracted; the dashed line is a fit to the mean rotational velocity (see text). The error bars show the standard deviation of the data from which the rotational velocity is derived. For clarity, only a small number of selected error bars are displayed. In (b), the curve is obtained by subtracting the dashed curve from the solid curve in (a); the error bars may be underestimated, because the error of fitting is not taken into account. In (c) and (d), error bars are obtained and displayed in the same way as in (a). Error bars in Figures 7.2 - 7.4 are obtained and displayed in the same way as here.

derived from our inversions are considered less reliable than the stronger vertical velocity in active regions (Zhao & Kosovichev, 2003b). Therefore, only horizontal velocities are analyzed in this study.

Once the synoptic maps of horizontal velocities at different depths are obtained,

the solar rotational and meridional velocities can be derived by averaging the East-West and North-South components of velocities in the synoptic map over longitude for different latitudes. In order to remove fluctuations caused by supergranules, the rotational and meridional velocities are averaged again on a scale of 30 Mm in the latitudinal direction. The vertical component of the vorticity $\omega_z = \partial v_y/\partial x - \partial v_x/\partial y$ (v_x and v_y represent East-West and North-South velocities respectively) is derived at each grid point of the synoptic flow map by employing a standard five-point derivative formula. This provides a synoptic map of the vertical component of vorticity. By applying the same averaging procedure as that used for the rotational and meridional flows, we obtain the vorticity distribution as a function of latitude for different depths. Figure 7.1 shows an example of our inference of rotational velocity, torsional oscillation, meridional flow, and vorticity distribution at a depth of 3 – 4.5 Mm for Carrington Rotation CR1923 in 1997.

7.3 Variations of Torsional Oscillation, Meridional Flow and Vorticity with Solar Cycle

7.3.1 Torsional Oscillation

There are generally two different approaches used to derive torsional oscillations from the inferred rotation rate, one is to subtract a temporal average of measured rotation rates from the whole period of observations from the rotation rate of each observing interval (e.g., Howe et al., 2000a), the other approach is to fit the average rotation rate by a function of $\Omega(\theta) = a_0 + a_1 \sin^2\theta + a_2 \sin^4\theta$, where θ is the solar latitude, then subtract the fitted curve from the individual rotation rate (e.g., Hathaway et al., 1996). There are some differences in the results of these two approaches, as pointed out by Antia & Basu (2000). Because we do not have continuous observations, the second approach is adopted in this study: all seven rotation velocity profiles are averaged to obtain a smoother profile, which is then fitted by the function given above. From our computation, after the subtraction of the standard Carrington rotation rate, the parameters of the fitted function for the rotational velocity are

$a_0 = -21.6$ m/s, $a_1 = -177.6$ m/s and $a_2 = -167.6$ m/s for the depth of 3 – 4.5 Mm, and $a_0 = -6.1$m/s, $a_1 = -233.0$ m/s and $a_2 = -17.8$ m/s for the depth of 6 – 9 Mm. The dashed curve in Figure 7.1a shows the fitted function obtained for the depth interval of 3 – 4.5 Mm. The zonal flows for each rotation is then obtained by subtracting the fitted curve from the rotational velocity profile of the corresponding depth.

The zonal flows, as functions of latitude for two different depth intervals, 3 – 4.5 Mm and 6 – 9 Mm, are shown in Figure 7.2, with the shaded regions indicating locations of the activity belts in both hemispheres. The location of the activity belts is derived from the latitudinal dependence of the mean absolute magnetic field strength obtained for the corresponding Carrington rotation time period by use of MDI magnetograms.

It is important to note that the results of our time-distance helioseismology inversions are consistent with the previous investigations based on different spectroscopic and helioseismic techniques. In particular, in both hemispheres the bands of faster rotation can be found with the activity belts residing on the poleward side of the faster rotation zones. These bands of faster rotation migrate equatorward together with the activity belts as the solar cycle progresses. In addition, the velocity of zonal flows obtained in our time-distance inversions is similar to that obtained by inversion of normal mode frequency splittings (Kosovichev & Schou, 1997; Howe et al., 2000a), and also by the ring-diagram analyses (Basu, Antia, & Tripathy, 1999; Haber et al., 2002). For 1997 – 2002, when solar activity was significant, the faster bands of zonal flows of the order of 5 m/s are prominent, while in 1996 when the Sun was less active, the faster bands are not so obvious, and the maximum velocity variation is also smaller. As one can see, the zonal flows are not symmetric relative to the solar equator.

7.3.2 Meridional Flow

The meridional flows derived for different Carrington rotations are displayed in Figure 7.3a as a function of latitude for two different depth intervals. Generally, the

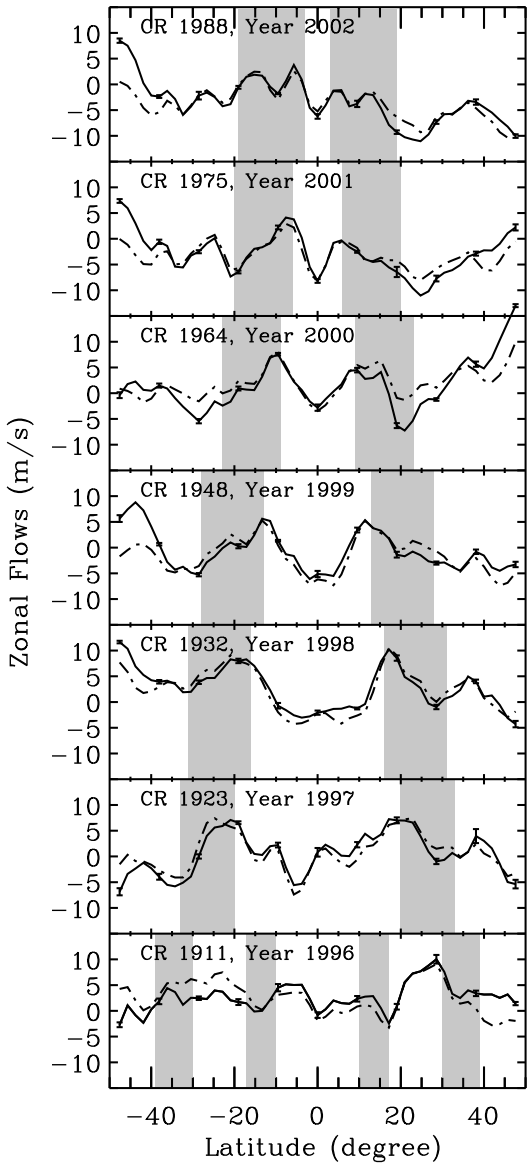

Figure 7.2: Zonal flows obtained at the depths of 3 – 4.5 Mm (*solid curves*) and 6 – 9 Mm (*dash dot curves*) for different Carrington rotations. Note that different rotation profiles have been removed at the two different depth intervals (see text). The shaded regions represent the locations of activity belts. The error bars for the depth of 6 – 9 Mm are not shown but are similarly scaled.

meridional flows are directed poleward with a speed of about 20 m/s, but have some variations in different phases of the solar cycle.

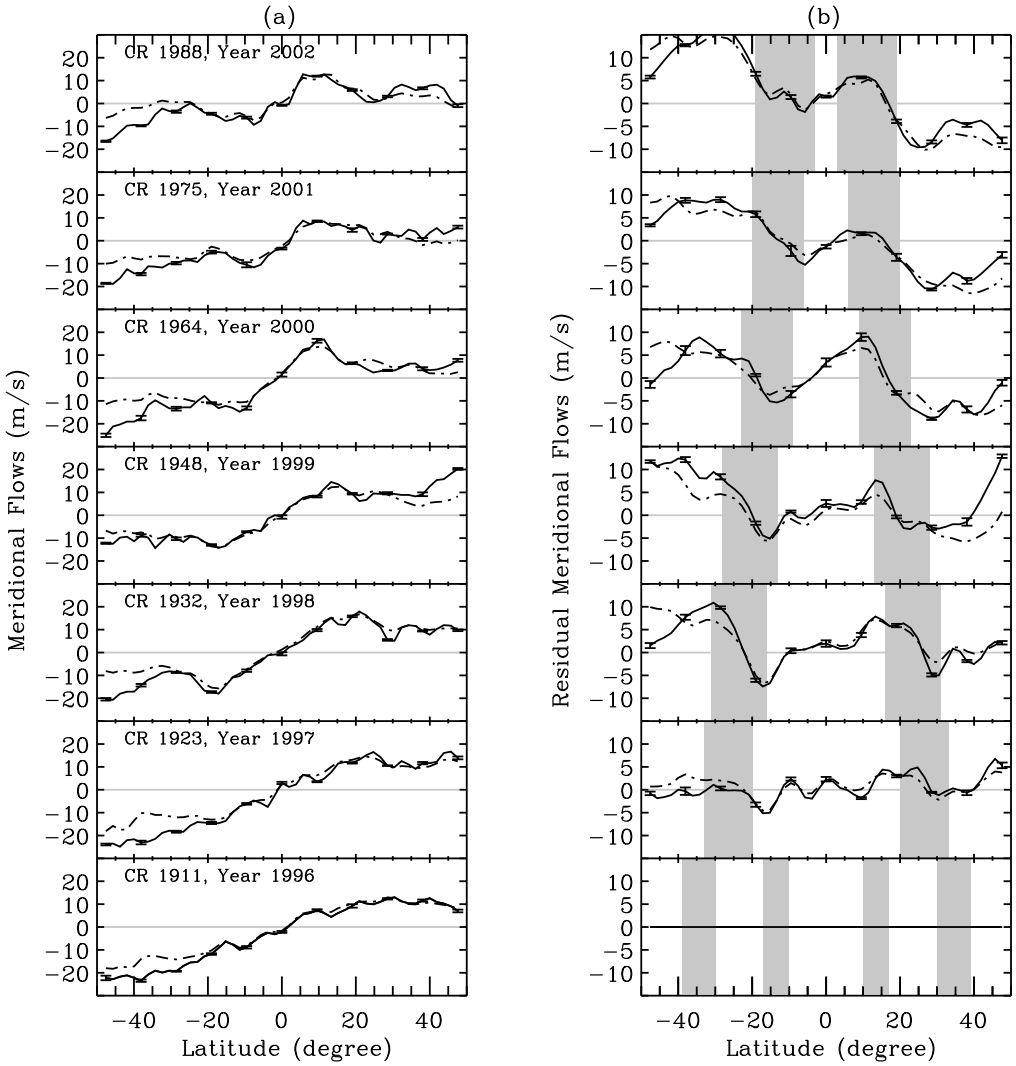

Figure 7.3: (a) Meridional flows obtained from 3 - 4.5 Mm (*solid curves*) and 6 - 9 Mm (*dash dot curves*) for different Carrington rotations. (b) The residual meridional flows after the flows of CR1911 have been subtracted from each rotation. Shaded regions are same as Figure 7.2. The error bars may be underestimated, because the errors from flows of CR1911 are not included.

It has been pointed out that the MDI camera may not be perfectly aligned parallel to the Sun's rotational axis as determined by the Carrington elements (Giles, 1999). A small deviation may cause a leakage of rotational velocity to the meridional direction, thus causing offset to the measurements of meridional flows. It has also been pointed

out that the Sun's true rotational axis may differ from that given by the Carrington elements (Giles, 1999). Based on statistics of time-distance measurements, Giles (1999) proposed an empirical formula to make P-angle corrections to the meridional flows (for details, please refer to `http://soi.stanford.edu/papers/dissertations/giles`), which was later used by Schou (2003). Such corrections are employed in this study to adjust the meridional flows derived from our time-distance analysis. We acknowledge that the meridional velocity corrections calculated from the empirical formula may have some uncertainties. Meridional flows shown in Figure 7.3a are after the P-angle corrections.

In order to study variations of the solar meridional flows with the increase of solar activities, we adopt the meridional flows of CR1911 of 1996, obtained during a solar minimum year, as a reference to investigate the changes of meridional flows in the following years, as suggested by Chou & Dai (2001). Thus, we subtract the meridional flow of CR1911 from all the meridional flows of the following years, and display the residual flows in Figure 7.3b.

From Figure 7.3b, we find that residual meridional flows converge toward the activity belts in both hemispheres, and the magnitude of these flows ranges from ~ 2 m/s to ~ 8 m/s. During the studied period, the convergent residual flows migrate toward the equator together with the solar activity belts except in the Northern hemisphere during CR1988 in 2002. The residual flows near the solar surface reveal extra converging components in addition to the poleward meridional flow profile of the solar minimum. The residual flows shown here agree with f-modes analysis near the photosphere (Gizon, 2003), and are in general agreement with findings from the ring-diagram analyses (Haber et al., 2002; Basu & Antia, 2003) that the gradient of the near-equator meridional flows steepen with the development of the solar cycle toward the solar maximum. However, divergent meridional flows from activity belts are found in much deeper solar layers in other time-distance studies (Chou & Dai, 2001; Beck, Gizon, & Duvall, 2002).

It is recognized that the MDI camera was set out of focus in 1996, and also that some focus changes occurred during the period of 1997 to 1999. The focus changes may bring systematic errors into our computations of synoptic flow maps. In order

to estimate the error level introduced by the focus changes, we select quiet regions near the solar disk center in the years of 1996 and 1999. Assuming supergranulation in quiet regions remains unchanged in these years, the changes in the magnitude of supergranular divergence may reflect the variations of the velocity measurements caused by the camera focus changes. Our computations show that the changes of the mean magnitude of flow divergence are only 3.6% at the depth of 3 – 4.5 Mm and 0.6% at the depth of 6 – 9 Mm, which are of smaller scales than the error bars in Figure 7.3. On the other hand, the mean acoustic travel time for the shortest time-distance annulus used in our computation shows a change of approximately 4.0% in these two years near the equator, which indicates that the largest possible errors due to the focus changes in the inverted velocity may be approximately 4.0% near the solar surface. The error estimations from the above two different approaches are basically in agreement. Therefore, the selection of the meridional flow of 1996 as a reference does not introduce significant errors in our inferences of the residual meridional flows.

7.3.3 Vorticity Distribution

Figure 7.4a shows the vorticity distribution at two depths for different Carrington rotations. The vorticity distribution seems largely to be a linear function of latitude, with some fluctuations for all years. This indicates that the global-scale vorticity mainly results from the differential rotation, in which the derivative of the term $\sin^2\theta$ has the largest contribution. We then compute the vorticity contributed from the fitted rotational velocities obtained from Section 3.1, and subtract the vorticity function from the vorticity distribution of each rotation to study the deviation of the vorticity distribution from that caused by the mean differential rotation.

The latitudinal distributions of the residual vorticity obtained after subtracting the derivative of mean differential rotation are presented in Figure 7.4b. It is found that in the Northern hemisphere, the residual vorticity usually displays a peak within the activity belt, and two valleys on both sides of the peak. However, in the Southern hemisphere, the residual vorticity usually displays a valley within the activity belt except in CR1988. The peaks and valleys of the residual vorticity in the activity belts

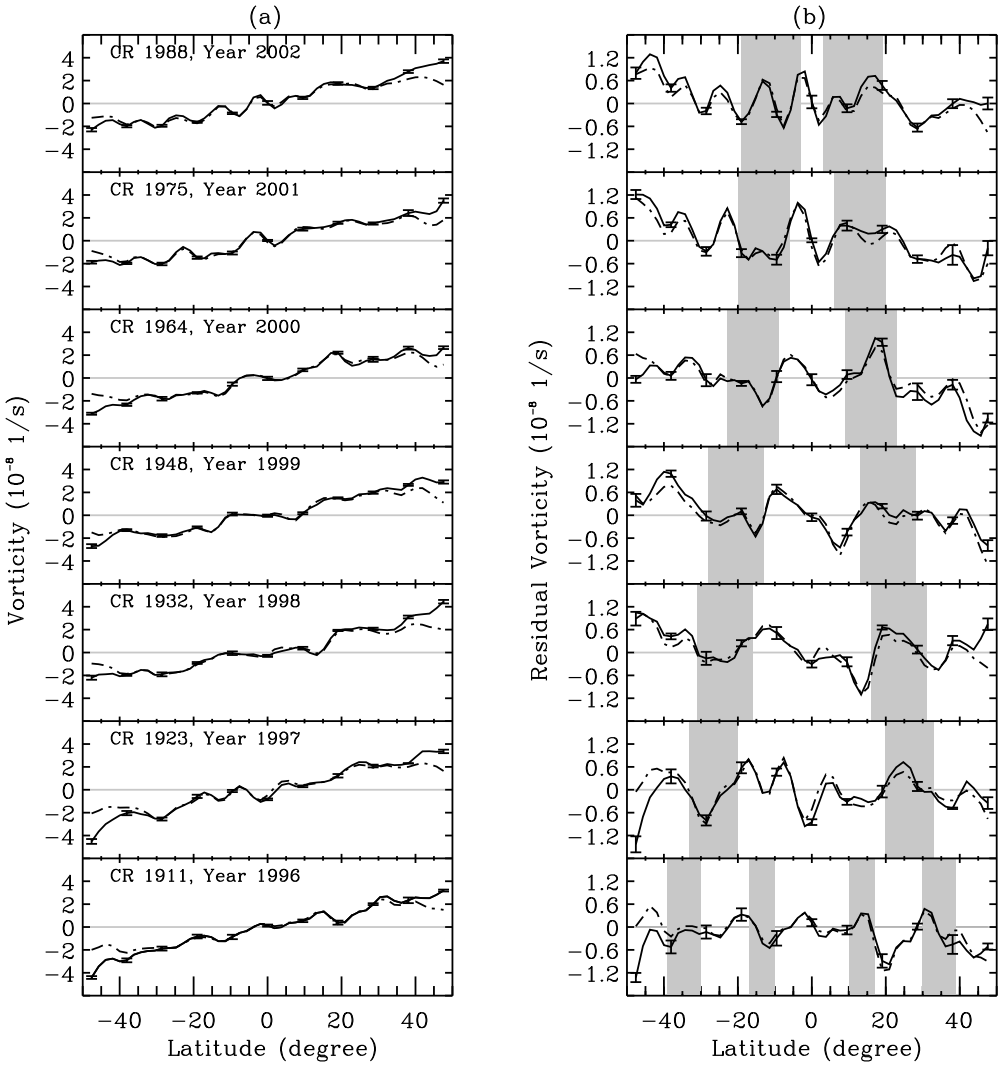

Figure 7.4: (a) Same as Figure 7.3a but for vorticity; (b) The residual vorticity after the vorticity caused by the mean differential rotation is subtracted from the vorticity distribution of each Carrington Rotation. The shaded regions represent the locations of solar activity belts. The error bars may be underestimated because the errors from the derivative of the mean differential rotation are not included.

migrate together with the solar activity belts as the solar cycle progresses.

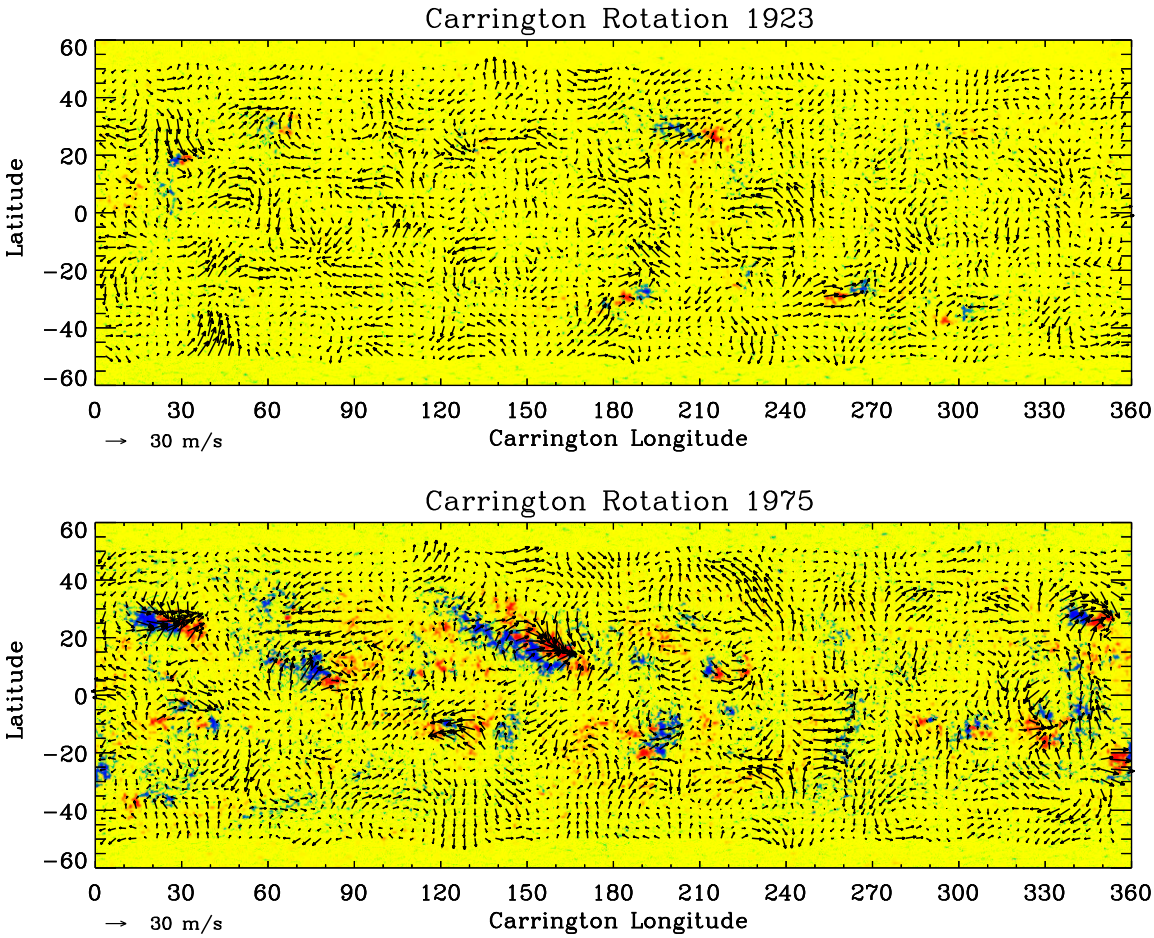

Figure 7.5: Synoptic maps for the residual flows at the depth of $0 - 3$ Mm for CR1923 (*above*) and CR1975 (*lower*).

7.4 Residual Flow Maps

From the synoptic flow maps obtained by the time-distance analysis, we have derived the mean rotational and meridional flow velocities. We remove the mean rotational and meridional velocities from the synoptic flow maps and obtain residual synoptic flow maps, which can reveal dynamics in local areas (Gizon, Duvall, & Larsen, 2001).

The residual synoptic flow maps are made for each Carrington rotation by merging together every 512-minute time-distance flow map after the mean differential rotation rates and meridional flows calculated separately for each rotation have been removed.

These flow maps have a high spatial resolution of 2.90 Mm per element and contain 1512×462 data points. However, in order to show the large-scale flows in this article and to make comparison with flow maps from ring-diagram analysis (Haber et al., 2002), we derive a larger scale flow velocity by averaging all the high spatial resolution velocities inside a square region with a side length of approximately 15°, taking into account spatial apodization of the ring analysis. Thus, we obtain larger scale flow maps of 96×48 data points separated in longitude and latitude by $3\overset{\circ}{.}75$. Significant spatial overlapping has been applied in this averaging procedure, and this simulates the synoptic flow maps obtained by the ring-diagram techniques (Haber et al., 2002). A more detailed comparison between the ring-diagram results and the time-distance inferences shown here is being carried out (Hindman et al., 2003).

Figure 7.5 presents the residual synoptic flow maps for Carrington Rotations 1923 and 1975 at the depth of $0 - 3$ Mm. Such maps display the flow patterns, especially the local variations, near the solar surface. Apparently, areas inside and around active regions show stronger and more systematic flows converging toward the active regions. The map of Carrington rotation CR1923, which was taken during a solar minimum year, has fewer active regions and shows weaker and less systematic flow patterns than the CR1975 map that has stronger magnetic activity. It is noticeable that even small active regions with relatively weak magnetic field have large-scale plasma flows toward them.

The flow fields beneath and around sunspots have been studied using MDI high-resolution and full-disk data (Chapter 3 of this dissertation; Kosovichev, Duvall, & Zhao, 2002). The converging and downward flows were found from near the photosphere to about 5 Mm in depth, the divergent flows were discovered deeper than 5 Mm. However, the larger scale flows beneath active regions may not have same structures as the small-scale flows beneath sunspots.

In Figure 7.6, we display the large-scale flow maps at two different depths around active region AR9433 during its passage of the central meridian in CR1975 taken in April, 2001. Near the solar surface at the depth of $0 - 3$ Mm, converging flows can be found toward the neutral line of this huge active region with a speed of approximately 40 m/s. This is generally consistent with the finding of converging flows toward the

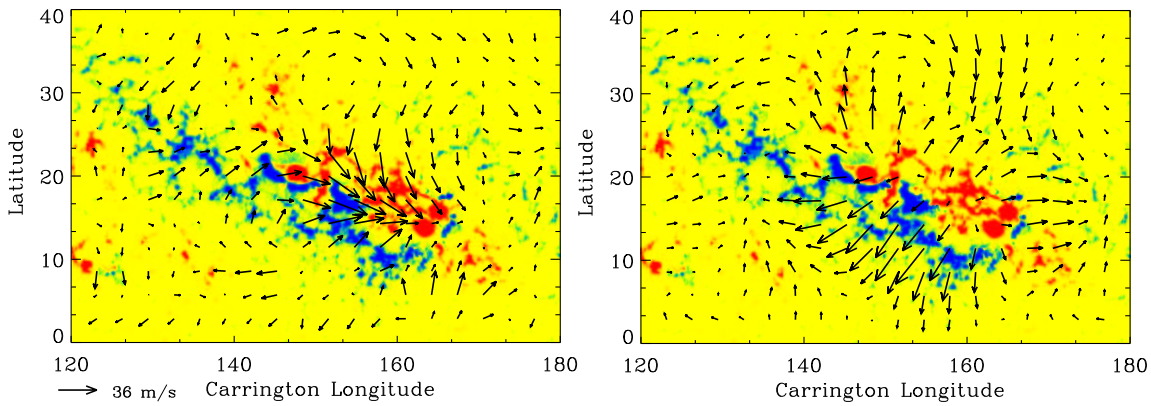

Figure 7.6: The large-scale averaged flow maps for a large active region AR9433 at two different depth intervals: 0 – 3 Mm *(left)* and 9 – 12 Mm *(right)*.

sunspot center (see Chapter 3), but with much smaller speed. However, the large-scale converging flow pattern of this active region seems to remain deeper than the small-scale converging flow pattern of sunspots. The large-scale divergent flows are only found beneath 9 Mm as shown in the right panel of Figure 7.6, while for the small-scale flows of sunspots this happens at a rather shallow depth of 5 Mm. Similar studies on active regions by ring-diagram analysis (Haber, Hindman, & Toomre , 2003) found that converging flows of active regions extended down to 10 Mm, even 16 Mm in some cases, which is much deeper than what we found. For studying flows around active region it is important to obtain small-scale flow maps, because the flows vary on relatively small scales.

7.5 Discussion and Conclusion

Using time-distance helioseismology measurements and inversions, we have obtained high-resolution synoptic horizontal flow maps for several solar rotations covering the first half of Solar Cycle 23 from minimum to maximum. The global-scale zonal and meridional flows, and the vorticity distributions are derived by averaging these high resolution data. Large-scale synoptic flow maps and large-scale flow patterns around active regions are obtained as well.

We find from this study that there is one, sometimes two, faster rotational bands residing in each hemisphere, as already shown in many previous studies (e.g., Howard & LaBonte, 1980; Kosovichev & Schou, 1997; Howe et al., 2000a). The activity belts are located at the poleward side of the faster zonal bands, and they migrate together towards the solar equator with the development of the solar cycle towards solar maximum. The zonal flows in the Southern and Northern hemispheres are not symmetrical, which was also pointed out in previous time-distance and ring-diagram analyses (Giles, 1999; Basu, Antia, & Tripathy, 1999; Haber et al., 2002).

From the meridional flows shown in Figure 7.3a, we find that flows of an order of 20 m/s remain mainly poleward at different depths through the whole period. Haber et al. (2002) reported an additional submerged cell seen in the Northern hemisphere from 1999 through 2001 beneath the depth of 6 Mm or so. However, in our study we do not see the equatorward flows occurring at the corresponding latitudes of the Northern hemisphere during these years, except perhaps in 2001 when some very small negative flows seem to appear above the latitude of 35° in the Northern hemisphere at the depth of 6 – 9 Mm. But it is possible that this small equatorward flow result from the inaccuracy of our P-angle corrections. Without the P-angle corrections, the meridional flows from our inversions also show the additional submerged cell in some deeper layers as claimed by Haber et al. (2002). This may indicate that the submerged meridional cell reported by Haber et al. (2002) resulted from the misalignment of the MDI instrument relative to the Sun's rotation axis. However, we cannot exclude the possibility that the reversed meridional flow cell may exist deeper than 12 Mm where our analyses have not reached. Furthermore, we should also recognize that although the meridional flow corrections give us reasonable results as shown in Figure 7.3a, there may be some other currently unknown sources that may affect the inference of meridional flows by local helioseismology techniques.

The residual meridional flows shown in Figure 7.3b present us some interesting results. By performing time-distance measurements, Chou & Dai (2001) and Beck, Gizon, & Duvall (2002) detected migrating outflows from the solar activity belts in addition to the normal poleward meridional flows. However, from the measurements of acoustic travel times alone without doing inversions, it is difficult to determine the

depth of the divergent flows. Based on our inversion results and the annulus ranges used in the two papers mentioned above, we estimate that divergent flows exist below a depth of approximately 18 Mm. The results shown in Figure 7.3b of our study also present a migrating signature of the residual meridional flows, but with a converging flow toward the activity belts from the solar surface to the depth of at least 12 Mm. This agrees with the results of converging residual meridional flows just below the photosphere, at a depth of 1 Mm or so, obtained by the f-modes analysis (Gizon, 2003). In addition, this signature is also generally consistent with the finding that the gradient of meridional flows steepens near the equator (Haber et al., 2002), and is also consistent with the variations of meridional flows after symmetrizing the flow structures of both hemispheres (Basu & Antia, 2003). From all these observations, we have a general picture of the residual meridional flows relative to the solar minimum: from the photosphere to the upper convection zone of approximately 12 Mm the residual meridional flows converge toward the solar activity belts, and below the depth of approximately 18 Mm the residual meridional flows diverge from the activity belts, thus forming circulation cells around the activity belts. Downdrafts are expected in the activity belts from the photosphere to the upper convection zone. These flows migrate toward the solar equator together with the activity belts as the solar cycle progresses. This general picture is similar to the schematic diagram proposed by Snodgrass (1987) and the theoretical prediction by Kleeorin & Ruzmaikin (1991). However, in this case, there must exist a depth where the converging flows turn over into the divergent flows, and detecting this turning point may be an important step in better understanding the mechanism of the formation of these flows. From the study of Chou & Dai (2001) and this investigation, the transition point is probably located somewhere between 12 and 18 Mm.

The extra meridional circulation cells associated with the magnetic activity in addition to the widely known poleward single cell pattern may have some interesting implications for dynamo theory. It is recognized that meridional circulation may play an important role in the regeneration of poloidal magnetic field and angular momentum transport (Wang, Sheeley, & Nash, 1991); accurate measurements of meridional flows have helped to build numerical simulations of the solar dynamo (Dikpati &

Charbonneau, 1999). The extra meridional circulation cell found in this study may add some new contents to these simulations, because this indicates that the meridional flows do not stay unchanged during the solar cycle, but vary with the location of the solar activity belts. Moreover, the additional converging flow structure may help transport more magnetic flux to the activity belts, but hamper the flux transported to the polar regions. On the other hand, the converging flows and the implied downdrafts in the activity belts may result from the hydrodynamic effects associated with cooling in magnetic regions, as recently discussed in a geostrophic flow model (Spruit, 2003). Or perhaps, the converging flows and downdrafts are just a global-scale manifestation of the strong converging flows and downdrafts in regions with strong magnetic fields.

The vorticity distribution is largely a linear function of latitude, with small deviations. Our calculations in Figure 7.4 show that the vorticity results mainly from the differential rotation. The vorticity inside supergranules and at the supergranular boundaries caused by the Coriolis force is approximately one order of magnitude smaller than vorticity generated by the differential rotation; this is apparently due to the cancellation of the opposite sign of vorticity in the supergranular converging and divergent flow regions. Since the flow vorticity is directly related to the α-effect, this may imply that in the upper convection zone, the local vorticity caused by the Coriolis force does not make a significant contribution to the α-effect on the global-scale compared to the differential rotation.

In this chapter, we have also presented large-scale flow maps for one large active region AR9433. It is found that the flows near the photosphere converge around both individual sunspots and the whole active region. However, for individual sunspots, divergent flows are found below the depth of 5 Mm, while for the whole active region, large-scale divergent flows are only found below the depth of approximately 9 Mm. This may imply that large active regions have deeper roots and deeper thermal and dynamical structures than individual sunspots. Combining the residual meridional flow structures discussed above, we find that converging flows are replaced by divergent flows beneath 5 Mm for individual sunspots, and the turning point for large active regions is at approximately 9 Mm, while the transition is located deeper than

12 Mm for the residual meridional flows at the solar activity belts. The underlying mechanisms for the converging and diverging flows around sunspots, active regions and activity belts are not well understood; it is possible, however, that the flows are the manifestation of a single mechanism being exhibited on different spatial scales.

As a summary, time-distance helioseismology has provided us with new information about solar dynamics in the upper convection zone and its relation to solar activity. We have found an extra meridional circulation cell around the solar activity belts, determined the distribution of vorticity, and studied the large-scale flows around a large active region. It is intriguing that despite the turbulence in the solar convection zone, it seems that the dynamics are also highly organized on large scales, which can be correlated with solar magnetic activity.

Chapter 8

Relationship Between Rotational Speed and Magnetic Fields

8.1 Introduction

It is well-known that sunspots and other solar magnetic features rotate faster than the surface plasma (Howard & Harvey, 1970). The sidereal rotation speeds of weak magnetic features and plages (Howard, Gilman, & Gilman, 1984; Komm, Howard, & Harvey, 1993), individual sunspots (Howard, Gilman, & Gilman, 1984; Sivaraman, Gupta, & Howard, 1993) and sunspot groups (Howard, 1992) have been studied for many years by different research groups by use of different observatory data (see reviews of Howard 1996 and Beck 2000). Such studies are deemed as diagnostics of subsurface conditions based on the assumption that the faster rotation of magnetic features was caused by the faster-rotating plasma in the interior where the magnetic features were anchored (Gilman & Foukal, 1979). By matching the sunspot surface speed with the solar interior rotational speed robustly derived by helioseismology (e.g., Thompson et al., 1996; Kosovichev et al., 1997; Howe et al., 2000a), several studies estimated the depth of sunspot roots for sunspots of different sizes and life spans (e.g., Hiremath, 2002; Sivaraman et al., 2003). Such studies are valuable for understanding the solar dynamo and origin of solar active regions. However, D'Silva & Howard (1994) proposed a different explanation, namely that effects of buoyancy

and drag coupled with the Coriolis force during the emergence of active regions might lead to the faster rotational speed.

Although many studies were done to infer the rotational speed of various solar magnetic features, the relationship between the rotational speed of the magnetic features and their magnetic strength has not yet been studied. In this chapter, we present our results on the relationship between the residual rotational speed and magnetic strength of weak magnetic features on the solar surface. The residual rotational speed relative to the mean rotational speed of the solar plasma is determined by time-distance helioseismology just beneath the solar surface.

8.2 Data Reduction

Same datasets and inversion results are used as in Chapter 7. One full Carrington rotation is selected from each year, from 1997 until 2002, for time-distance helioseismological analysis in this study.

At the start of each Carrington rotation, we select from the solar surface a central meridian region of 30° wide in longitude and from $-54°$ to 54° in latitude with 512 minutes nearly uninterrupted Dopplergram observation. Time-distance measurement and inversion are carried out for this selected region to derive the horizontal velocities from the photosphere to a depth of 12 Mm (see Chapters 3 and 7). Then, another 512-minute central meridian region observed 8 hours after the first one is processed in the same way. Such procedure is repeated till the end of the Carrington rotation. Approximately 90 such regions are processed for each rotation. Only the flow maps of the upper layer, $0 - 3$ Mm in depth, are used in this study. The pixel size at this depth is 0.24 heliographic degrees (or 2.9 Mm), though the spatial resolution may be slightly greater. Such a high spatial resolution enables us to overlap the horizontal flow maps over the corresponding magnetic field maps to study the relationship between the rotational speed of solar magnetic features and their magnetic strength. Figure 8.1 shows one example of the flow maps overlapping the corresponding magnetograms.

MDI also provides magnetograms with 96-minute cadence during the Dynamic Campaign periods. For each selected Carrington rotation, about 90 magnetic field

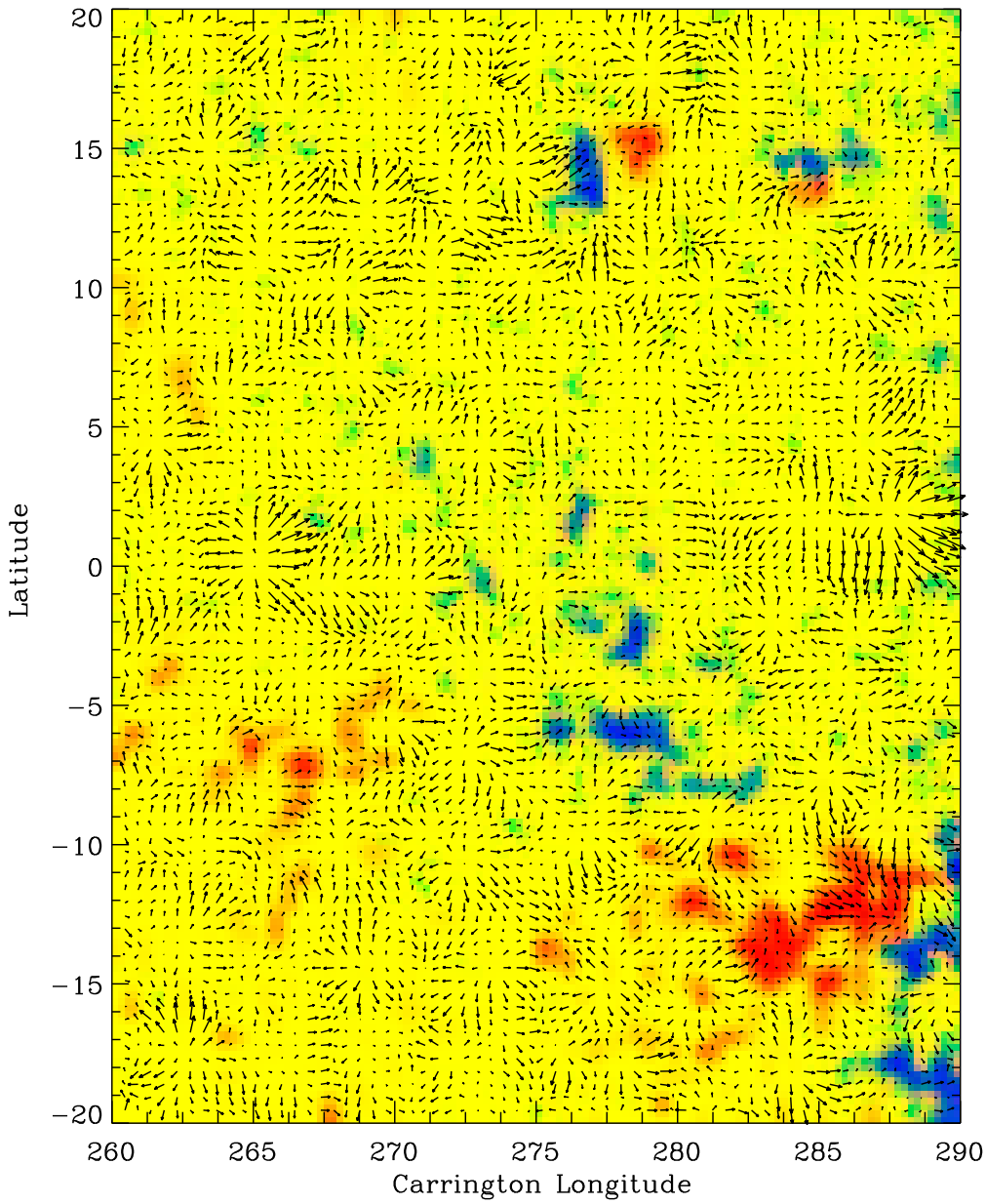

Figure 8.1: An example of the horizontal flow maps overlapping the corresponding magnetograms. The horizontal flows are plotted after 2×2 rebin in order to show the vectors clearly, and the magnetogram is kept at the original resolution. The plot shows a solar region at the disk center averaged from 08:00UT to 16:31UT of April 5, 2002.

maps are obtained covering the the same spatial regions and same temporal periods as those of the corresponding flow maps. In this study, we consider only weak magnetic features with magnetic field strength less than a few hundred Gauss, for which the parameter $\beta = 8\pi p/B^2 \gg 1$, thus magnetic field does not directly affect the plasma flows. Sunspots may have different origins and rotational speed compared to weak magnetic features, such as magnetic networks and plages. Therefore, in order to study the dependence of rotational speed on magnetic strength for weak magnetic features, all sunspots are masked out from the magnetic maps, but plages and other weak magnetic features surrounding the sunspots are kept.

8.3 Results

For each Carrington rotation, the mean latitudinal rotational speed is derived from all the flow maps of East-West velocity, and then subtracted from each flow map to get residual velocity maps. A scatter plot can be made for the magnetic field strength (the absolute value) of each pixel, between latitude $-30°$ to $30°$, and the corresponding residual East-West velocity. In order to increase the signal to noise ratio, we combine data points from six maps to make one such scatter plot. Figure 8.2(a) presents an example of the scatter plot. The residual velocity of individual elements can be eastward or westward, but the West-directed velocities clearly dominate over the East-directed flows with the increase of magnetic strength. To infer the dependence of the residual rotational speed of magnetized plasma on the magnetic strength, we average the East-West velocity of all pixels in 5 Gauss bins, from 0 to 600 Gauss. The average rotational velocity as a function of magnetic strength is plotted as the solid curve in Figure 8.2(a). For one Carrington rotation, we have approximately 15 such scatter plots, hence 15 functions of residual rotational speed relative to the magnetic strength. The averages are made again from these 15 functions to derive one function for the whole Carrington rotation which is shown in Figure 8.2(b). This plot shows the residual rotational velocity as a function of magnetic strength for Carrington rotation CR1964 of 2000. This function is nearly linear: the rotational speed increases with the magnetic field strength. By use of the weak magnetic features as tracers,

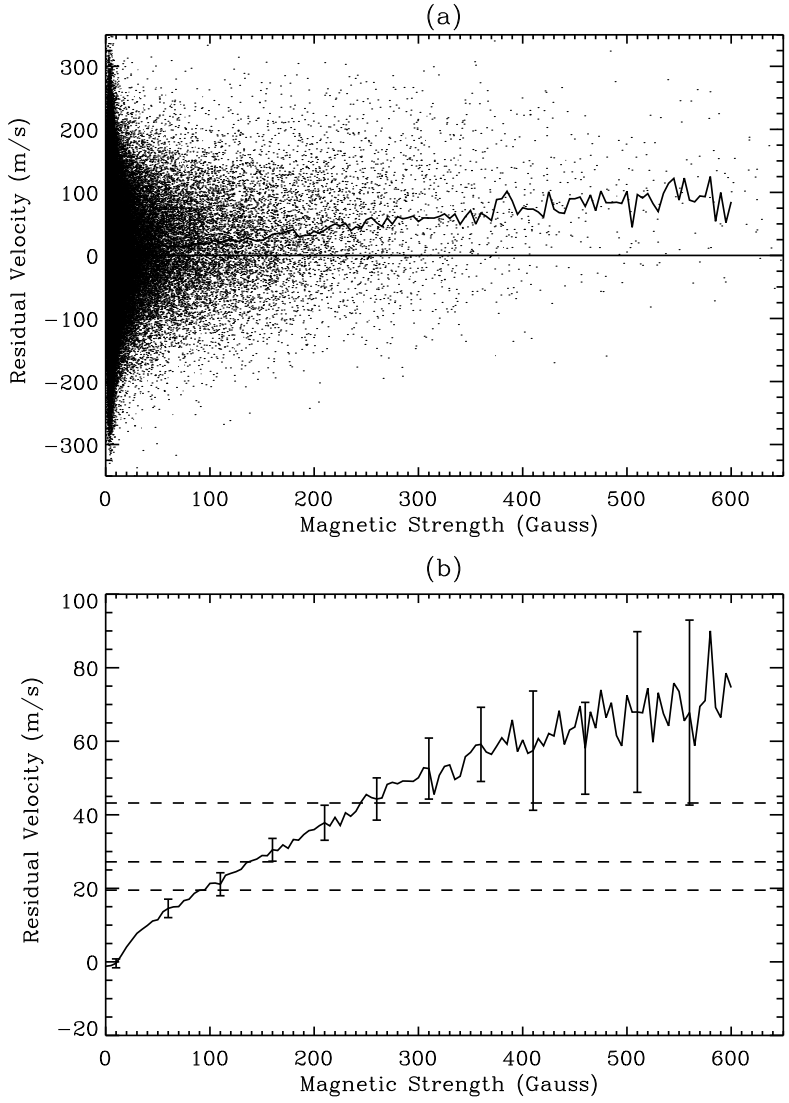

Figure 8.2: (a) Scatter plot of the residual East-West velocity versus the magnetic field strength for six 512-minute observation periods, in Carrington Rotation 1964 in 2000. The solid curve is an average of the residual velocities in 5 Gauss bins. (b) The average residual rotational velocity as a function of magnetic strength for CR1964. The error bars show one standard deviation of all 15 curves obtained for this solar rotation (for clarity, error bars are only displayed every 50 Gs). From the lower to upper, the three horizontal dashed lines represent the residual equatorial rotational speed of magnetic features inferred from Mt. Wilson data (Snodgrass & Ulrich, 1990), MDI data (Meunier, 1999) and Kitt Peak data (Komm, Howard, & Harvey, 1993), respectively.

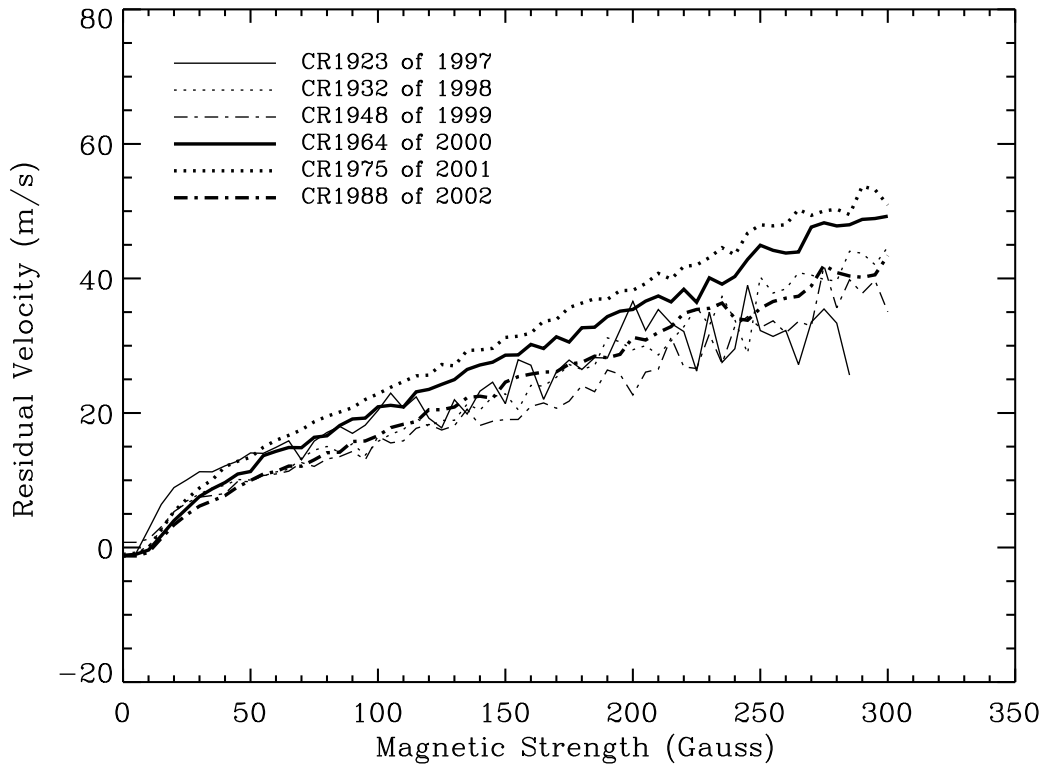

Figure 8.3: Residual rotational velocity as a function of the magnetic field strength for all studied Carrington rotations. For clarity, the error bars are not displayed, but they are similar as in Figure 8.2(b) except of CR1923 which has slightly larger error bars.

various researchers have derived slightly different rotational rate of magnetic features. For comparison, three previous results derived by different researchers are plotted in Figure 8.2(b), all of which fall in the ranges of the residual velocity function.

Following the same procedure, we derive the residual rotational velocity as a function of magnetic strength for each Carrington rotation selected from 1997 to 2002. Figure 8.3 presents all these functions covering 0 to 300 Gauss, beyond which data become very noisy for Carrington rotations in solar minimum years. Clearly, all the functions display approximately a linear relationship between the residual rotational velocity of weak magnetic features and their magnetic strength. However, these functions for different Carrington rotations are not the same, but seem to vary

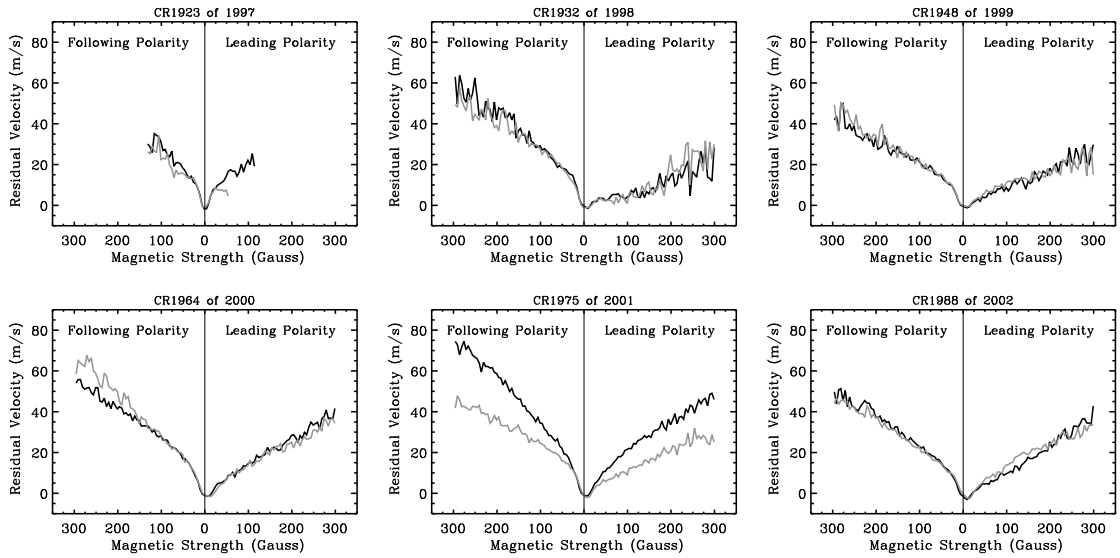

Figure 8.4: Residual rotational velocity versus the magnetic field strength for the leading and following polarities in both hemispheres. The black curves represent the functions for the Northern Hemisphere, and the gray curves represent the functions for the Southern Hemisphere.

with the phase of the solar cycle. The curves for the years 2000 and 2001, the maximum activity years, have the greatest slopes; the curves for the years 1997 – 1999 and 2002, when the solar activity was moderate, have smaller slopes. That is, the residual rotational speed of magnetic elements during the solar maximum years is faster than the speed of elements of same magnetic strength during the years with moderate activity. We have tried to derive such functions for various latitudes in each Carrington rotation, but did not find clear latitudinal dependence.

Magnetic features of leading and following polarities may have different residual rotational speed. By employing the similar procedure used above, we derive the rotational velocity of magnetic features separately for leading and following magnetic fields in both Northern and Southern hemispheres. Figure 8.4 presents the results. Except perhaps for CR1975 in 2001, the functions for the Northern and Southern hemispheres are strikingly similar. The differences in the two curves for CR1975 may result from the significantly different magnetic activity levels in the two hemispheres during this Carrington rotation: the Northern hemisphere had much stronger

magnetic activity than the Southern hemisphere. The residual velocities for larger magnetic strength in CR1923 are not able to be derived reliably due to small number of pixels with larger magnetic strength. Nevertheless, for all the Carrington rotations studied covering from near the solar activity minimum to past the maximum of Solar Cycle 23, the plots show that the magnetic elements of the following polarity rotate faster than those of the leading polarity with the same magnetic strength. The increase of the residual rotational velocity with the magnetic strength is particularly fast for elements of the following polarity when the magnetic strength is less than ~ 50 Gauss.

8.4 Discussion

In this study, we have derived the rotational speed of magnetic features relative to the mean speed of the Sun's differential rotation as a function of magnetic field strength at different phases of the current solar cycle, and found that these functions are nearly linear for all Carrington rotations studied, from the solar activity minimum to maximum: the stronger the magnetic strength, the faster the magnetic elements rotate. Generally, this is consistent with the previous finding that sunspots rotate faster than plages, because one would expect sunspots are composed of magnetic elements with stronger magnetic strength than magnetic networks and plages.

It was suggested that the faster rotational rate of magnetic features could be due to the faster rotational rate of the solar interior where these features were anchored (Gilman & Foukal, 1979; Sivaraman et al., 2003). Following this suggestion, by matching the residual rotational velocity of magnetic features with the solar interior rotational rate from helioseismology studies (Howe et al., 2000a), we are able to derive the anchoring depth of the magnetic elements as a function of their magnetic strength. From our results, the magnetic features with a strength of 600 Gauss are rooted at a radius of approximately 0.95 $R_\odot$. Perhaps, this indicates that the weak magnetic features such as networks, plages may be generated in the surface shear layer which is located above 0.95 $R_\odot$, rather than in deeper convection zone; or perhaps, these features are formed by the dissipated magnetic elements of the decayed

active regions which do not submerge deep into the solar interior. This is also in agreement with the local dynamo theory (e.g., Cattaneo, 1999) which suggested that weak and small-scale magnetic field on the Sun might be generated locally, very close to the solar surface. Furthermore, the linear dependence of the rotational speed on the magnetic field strength found in this study should be addressed by local dynamo theories.

However, there may be other explanations for the fast rotation of magnetic features, such as the Coriolis force in the course of magnetic emergence (D'Silva & Howard, 1994). The linear dependence of the residual rotational velocity on the magnetic strength may inspire us for other interpretations. Naively following the suggestion of Schüssler (1981) which was proposed to explain the global faster zonal flows known as "torsional oscillation" (Howard & LaBonte, 1980), the Lorentz force per unit volume f_L is proportional to $|B_{\rm tor}| \cdot |B_{\rm pol}|/L$, where $B_{\rm tor}$ is toroidal field, $B_{\rm pol}$ is poloidal field and L is the length scale of magnetic elements. Suppose that the kinetic energy density of the magnetized plasma, $\frac{1}{2}\rho v^2$, is achieved only from the influence of Lorentz force, one may expect $v \propto (|B_{\rm tor}| \cdot |B_{\rm pol}|)^{1/2}$. Intuitively, this may suggest the velocity is linearly proportional to the observed magnetic strength. However, this back-of-the-envelope interpretation does not explain the difference in the rotational speed of the leading and following polarities.

The following two factors may have played some roles in the linear relationship found in this study: 1) all the magnetic elements may rotate with the same speed, but the pixels observed by MDI may be composed of fast magnetic elements and slow unmagnetized plasma, hence our measurements are just averages of these two different speeds; 2) all magnetic features may rotate with the same speed, the unavoidable smoothing involved in the measurement and inversion procedure may reduce the speed of boundaries of these features. In both cases, one may expect the largest residual velocity should be less than or equal to the speed found by using magnetic features as tracers. However, Figure 8.2(b) clearly shows that this is not the case. Therefore, despite that the above two factors may inevitably contribute to the linear relationship found in this study, they do not play major roles, although we can not determine how much they contribute because the filling factor is unknown.

In this study, we have found that the functions of the residual rotational velocity versus the magnetic field strength have larger slopes for the solar maximum years (2000 and 2001) than for the intermediate activity years (Figure 8.3). By using sunspots as tracers, Gilman & Howard (1984) found that the residual rotational speed of sunspots was often faster in the activity maximum and minimum years than in the intermediate years. They interpreted the change of sunspots' rotational speed as resulting from the change of solar interior rotation rate with the solar cycle, but recent helioseismological studies did not show such significant change in the rotation rate. Our finding for the weak magnetic features is basically in agreement with the observations for sunspots: the magnetized plasma on the solar surface usually rotates faster during solar maximum years than during the years with moderate activity. This effect should not be related with or caused by the torsional oscillation, because the mean zonal flows are already removed from our data. Interpretation of this phenomenon may require more observational and theoretical studies.

Figure 8.4 suggests that for the same magnetic strength, magnetic features of the following polarity often have faster rotational speed than those of the leading polarity. Howard (1996) summarized previous results and showed that the leading sunspots often rotate faster than the following sunspots, but oppositely, the following portions of weak magnetic features are often faster than the leading portions. Our results confirm his conclusion. Howard (1996) suggested that the faster rotation of the following polarity might be caused by the faster diffusion to the East of the following magnetic flux, which would give an appearance of faster rotation of the following portions. However, our results are based on averaged plasma velocities of the magnetic elements rather than on tracking motions of specific magnetic features. Therefore, the faster rotation of the following polarity should not be just an apparent, but a real motion. This phenomenon may have some interesting implications in understanding magnetic network cancellation. The explanation of this observation may require more studies and improvement in the solar velocity measurements.

Chapter 9

Summary and Perspective

This thesis has presented a variety of applications of time-distance helioseismology measurements and inversions, and many new results have been obtained by this technique. In the following, I summarize all the major results presented in the previous chapters as the first part of this chapter, and discuss perspective of future works in the second part.

9.1 Summary

It has been proved that time-distance helioseismology is a useful technique to study solar interior sound-speed structures and dynamics on both small and large scales. Two inversion techniques, one based on the LSQR algorithm and one based on Multi-Channel Deconvolution, have been developed; comparisons between these two inversion techniques give reasonable agreement.

Time-distance measurement and inversion have been applied to study local structures: sunspots and supergranules. For sunspots, it was found that the sound-speed is slower relative to the quiet Sun immediately below the solar surface, but faster than the quiet Sun below the depth of approximately 5 Mm. Converging and downward flows were revealed beneath sunspots, which may play important roles in keeping sunspots stable for more than a few days even a few weeks, and also may be observational evidence for the sunspot cluster model (Parker, 1979). However, below the

regions of converging and downward flows, divergent and upward flows were seen.

For supergranules, the vertical velocity cannot be reliably derived due to the strong cross-talk effects between the weak vertical velocity and the strong divergence (convergence) at the center (boundary) of supergranules. However, the horizontal velocities near the surface and at some depth display a convective cell structure. The correlation coefficients between the divergences at the surface and at a few different depths suggest that the depth of supergranules is approximately 14 Mm, close to the expectation of many researchers.

A sunspot with fast self-rotation was studied by use of time-distance helioseismology, in order to detect the interior structure of this unusual sunspot, and try to connect the subsurface flow fields with the coronal activities. By comparing the subsurface sound-speed structures with the photospheric magnetic field, a structural twist was found beneath the sunspot, which may explain the twists of vector magnetic field observed in the photosphere. A vortex, which is in the same direction as seen by white light movies, was found beneath the surface, but an opposite vortex was found in some deeper layers at depths of about 12 Mm. Such flow fields could significantly twist the magnetic flux and store a huge amount of magnetic energy and helicity for solar eruptions in the chromosphere and corona. A statistical study of 88 active regions in both hemispheres showed that the sign of subsurface kinetic helicity has a slight hemispheric preference, even weaker than the hemispheric preference found by the statistics of magnetic helicity. It also showed that the sign of kinetic helicity is opposite to that of the magnetic helicity in the same solar hemisphere.

Large-scale properties, such as zonal flows, meridional flows and vorticity distribution, were also derived from our studies of one Carrington rotation each year from 1996 to 2002, covering from the solar minimum to maximum. Synoptic flow maps were constructed from the surface to a depth of 12 Mm for all the selected Carrington rotations. Faster zonal flows, residing on the equatorial side of the activity zones and also known as torsional oscillation, were found from our study and had similar magnitudes as obtained by previous researchers. The residual meridional flows, after the meridional flows of the minimum year were subtracted from the flows of all the following years, display a converging flow toward the activity zones in both

hemispheres, which implies downward flows in the activity zones. These properties migrate together with the activity zones toward the solar equator with the evolution of the solar cycle toward its maximum. The global vorticity distribution is largely a linear function of latitude, and mainly results from solar differential rotation but with some variations.

Once we had synoptic flow maps, we overlapped the synoptic flow map with the magnetic synoptic map to study the relationship between the magnetic field strength and the rotational speed of magnetic features on the solar surface. After masking the major active regions, we found that the residual rotational speed of weak magnetic features, pores and network structures, is nearly linearly proportional to its magnetic field strength. This linear relationship varies with the evolution of the solar cycle, and the slope is largest during solar maximum years. In addition, it was found that the plasma of following polarity has a faster speed than the plasma of leading polarity with the same magnetic field strength.

9.2 Perspective

Time-distance helioseismology has already revealed many new results in the solar interior sound-speed variations and dynamics. Some efforts are still ongoing and should be done in the future to improve the accuracy and reliability of time-distance helioseismology results.

9.2.1 Artificial Data from Numerical Simulation

Some artificial models have been made and used in Chapters 3, 4 and 5 of this thesis, however, these artificial data were simply created to test the reliability of inversion codes, but might not represent the reality inside the Sun.

More realistic artificial data are necessary to test time-distance helioseismology, including both measurements and inversions. Such data should be simulated by employing the compressible hydrodynamical equations, or perhaps even magnetohydrodynamical equations, including perhaps radiative transfer equations. The final

dataset should have long enough time series, large enough surface areas with spatial resolution better than or comparable to the real observation, and more importantly, acoustic waves should be present through the plasma. Granulation, and maybe supergranulation, should be expectedly obtained in such numerical simulations. Then, time-distance measurements and inversions are applied upon such numerical data, in an attempt to reveal the structures and flow fields initially set inside this numerical model. Such a numerical experiment could fully test the reliability of time-distance helioseismology, and estimate the systematic and random errors involved in this technique. Such an effort is ongoing.

9.2.2 Wave Approximation

All results that have been presented in this thesis are based on the ray-approximation. As already discussed in Chapter 2, the wave approximations, including Fresnel-zone approximation and Born approximation, have proved that for the sound-speed perturbation, the major results derived from ray-approximation are valid (with no phase-velocity filtering applied to both kernels), although the depth and magnitude of features are slightly at odds (Couvidat et al., 2004). The wave-approximation inversion kernels for flow fields, with the phase-velocity filtering being applied as well, are currently under development, and soon a comparison between velocities obtained by different inversion kernels will be available.

However, since the solar regions in our study are often sunspots or active regions, where strong magnetic fields are present, it is considerably difficult to derive the proper inversion kernels with different scales of magnetic field taken into account, and also it is difficult to disentangle the effects of magnetoacoustic waves from the normal acoustic waves, as also pointed out in Chapter 2. Therefore, considerable efforts should be put on modeling the magnetic-acoustic interaction for better interpreting time-distance results in solar active regions.

9.2.3 Deep-focus Time-distance Helioseismology

Conceivably, more measurements are often necessary to derive results with better accuracy. Deep-focus time-distance helioseismology is designed to complement surface-focus time-distance helioseismology, the sole technique used through this thesis; deep-focus can bring us more information of deeper structures. Deep-focus time-distance helioseismology is introduced in Appendix B of this thesis.

Some attempts (see Appendix B) have also been made to incorporate the deep-focus and surface-focus time-distance measurements, then inversions were performed based on both measurements. Although the major results obtained from such inversions, e.g., faster sound-speed, converging and downward plasma flows beneath sunspots, are similar, the detailed sound-speed structures, the flow magnitudes and directions are somewhat different with the inversion results from surface-focus alone.

The differences may be caused by a few aspects: the measurements from the deep-focus time-distance are significantly noisier than the measurements from surface-focus, which may introduce many unpredictable uncertainties to the inversion results; the accuracy of inversion kernels derived from the ray-approximation for the deep-focus time-distance is unknown, and may partially introduce some errors to the inversion results; without knowledge of the noise level (or error covariance) of both surface- and deep-focus time-distance measurements, it is hard to determine the proper regularization parameters and infer the best possible results. Therefore, it is very important to design better schemes for the deep-focus time-distance measurements, which can optimally cover the regions of interest and depths to complement the surface-focus time-distance. It is equally important to derive the deep-focus wave-approximation inversion kernels.

9.2.4 Connections between Subsurface Flows and Coronal Activity

This may be a very interesting topic for the future study, and potentially a new field. It is well known that the shearing flows at the footpoints of solar flares play a very important role in triggering solar flares, and it is also known that, part of, or even

most part of the magnetic energy released by solar flares is built up under the solar photosphere. Thus, it is interesting to study the connections between subsurface flow fields and coronal activity.

Three-dimensional subsurface velocity derived from time-distance inversions enables us to compute the subsurface kinetic helicity, and to look for shearing or vortical flows under active regions. Abnormal kinetic helicity and shearing flows may be pointers to potential solar eruptions a few minutes or hours later. Therefore, such a study can not only help us to understand the helicity and energy build-up procedure below the solar surface to power solar eruptions, but also can identify the indicators to forecast the solar eruptions well ahead the occurrence of solar flares.

Some preliminary studies have been performed, trying to establish such connections by analyzing the "Thanksgiving events" of 2000. A series of five X-class solar flares occurred on November 23 and 24, 2000 in NOAA AR9236. Preliminary time-distance analyses have shown that for the first three cases of X-class flares, approximately 4 hours before the onset of each flare, vortical flows were found around the footpoints of the solar flares, and abnormal converging flows were found flowing toward the footpoints. If these features are able to be confirmed in other solar flares, these features may serve as indicators of potential solar eruptions. The major difficulty is that the temporal resolution of time-distance is rather low, and spatial resolution from time-distance results is also low compared to the size of solar flare footpoints.

I believe this is a very interesting and novel topic, and is definitely worth substantial research effort in the future.

Appendix A

Procedures of Doing Time-Distance Measurement

This appendix is complimentary to Chapter 2, in which I have described the detailed procedures of doing time-distance measurement and inversion. I present in this appendix some part of the scripts, codes, and important parameters that I used in my study, so that readers of this dissertation may be able to repeat all the work included in this dissertation.

A.1 Data Preparation

It is strongly recommended that time-distance analysis be done on the central region of the solar disk, so that the side-effects caused by the large image distortion in limb regions may be limited to the minimum. Once the region of interest and the time period are decided, one should determine the Carrington longitude and latitude of the center of this region, as well as the MDI time index that the time period of interest corresponds to. To convert the real time of observation to the corresponding MDI time index, `time_index` is a useful command.

In order to perform FFT effectively, I often select a solar region with a size 256×256, and an observation duration of 512 minutes. Assume that we are analyzing a region with its center located at Carrington longitude of 100° and latitude of 10°

in the northern hemisphere. The time period we are analyzing is from 00:00UT to 08:31UT on January 1, 2000. Running the command `time_index`, we can get

```
csh> time_index in=61344
hour 2000.01.01_00:00:00_TAI 3680640 61344 2556 1325376000.000 10224 85
```

Then we know that the corresponding MDI hour indices for our analysis period are from 61344 to 61351. Suppose that the datasets are from MDI full-disk observation. The script we run to track the region of interest and remap the region by utilizing Postel's projection is like the following:

```
!setenv mdi /tmp01/junwei/data_proc
p=fastrack d=1 \
  in=prog:mdi,level:lev1.5,series:fd_V_01h[61344-61351],sel:[00-31] \
  out=prog:mdi,level:lev2_track,series:vtrack_15_30_720[0] \
  scale=0.12 \
  rows=256 cols=256 \
  lat=10.0 lon=100.0 map=Postels \
  a0=0.0 a2=0.0 a4=0.0\
  n=0 z=0 v=1
```

The first line in the script is to provide a working directory where the final data are stored. The line with `a0, a2 and a4` is to give a rotation rate to be removed during the tracking procedure. To assign all these three values to be 0 is what I normally use, i.e., the solid Carrington rotation rate is removed from the data for all latitudes. Different tracking rate may be used by changing values of `a0, a2 and a4`. The argument `map=Postels` indicate that the mapping projection used is Postel's projection, whereas other projections, such as "rectangular", "orthographic", may be used. The dataset is then ready for time-distance analysis after the mean image of all these 512 images is removed from each image.

A.2 Filtering

As introduced in Chapter 2, two filters are usually applied on the dataset in the Fourier domain. One is to filter out the f-mode and all signals below the f-ridge,

and the equations for the filter are given in equation 2.2; the other is the phase-velocity filter.

The choices of phase-velocity filter parameters, including the annulus ranges, the ratio of k/ω and the Full Width at Half Maximum (FWHM) of the Gaussian curve, are essential to the accuracy of the computed travel times. All through this dissertation, I used eleven annuli for computation of time-distance, and in Table A.1, I present all the parameters used in the computation.

	Annulus Range	k/ω Ratio	FWHM
1	0°.306 - 0°.714	2.92	1.00
2	0°.510 - 0°.918	3.40	1.00
3	0°.714 - 1°.190	4.00	1.00
4	1°.190 - 1°.598	5.675	1.47
5	1°.598 - 2°.414	8.11	2.00
6	2°.176 - 2°.856	9.08	1.16
7	2°.652 - 3°.400	9.90	1.20
8	3°.196 - 3°.876	10.90	1.36
9	3°.638 - 4°.454	11.95	1.70
10	4°.182 - 4°.930	13.07	1.44
11	4°.692 - 5°.372	13.98	1.30

Table A.1: Parameters used to perform the phase-velocity filtering. Units for k/ω ratio and FWHM are both m/s.

A.3 Cross-Correlation and Fitting

Following equation 2.3, the discrete equations used to compute the cross-covariance between two signal series are:

$$r_{xy}(L) = \begin{cases} \frac{1}{N} \sum_{k=0}^{N-L-1} (x_{k+L} - \bar{x})(y_k - \bar{y}) & \text{for} L < 0 \\ \frac{1}{N} \sum_{k=0}^{N-L-1} (x_k - \bar{x})(y_{k+L} - \bar{y}) & \text{for} L \geq 0 \end{cases} \tag{A.1}$$

where x and y are the two signal series, L is time lag with both positive and negative values, and $r_{xy}(L)$ is the resultant cross-covariance function. IDL subroutine `c_correlate.pro` can be called directly for such a computation:

```
r = C_CORRELATE(x, y, L, /COVARIANCE)
```

As pointed out in §2.1, the IDL function `lmfit.pro`, a function to perform non-linear least squares fitting, can be used to fit the Gabor function obtained from the cross-correlation. The following is a sample IDL code to do the fitting:

```
FUNCTION myfunct, x, a

bx=EXP(-a(1)^2/4.*((x-a(2))^2))
cx=COS(a(3)*(x-a(4)))
RETURN,[[a(0)*bx*cx], [bx*cx], $
       [-0.5*a(0)*a(1)*((x-a(2))^2)*bx*cx], $
       [a(0)*bx*cx*(x-a(2))*(a(1)^2)/2.], $
       [a(0)*bx*(x-a(4))*(-SIN(a(3)*(x-a(4))))], $
       [a(0)*bx*a(3)*SIN(a(3)*(x-a(4)))]]

END

PRO lmqt_0, r, bb

x=FINDGEN(19)+2.
dat=FLTARR(19)
dat=r(101:119)/max(r)
aa=[1.0, 0.2, 10.5, 1.5, 12.1]
coefs=LMFIT(x, dat, aa, FUNCTION_NAME='myfunct',TOL=1.e-6,ITMAX=35)
bb=aa(4)

RETURN
END
```

The parameters of `r` and `aa` should be changed accordingly for different annulus ranges.

Certainly, the subroutines `c_correlate.pro` and `lmfit.pro` provided by IDL are not computational efficient in practice. Both of these two subroutines were translated into *FORTRAN* to meet the requirement of a large number of computations.

Appendix B

Deep-Focus Time-Distance

B.1 Deep-focus Time-Distance Measurement

Throughout this dissertation before this appendix, when we talk about time-distance, we mean surface-focus time-distance. As we know, more measurements can help to improve the accuracy of inversion results. Deep-focus time-distance was designed to meet such a requirement, and at the same time, bring up more information from the deeper layers of the solar interior.

As shown in the schematic plot of Figure B.1, surface-focus time-distance has the central point at the solar surface, hence it is like that its "focus" is at the surface, while deep-focus time-distance has its "focus" somewhere beneath the surface. Presumably, deep-focus should be more accurate in determining the deeper structures and dynamics. For the deep-focus scheme, by moving one set of rays to the left or to the right, one can move the "focus" point up or down. Therefore, one can design optimal schemes combining both surface- and deep-focus measurements to cover all the depths of interest in order to get better inversion results.

Basically, the procedure of performing deep-focus time-distance measurement is similar to that of surface-focus time-distance, except that for the surface-focus, we only have one central point, while for the deep-focus, we have an annulus of many points. Filtering, cross-correlation computation, and fitting subroutines are all the same, or sometimes with only slight modifications from surface-focus subroutines.

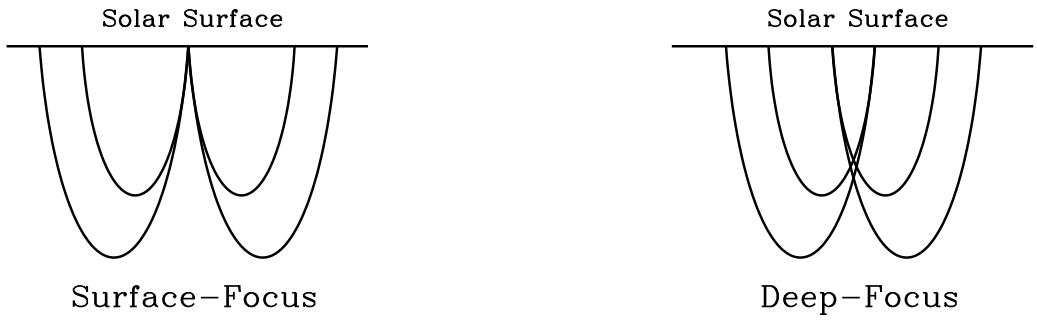

Figure B.1: A schematic plot to show the surface- and deep-focus time-distance measurement schemes.

An attempt has been made to combine both surface- and deep-focus time-distance measurements to study the subsurface dynamics of a sunspot. High resolution MDI observations of NOAA AR9236 on November 24, 2000 were selected for such an attempt. Eleven surface-focus measurements with different annulus ranges were performed based on the parameters given in Appendix A, and nine sets of deep-focus measurements were performed. All the necessary parameters to perform the deep-focus measurements are given in Table B.1. Please note that these parameters are just from one of my attempts to do deep-focus time-distance measurements. They are perhaps inaccurate, and probably, the choices of inner and outer annulus ranges are not optimal. Clearly, further efforts should be put into optimizing the measurement

	Inner Annulus Range	Outer Annulus Range	k/ω Ratio (m/s)
1	0°.136 - 0°.204	0°.544 - 1°.020	4.00
2	0°.306 - 0°.374	0°.850 - 1°.258	5.675
3	0°.578 - 0°.644	1°.054 - 1°.802	8.11
4	0°.918 - 0°.986	1°.190 - 1°.938	9.08
5	1°.122 - 1°.190	1°.462 - 2°.278	9.90
6	1°.326 - 1°.394	1°.802 - 2°.550	10.90
7	1°.530 - 1°.598	2°.074 - 2°.890	11.95
8	1°.734 - 1°.870	2°.414 - 3°.162	13.07
9	1°.938 - 2°.074	2°.686 - 3°.434	13.98

Table B.1: Parameters, including the inner and outer annuli ranges, and k/ω ratios, for the deep-focus time-distance measurements.

schemes, as discussed in Chapter 9.

B.2 Inversion Combining Surface- and Deep-Focus

It is interesting to see whether the combination of both surface- and deep-focus time-distance measurements can improve the inversion results, and how the inversion results compare with the previous inversions based on the surface-focus measurements only.

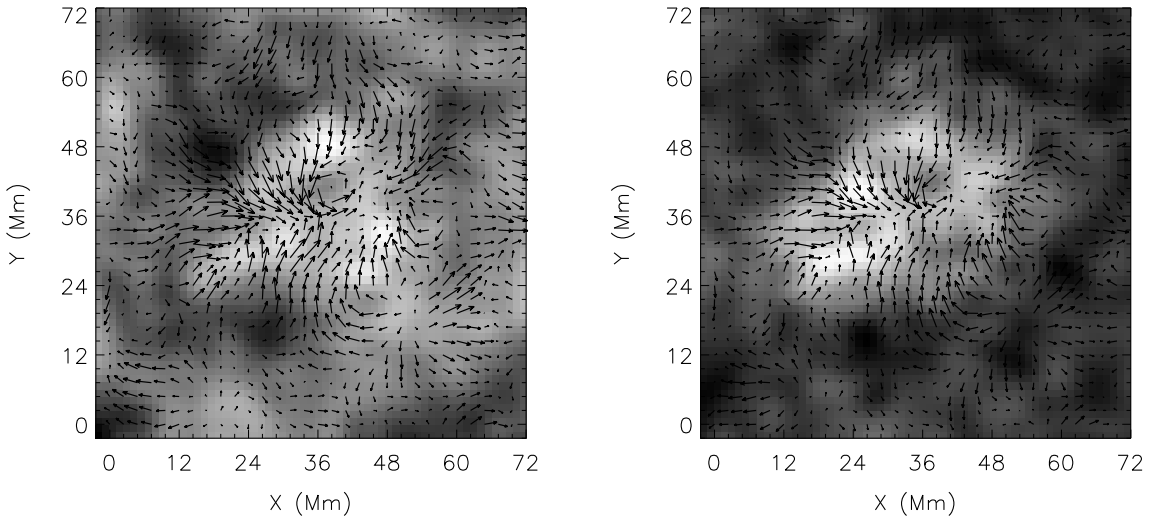

Figure B.2: Inversion results at the depth of 0 – 3 Mm for AR9236 from surface-focus measurements alone (*left*) and from the combination of surface- and deep-focus measurements (*right*). The background images show the vertical velocity with light color representing downward flows, and vectors show the horizontal velocity after a 2×2 rebin.

The inversion kernels for the deep-focus measurements were also derived based on the ray-approximation, like for the surface-focus measurements described in Chapter 2.

Combining both surface- and deep-focus measurements, inversions were performed by use of LSQR algorithm. Inversions were also performed by use of surface-focus measurements alone by the same inversion technique. Results obtained from both approaches at the depth of 0 – 3 Mm and at the depth of 6 – 9 Mm are shown in

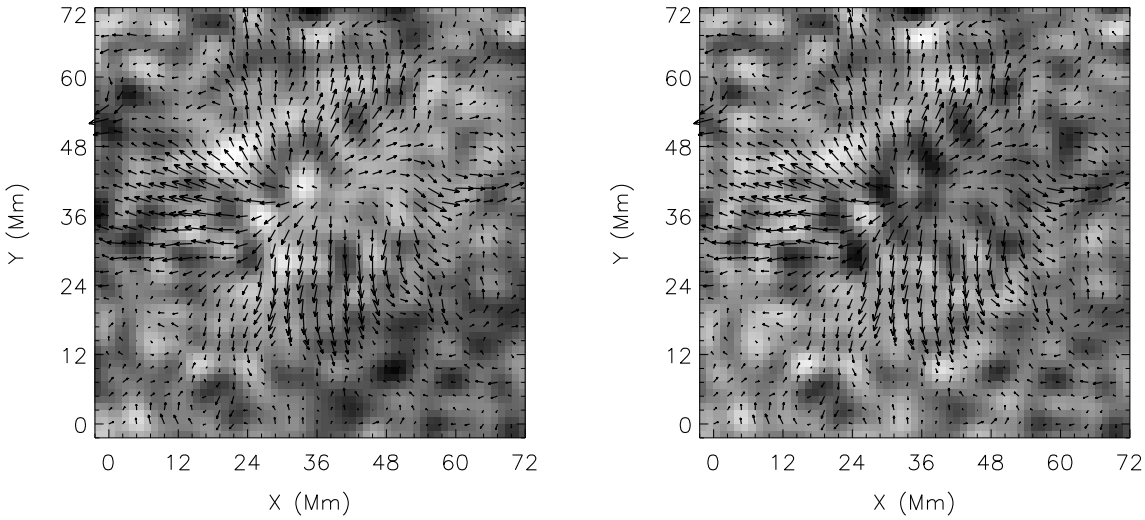

Figure B.3: Same as Figure B.2, but for the depth of 6 – 9 Mm.

Figure B.2 and B.3, respectively.

It can be obviously seen that basically, results from the both inversion approaches agree with each other, although the details differ from slightly to significantly at different locations. Near the surface, both inversions show downdrafts and converging flows toward the umbra of the sunspot. The vortex structure located at the center of the sunspot is seen in both inversions. At the depth of 6 – 9 Mm, both inversions show strong outflows from the sunspot, but the vertical flows differ significantly: results from the combination show clearly upward flows while results from surface-focus alone show somewhat mixed upward and downward directed flows.

At present, it is hard to discern whether one inversion is superior to the other, because the deep-focus measurement are still at its initial stage, and especially, the measurement scheme design used in this study is somewhat arbitrary, perhaps far from its optimal form. On the other hand, although it is proved that the ray-approximation kernels agree well with the wave-approximation kernels for the surface-focus time-distance inversions (Couvidat et al., 2004), it is not yet known whether the application of ray-approximation kernels on the deep-focus inversion is suitable. Additionally, from the measurements I made, it is obvious that the deep-focus measurements have larger noise level than the surface-focus ones. Then there is difficulty in choosing

an optimal damping coefficient input for the LSQR to balance the different noise contributions from both sets of measurements. This factor may also play a role in the differences between inversion results.

Undoubtedly, for the purpose to study deeper areas of the Sun more reliably, deep-focus time-distance must be better developed in the future with the measurement schemes better designed to cover all depths. At the same time, wave-approximation inversion kernels for the deep-focus time-distance helioseismology should be developed as well.

Bibliography

Antia, H. M., & Basu, S. 2000, *Astrophys. J.*, 541, 442

Bao, S. D., & Zhang, H. Q. 1998, *Astrophys. J.*, 496, L43

Basu, S., & Antia, H. M. 2003, *Astrophys. J.*, 585, 553

Basu, S., Antia, H. M., & Tripathy, S. C. 1999, *Astrophys. J.*, 512, 458

Basu, S., et al. 1997, *Mon. Not. R. Astron. Soc.*, 292, 243

Beck, J. G. 2000, *Solar Phys.*, 191, 47

Beck, J. G., Gizon, L., & Duvall, T. L., Jr. 2002, *Astrophys. J.*, 575, L47

Birch, A. C. 2002, Ph.D. Thesis, Stanford Univer.

Birch, A. C., & Kosovichev, A. G. 2000, *Solar Phys.*, 192, 193

Birch, A. C., Kosovichev, A. G., Price, G. H., & Schlottmann, R. B. 2001, *Astrophys. J.*, 561, L229

Bogart, R. S., et al. 1995, in *Proceedings of the 4th SOHO Workshop*, 147

Brandenburg, A., Nordlund, Å, Pulkkinen, P., Stein, R. F., & Tuominen, I. 1990, *Astron. Astrophys.*, 232, 277

Brandenburg, A., Sarr, S. H., & Turpin, C. R. 1998, *Astrophys. J.*, 498, L51

Brandenburg, A., & Schmitt, D. 1998, *Astron. Astrophys.*, 338, L55

Braun, D. C., Duvall, T. L., Jr., & Labonte, B. J. 1988, *Astrophys. J.*, 335, 1015

Braun, D. C., & Lindsey, C. 2000, *Solar Phys.*, 192, 307

Braun, D. C., & Lindsey, C. 2003, in *Proceedings of SOHO 12/ GONG+ 2002 Workshop, Local and Global Helioseismology: the Present and Future*, ed. H. Sawaya-Lacoste (ESA SP-517, Noordwijk: ESA), 15

Brown, D. S., Nightingale, R. W., Alexander, D., Schrijver, C. J., Metcalf, T. R., Shine, R. A., Title, A. M., & Wolfson, C. J. 2003, *Solar Phys.*, 216, 79

Brun, A. S., & Toomre, J. 2002, *Astrophys. J.*, 570, 865

Canfield, R. C., & Pevtsov, A. A. 1999, in *Magnetic Helicity in Space and Laboratory Plasmas* (Geophys. Monogr. 111; Washington DC: AGU), 197

Canfield, R. C., & Pevtsov, A. A. 2000, *J. Astrophys. Astr.*, 21, 213

Cattaneo, F. 1999, *Astrophys. J.*, 515, L39

Chang, H.-K., Chou, D.-Y., LaBonte, B., & the TON Team 1997, *Nature*, 389, 825

Chou, D.-Y. 2000, *Solar Phys.*, 192, 241

Chou, D.-Y., & Dai, D.-C. 2001 *Astrophys. J.*, 559, L175

Chou, D.-Y., et al. 1995, *Solar Phys.*, 160, 237

Choudhury, A. R. 2003, *Solar Phys.*, 215, 31

Christensen-Dalsgaard, J. 2002, *Rev. of Modern Phys.*, 74, 1073

Christensen-Dalsgaard, J., Duvall, T. L., Jr., Gough, D. O., Harvey, J. W., & Rhodes, E. J., Jr. 1985, *Nature*, 315, 378

Christensen-Dalsgaard, J., Schou, J., & Thompson, M. J. 1990, *Mon. Not. R. Astron. Soc.*, 242, 353

Christensen-Dalsgaard, J., et al. 1996, *Science*, 272, 1286

Claverie, A., Issak, G. R., McLeod, C. P. van der Raay, H. B., & Roca Cortes, T. 1979, *Nature*, 282, 591

Couvidat, S., Birch, A. C., Kosovichev, A. G., & Zhao, J. 2004, *Astrophys. J.*, in press

DeRosa, M. L., Gilman, P. A., Toomre, J. 2002, *Astrophys. J.*, 581, 1356

Deubner, F.-L. 1975, *Astron. Astrophys.*, 44, 371

DeVore, C. R. 2000, *Astrophys. J.*, 539, 944

Dikpati, M., & Charbonneau, P. 1999, *Astrophys. J.*, 518, 508

D'Silva, S., & Duvall, T. L., Jr. 1995, *Astrophys. J.*, 438, 454

D'Silva, S., & Howard, R. F. 1994, *Solar Phys.*, 151, 213

Duvall, T. L., Jr. 1979, *Solar Phys.*, 63, 3

Duvall, T. L., Jr. 1980, *Solar Phys.*, 66, 213

Duvall, T. L., Jr. 1998, in *Proceedings of SOHO 6/ GONG 98 Workshop: Structures and Dynamics of the Interior of the Sun and Sun-like Stars*, (ESA SP-418), 581

Duvall, T. L., Jr., D'Silva, S., Jefferies, S. M., Harvey, J. W., & Schou, J. 1996, *Nature*, 379, 235

Duvall, T. L., Jr., Dziembowski, W. A., Goode, P. R., Gough, D. O., Harvey, J. W., & Leibacher, J. W. 1984, *Nature*, 310, 22

Duvall, T. L., Jr., & Gizon, L. 2000, *Solar Phys.*, 192, 177

Duvall, T. L., Jr., Harvey, J. W. 1983, *Nature*, 302, 24

Duvall, T. L., Jr., Jefferies, S. M., Harvey, J. W., & Pomerantz, M. A. 1993, *Nature*, 362, 235

Duvall, T. L., Jr., et al. 1997, *Solar Phys.*, 170, 63

Evershed, J. 1909, *Mon. Not. R. Astron. Soc.*, 69, 454

Frazier, E. N. 1970, *Solar Phys.*, 14, 89

Giles, P. M. 1999, Ph.D. Thesis, Stanford University

Giles, P. M., Duvall, T. L., Jr., Scherrer, P. H., & Bogart, R. S. 1997, *Nature*, 390, 52

Gilman, P. A., & Charbonneau, P. 1999, in *Magnetic Helicity in Space and Laboratory Plasmas* (Geophys. Monogr. 111; Washington DC: AGU), 75

Gilman, P. A., & Foukal, P. V. 1979, *Astrophys. J.*, 229, 1179

Gilman, P. A., & Howard, R. F. 1984, *Astrophys. J.*, 283, 385

Gizon, L. 2003, Ph.D. Thesis, Stanford Univer.

Gizon, L., & Birch, A. C. 2002, *Astrophys. J.*, 571, 966

Gizon, L., Duvall, T. L., Jr., & Larsen, R. M. 2000, *J. Astrophys. Astron.*, 21, 339

Gizon, L., Duvall, D. L., Jr., & Larsen, R. M. 2001, in *Recent Insights into the Physics of the Sun and Heliosphere - Highlights from SOHO and Other Space Missions, Proc of IAU Symposium 203*, ed. P. Brekke, B. Fleck, & J. Gurman (ASP), 189

Gizon, L., Duvall, T. L., Jr., & Schou, J. 2003, *Nature*, 421, 43

Golub, G. H., & Kahan, W. 1965, *SIAM J. Numer. Anal.*, 2, 205

González Hernández, I., Patrón, J., Bogart, R. S., & SOI Ring-Diagrams Team 1998, in *Proceedings of the SOHO 6/GONG 98 Workshop: Structure and Dynamics of the Interior of the Sun and Sun-like Stars*, ed. S. G. Korzennik, & A. Wilson (ESA SP-418, Noordwijk: ESA), 587

Gordon, A. H. 1998, *Dynamic Meteorology: a Basic Course*, Oxford University Press

Gough, D. O. 1984, *Phil. Trans. R. Soc. Lond. A*, 313, 27

Gough, D. O. 1993, in *Astrophysical Fluid Dynamics*, ed. J.-P. Zahn & J. Zinn-Justin, Elsevier Science Publ., 339

Gough, D. O., & Toomre, J. 1983, *Solar Phys.*, 82, 401

Gough, D. O., et al. 1996, *Science*, 272, 1296

Haber, D. A., Hindman, B. W., & Toomre, J. 2003, in *Local and Global Helioseismology: The Present and Future, Proc. SOHO 12/GONG+ 2002 Workshop*, ed. H. Sawaya-Lacoste (ESA SP-517; Noodwijk: ESA), 103

Haber, D. A., Hindman, B. W., Toomre, J., Bogart, R. S., Larsen, R. M., & Hill, F. 2002, *Astrophys. J.*, 570,855

Haber, D. A., Hindman, B. W., Toomre, J., Bogart, R. S., Thompson, M. J., & Hill, F. 2000, *Solar Phys.*, 192, 335

Hale, G. E. 1927, *Nature*, 119, 708

Hart, A. B. 1954, *Mon. Not. R. Astron. Soc.*, 114, 17

Harvey, J. W., et al. 1996, *Science*, 272, 1284

Hathaway, D. H., Beck, J. G., Bogart, R. S., Bachmann, K. T., Khatri, G., Petitto, J. M., Han, S., & Raymond, J. 2000, *Solar Phys.*, 193, 299

Hathaway, D. H., et al. 1996, *Science*, 272, 1284

Hill, F. 1988, *Astrophys. J.*, 333, 996

Hindman, B., Haber, D., Toomre, J., & Bogart, R. 2000, *Solar Phys.*, 192, 363

Hindman, B. W., Zhao, J., Haber, D. A., Kosovichev, A. G., & Toomre, J 2003, *Bulletin of American Astronomical Society, SPD meeting #34*, #08.06

Hiremath, K. M. 2002, *Astron. Astrophys.*, 386, 674

Howard, R. F. 1992, *Solar Phys.*, 142, 47

Howard, R. F. 1996, *Annu. Rev. Astron. Astrophys.*, 34, 75

Howard, R. F., Gilman, P. I., & Gilman, P. A. 1984, *Astrophys. J.*, 283, 373

Howard, R. F., & Harvey, J. W. 1970, *Solar Phys.*, 12, 23

Howard, R., & LaBonte, B. J. 1980, *Astrophys. J.*, 239, L33

Howe, R., Christensen-Dalsgaard, J., Hill, F., Komm, R. W., Larsen, R. M., Schou, J., Thompson, M. J., & Toomre, J. 2000, *Astrophys. J.*, 533, L163

Howe, R., Christensen-Dalsgaard, J., Hill, F., Komm, R. W., Larsen, R. M., Schou, J., Thompson, M. J., & Toomre, J. 2000, *Science*, 287, 2456

Hurlburt, N. E., & Rucklidge, A. M. 2000, *Mon. Not. R. Astron. Soc.*, 314, 793

Jacobsen, B. H., Møller, I., Jensen, J. M., & Effersø, F. 1999, *Phys. Chem. Earth*, 24, 15

Jensen, J. M., Duvall, T. L., Jr., Jacobsen, B. H., & Christensen-Dalsgaard, J. 2001, *Astrophys. J.*, 553, L193

Jensen, J. M., Jacobsen, B. H., & Christensen-Dalsgaard, J. 1998, in *Proceedings of SOHO 6/GONG 98 Workshop: Structure and Dynamics of the Interior of the Sun and Sun-like Stars*, ed. S. G. Korzennik & A. Wilson (ESA SP-418; Noordwijk: ESA), 635

Jensen, J. M., Jacobsen, B. H., & Christensen-Dalsgaard, J. 2000, *Solar Phys.*, 192, 231

Kleeorin, N. I., & Ruzmaikin, A. A. 1991, *Solar Phys.*, 131, 211

Knoška, Š. 1975, *Bulletin Astronomical Inst. Czechoslovakia*, 26, 151

Komm, R. W., Howard, R. F., & Harvey, J. W. 1993, *Solar Phys.*, 145, 1

Kosovichev, A. G. 1996, *Astrophys. J.*, 461, L55

Kosovichev, A. G. 1999, *Journal of Computational and Applied Mathematics*, 109, 1

Kosovichev, A. G., & Duvall, T. L., Jr. 1996, in *Proceedings of SCORe Workshop: Solar Convection and Oscillations and Their Relationship*, ed. J. Christensen-Dalsgaard & F. Pijpers (Dordrecht: Kluwer), 241

Kosovichev, A. G., Duvall, T. L., Jr., & Scherrer, P. H. 2000, *Solar Phys.*, 192, 159

Kosovichev, A. G., Duvall, T. L., Jr., & Zhao, J. 2002, in *Proc. Magnetic Coupling of the Solar Atmosphere Euroconference and IAU Coll. 188*, (ESA SP-505, Noordwijk), 79

Kosovichev, A. G., & Schou, J. 1997, *Astrophys. J.*, 482, 207

Kosovichev, A. G., & Zharkova, V. V. 1998, *Nature*, 393, 317

Kosovichev, A. G., et al. 1997, *Solar Phys.*, 170, 43

Leibacher, J., & Stein, R. F. 1971, *Astrophys. Lett*, 7, 191

Leighton, R. B., Noyes, R. W., & Simon, G. W. 1962, *Astrophys. J.*, 135, 474

Leka, K. D., Canfield, R. C., & McClymont, A. N. 1996, *Astrophys. J.*, 462, 547

Lindsey, C., & Braun, D. C. 1997, *Astrophys. J.*, 485, 895

Lindsey, C., & Braun, D. C. 2000, *Science*, 287, 1799

Lindsey, C., & Braun, D. C. 2000, *Solar Phys.*, 192, 261

Lindsey, C., Braun, D. C., Jefferies, S. M., Woodard, M. J., Fan, Y., Gu, Y., and Redfield, S. 1996, *Astrophys. J.*, 470, 636

Liu, Y., & Norton, A. A. 2001 *SOHO*/MDI Technical Note, `http://soi.stanford.edu/general/TechNotes/01.144/TN01-144.pdf`

Longcope, D. W., Fisher, G. H., & Pevtsov, A. A. 1998, *Astrophys. J.*, 507, 417

López Fuentes, M. C., Démoulin, P., Mandrini, C. H., Pevtsov, A. A., & van Driel-Gesztelyi, L. 2003, *Astron. Astrophys.*, 397, 305

Magara, T., & Longcope, D. W. 2003, *Astrophys. J.*, 586, 630

Martin, S. F., Billamoria, R., & Tracadas, P. W. 1994, in Rutten R. J. & Schrijver, C. J. (eds), *Solar Surface Magnetism*, Kluwer, Dordrecht, 303

Menke, W. 1984, *Discrete Inverse Theory*, Geophys. Series vol. 45, Academic Press Inc.

Mestel, L. 1999, *Stellar Magnetism*, Oxford University Press, Chapter 6

Meunier, N. 1999, *Astrophys. J.*, 527, 967

Meyer, F., Schmidt, H. U., Weiss, N. O. and Wilson, P. R. 1974, *Mon. Not. R. Astron. Soc.*, 169, 35

Mickey, D. L., Canfield, R. C., LaBonte, B. J., Leka, K. D., Waterson, M. F. and Weber, H. M. 1996, *Solar Phys.*, 168, 229

Moffatt, H. K. 1978, *Magnetic Field Generation in Electrically Conducting Fluids*, Cambridge University Press, Cambridge

Moon, Y.-J., Chae, J., Choe, G. S., Wang, H., Park, Y. D., Yun, H. S., Yurchyshyn, V., & Goode, P. R. 2002, *Astrophys. J.*, 574, 1066

Nindos, A., & Zhang, H 2002, *Astrophys. J.*, 573, L133

November, L. J., & Simon, G. W. 1988, *Astrophys. J.*, 333, 427

Paige, C. C., & Saunders, M. A. 1982, *ACM Trans. Math. Software*, 8, 43

Parker, E. N. 1979, *Astrophys. J.*, 230, 905

Parker, E. N. 1994, *Astrophys. J.*, 433, 867

Pevtsov, A. A., Balasubramaniam, K. S., & Rogers, J. W. 2003, *Astrophys. J.*, 595, 255

Pevtsov, A. A., Canfield, R. C., & Latushko, S. M. 2001, *Astrophys. J.*, 549, L261

Pevtsov, A. A., Canfield, R. C., & Metcalf, T. R. 1995, *Astrophys. J.*, 440, L109

Press, W. H., Teukolsky, S. A., Vetterling, W. T., & Flannery, B. P. 1992, *Numerical Recipes in FORTRAN 77* (2nd ed.; Cambridge, Cambridge Univ. Press)

Rajaguru, S. P., Basu, S., & Antia, H. M. 2001, *Astrophys. J.*, 563, 410

Rimmele, T. 1995, *Astron. Astrophys.*, 298, 260

Rüdiger, G., Pipin, V. V., & Belvedère, G. 2001, *Solar Phys.*, 198, 241

Ryutova, M., & Scherrer, P. H. 1998, *Astrophys. J.*, 494, 438

Rust, D. M., & Kumar, A. 1996, *Astrophys. J.*, 464, L199

Schatten, K. H., & Mayr, H. G. 1985, *Astrophys. J.*, 299, 1051

Scherrer, P. H., et al. 1995, *Solar Phys.*, 162, 129

Schlichenmaier, R. and Schmidt, W. 1999, *Astron. Astrophys.*, 349, L37

Schou, J, 1999, *Astrophys. J.*, 523, L181

Schou, J. 2003, *Astrophys. J.*, 596, L259

Schou, J., & Bogart, R. S. 1998, *Astrophys. J.*, 504, L131

Schou, J., et al. 1998, *Astrophys. J.*, 505, 390

Schrijver, C. J., et al. 1999, *Solar Phys.*, 187, 261

Schüssler, M. 1981, *Astron. Astrophys.*, 94, L17

Seehafer, N. 1996, *Phys. Rev. E*, 53, 1283

Simon, G. W. 1967, *Z. Astrophys.*, 65, 345

Sivaraman, K. R., Gupta, S. S., & Howard, R. F. 1993, *Solar Phys.*, 146, 27

Sivaraman, K. R., Sivaraman, H., Gupta, S. S., & Howard, R. F. 2003, *Solar Phys.*, 214, 65

Snodgrass, H. B. 1984, *Solar Phys.*, 94, 13

Snodgrass, H. B. 1985, *Astrophys. J.*, 291, 339

Snodgrass, H. B. 1987, *Astrophys. J.*, 316, 91

Snodgrass, H. B., & Ulrich, R. K. 1990, *Astrophys. J.*, 351, 309

Spiegel, E. A., & Zahn, J.-P. 1992, *Astron. Astrophys.*, 265, 306

Spruit, H. C. 2003, *Solar Phys.*, 213, 1

Stanchfield II, D. C. H., Thomas, J. H., & Lites, B. W. 1997, *Astrophys. J.*, 477, 485

Stix, M. 2002, *The Sun: an Introduction* (Springer-Verlag New York)

Sun, M. T., Chou, D. Y., & the TON Team 2002, *Solar Phys.*, 209, 5

Thomas, J. H. and Weiss, N. O. 1992, in J. H. Thomas and N. O. Weiss(eds.), *Sunspots: Theory and Observations*, 1992, Kluwer Academic Publishers, Netherlands, 3

Thompson, M. J., et al. 1996, *Science*, 272, 1300

Tokman, M., & Bellan, P. M. 2002, *Astrophys. J.*, 567, 1202

Ulrich, R. K. 1970, *Astrophys. J.*, 162, 993

Ulrich, R. K. 2001, *Astrophys. J.*, 560, 466

Vorontsov, S. V., Christensen-Dalsaard, J., Schou, J., Strakhov, V. N., & Thompson, M. J. 2002, *Science*, 296, 101

Wang, H. 1989, *Solar Phys.*, 123, 21

Wang, H., & Zirin, H. 1992, *Solar Phys.*, 140, 41

Wang, Y.-M., Sheeley, N. R., Jr., & Nash, A. G. 1991, *Astrophys. J.*, 383, 431

Woodard, M. F. 1997 *Astrophys. J.*, 485, 890

Woodard, M. F., & Noyes, R. W. 1985, *Nature*, 318, 449

Zhao, J., & Kosovichev, A. G. 2003a, in *Proceeding of SOHO 12/ GONG+ 2002 Workshop, Local and Global Helioseismology: the Present and Future*, ed. H. Sawaya-Lacoste (ESA SP-517; Noordwijk: ESA), 417

Zhao, J., & Kosovichev, A. G. 2003b, *Astrophys. J.*, 591, 446

Zhao, J., & Kosovichev, A. G. 2004, *Astrophys. J.*, 603, 776

Zhao, J., Kosovichev, A. G., & Duvall, T. L., Jr. 2001, *Astrophys. J.*, 557, 384

Zhao, J., Kosovichev, A. G., & Duvall, T. L., Jr. 2004, *Astrophys. J.*, submitted